MECHANICAL BEHAVIOR OF CARBON NANOTUBE FORESTS UNDER COMPRESSIVE LOADING

A Dissertation
Presented to
The Academic Faculty

By

Parisa Pour Shahid Saeed Abadi

In Partial Fulfillment
of the Requirements for the Degree
Doctor of Philosophy in the
George W. Woodruff School of Mechanical Engineering

Georgia Institute of Technology

May 2013

MECHANICAL BEHAVIOR OF CARBON NANOTUBE FORESTS UNDER COMPRESSIVE LOADING

Approved by:

Dr. Samuel Graham, Advisor
School of Mechanical Engineering
Georgia Institute of Technology

Dr. Hamid Garmestani
School of Materials Science and Engineering
Georgia Institute of Technology

Dr. Baratunde A. Cola, Advisor
School of Mechanical Engineering
Georgia Institute of Technology

Dr. Ting Zhu
School of Mechanical Engineering
Georgia Institute of Technology

Dr. Satish Kumar
School of Materials Science and Engineering
Georgia Institute of Technology

Date Approved: April 3, 2013

To my husband (Hassan Masoud),

and my parents (Pari Shekouh and Seyyed Ata PourShahid)

ACKNOWLEDGEMENTS

First, I am grateful to God for enabling me to accomplish this research and all other goals of my life.

Then, I would like to express my deep appreciation to my advisors, Dr. Samuel Graham and Dr. Baratunde Cola, for their incessant guidance and assistance throughout my entire Ph.D research process. I really appreciate their constructive comments and criticism and the freedom they gave me to explore my ideas. I would also like to thank Dr. Satish Kumar, Dr. Hamid Garmestani, and Dr. Ting Zhu for serving on my committee. Their comments added a lot to my research.

Many other people contributed to this work. I would like to thank Dr. Julia Greer from Caltech who offered me her lab equipment for conducting in situ mechanical experiments. I'm grateful to Dr. Matthew Maschmann from AFRL for all his help throughout this work including conductance of mechanical testing experiments. I wish to express my gratitude to others who assisted me throughout this research specially Dr. Shelby Hutchens form Caltech, John Taphouse, and Dr. Anuradha Bulusu from Georgia Tech, and Denzell Bolling, undergraduate student visitor from Howard University.

I would like to acknowledge my lab mates, colleagues and friends for their support and help, and useful conversations throughout my stay at Georgia Tech. Special thanks go to NEST and EMRL group members, to faculty and staff of the school of mechanical engineering in Georgia Tech who helped me in different ways, specially Dr. Jason Nadler and Dr. Yogendra Joshi for offering their lab equipment to be used for this dissertation, and to the staff of Microelectronic Research Center in Georgia Tech

specially Walter Henderson, Ben Hollerbach, John Pham, and Charlie Suh for great assistance in performing experiments for this dissertation.

I am ever thankful to my husband for his love and support. I could not have accomplished this work without his support and encouragement during the tough times. I can never thank my parents enough. They sacrificed a lot so I can be where I am now. Thank you and I love you. I wish to thank my siblings and all family members and friends who loved me and supported me.

Contents

List of Tables

List of Figures

SUMMARY

Carbon nanotube (CNT) forests are an important class of nanomaterials with many potential applications due to their unique properties such as mechanical compliance, thermal and electrical conductance, etc. Their deformation and failure in compression loading is critical in any application involving contact because the deformation changes the nature of the contact and thus impacts the transfer of load, heat, and charge carriers across the interface. The micro- and nano-structure of the CNT forest can vary along their height and from sample to sample due to different growth parameters. The morphology of CNTs and their interaction contribute to their mechanical behavior with change of load distribution in the CNT forest. However, the relationship is complicated due to involvement of many factors such as density, orientation, and entanglement of CNTs. None of these effects, however, are well understood. This dissertation aims to advance the knowledge of the structure-property relation in CNT forests and find methodologies for tuning their mechanical behavior. The mechanical behavior of CNT forests grown with different methodologies is studied. Furthermore, the effects of coating and wetting of CNT forests are investigated as methods to tailor the degree of interaction between CNTs. In situ micro-indentation of uncoated CNT forests with distinct growth-induced structures are performed to elucidate the effects of change of morphology along the height of CNT forests on their deformation mechanism. CNT aerial density and tortuosity are found to dictate the location of incipient deformation along height of CNT forests. Macro-compression testing of uncoated CNT forests reveals mechanical failure of CNT forests by delamination at the CNT-growth substrate. Tensile loading of CNT roots due to post-buckling bending of CNTs is proposed to be the cause of this failure and simple bending theory is shown to estimate the failure load to be on the same order of magnitude as experimental measurements. Furthermore, delamination is observed to occur in the in situ micro-indentation of CNT forests coated with aluminum on the top surface, which demonstrates the role of the mechanical constraints within the CNT forest in the occurrence of delamination at the CNT-substrate interface. In addition, this dissertation explores the mechanical behavior of CNT forests coated conformally (from top to bottom) with alumina by atomic layer deposition. In situ micro-indentation testing demonstrates that the deformation mechanism of CNT forests does not change with a thin coating (2 nm) but does change with a sufficiently thick coating (10 nm) that causes fracturing of the hybrid nanotubes. Ex situ flat punch and Berkovich indentations reveal an increase in stiffness of the CNT forests that are in range with those predicted by compression and bending theories. An increase in the recoverability of the CNTs is also detected. Finally, solvent infiltration is proposed as a method of decreasing stiffness of CNT forests and changing the deformation mechanism from local to global deformations (i.e., buckling in the entire height). Presence of solvents between CNTs decreases the van der Waals forces between them and produces CNT forests with lower stiffness. The results demonstrate the effect of interaction between CNTs on the mechanical behavior. This dissertation reveals important information on the mechanical behavior of CNT forests as it relates to CNT morphology and tube-to-tube interactions. In addition, it provides a framework for future systematic experimental and theoretical investigations of the structure-property relationship in CNT forests, as well as a framework for tuning the properties of CNT forests for diverse applications.

CHAPTER 1 INTRODUCTION

1.1 Applications and motivation

Nanomaterials are defined as materials which are composed of granules with at least one dimension in the range of 1-100 nm [1, 2]. The schematic in Fig. 1.1 illustrates a bulk material and three types of nanomaterials composed of small granules. Mechanical behavior of nanomaterials is different from their bulk materials due to the dominance of interfaces [2] and different distributions of atoms (localized on the surface of granules in contrast to distribution over the volume of granules in the case of ordinary materials) [1].

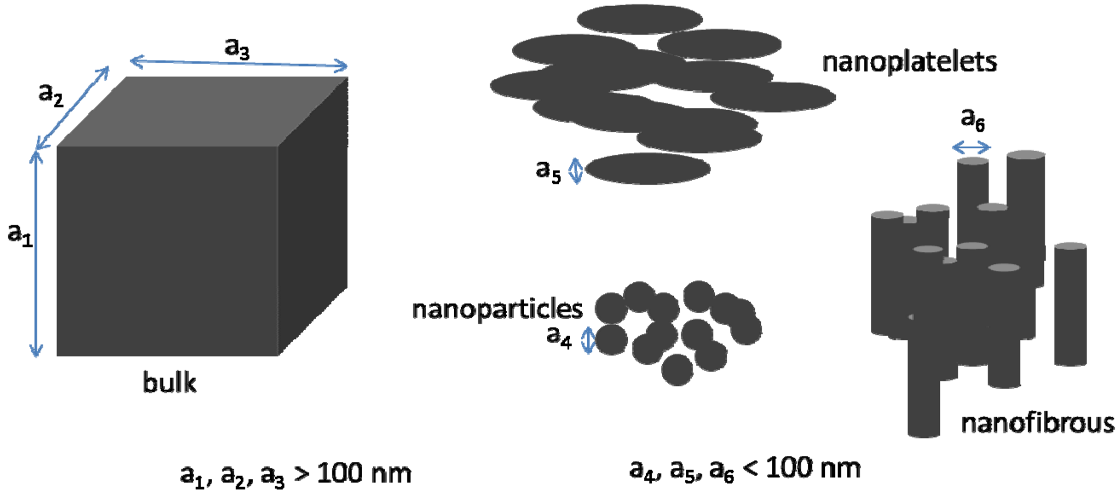

Fig. 1.1. Schematic showing a bulk material (left) and three types of nanomaterials (right). The dimension limitations [1, 2] are demonstrated.

As an important class of nanomaterials, carbon nanotube (CNT) forests, also known as vertically aligned CNTs (VACNTs), CNT turfs, and CNT arrays, are composed of intertwined extra-high aspect ratio CNTs (Fig. 1.2). Owing to their unique properties (*e.g.*, high thermal and electrical conductivity, optical absorption, and mechanical compliance), they are excellent candidates for applications such as field emitters [3], thermal interfaces [4, 5], electrical [6] interfaces, super dark absorbers [7, 8], through wafer interconnects [9], and electrochemical capacitors [10]. Though CNTs in a CNT forest appear to be vertically aligned on the scale of tens or hundreds of microns, at higher magnifications the individual CNTs are clearly discernible and exhibit various degrees of misalignment and entanglement (Fig. 1.2). The differences in the density, orientation and entanglement of the CNTs are expected to lead to inevitable vertical variations in interaction among the tubes within the forests in the vertical direction. The individual CNTs are the load bearing members of the material. Therefore, the variations within the morphology and interaction between the CNTs are expected to govern their mechanical response under loading. Thus, their complex and intertwined morphology must be investigated in detail in order to link their deformation response to their underlying structure. Investigation of the relation between the microstructure morphology and the mechanical behavior is critically important in applications involving loading of CNTs. Understanding of the relation between the micro/nano-structure and the deformation and failure characteristics is necessary for the design of CNT forests and other similar nanostructures (e.g. structures composed of nanofibers, nanorods, etc) where the collective behavior of the material could be substantially different from the behavior of individual components due to interaction between them.

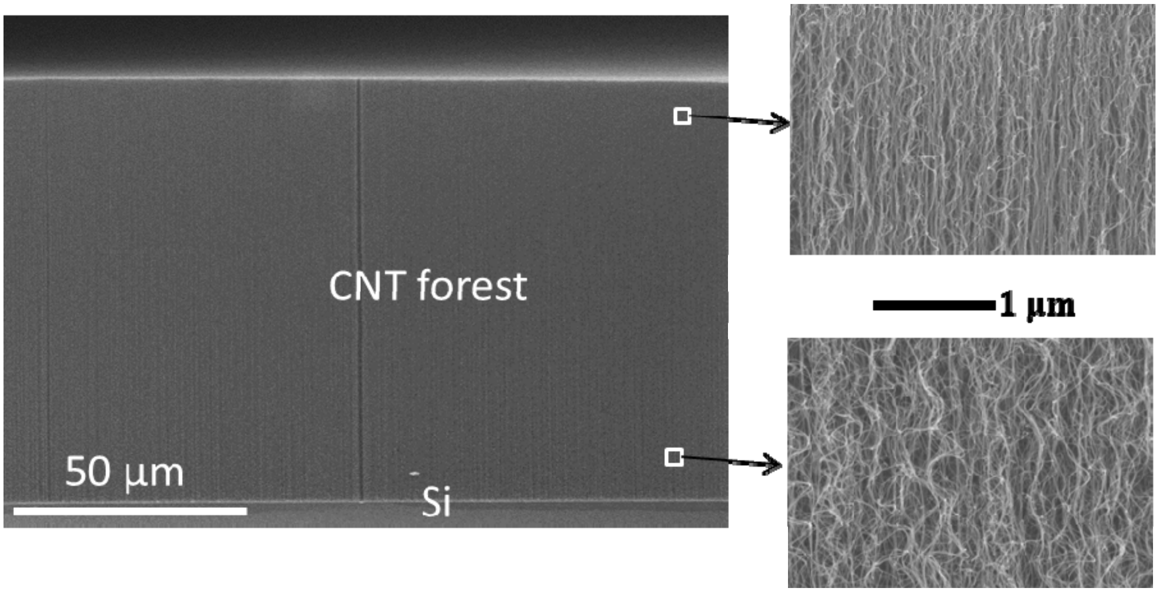

Fig. 1.2. SEM images of a side edge of a CNT forest. Left: larger scale in which individual CNTs are not discernible, and Right: smaller scale in which change of morphology from top to bottom of the forest is clear.

Mechanical properties of CNT forests and their deformation mechanisms have been investigated in the literature [11-23]. CNT forests have been shown to deform dominantly with formation of local buckles along their heights [8, 9, 24-28]. The measured properties and reported deformation mechanisms differ substantially in different studies. For instance, elastic modulus of CNT forests measured by micro-/nano-indentation ranges from <1 MPa to >1 TPa due to the differences between the samples, indenters, and/or quantification methodologies. A summary of some examples is listed in Table 1.1 (adapted from ref [29]). Decoupling of the effects of CNT forest morphology from other factors requires testing different samples with the same indenter and measurement methodologies to eliminate the effect of variations in indenter geometry and measurement methodologies. Furthermore, the local buckling within the forests has been reported to begin at different locations along the height of CNT forests such as the bottom (*i.e.*, close to the substrate) [17, 19, 22, 30] or top [21, 22] of the CNT forests. Morphology gradients have been proposed [17, 19, 21, 22] to be related to the location of incipient buckling in CNT forests. However, the effects of change of growth-induced morphological gradients along the height of CNT forests on their mechanical behavior are poorly understood. CNT forests with distinct different morphologies should be tested to help understanding of this relationship.

Table 1.1. Various modulus values measured for different CNT forests with different indenters and measurement methodologies. (adapted from ref. [21])

Support substrate	Indenter tip/compressive technique	CNT height	CNT diameter	Onset of buckling strain	Elastic compressive modulus	Modulus computation method
Silicon [31]	Berkovich – 1000 nm diameter tip	60 µm	N/A	0.03	14.9 ± 5.7 MPa	Unloading stiffness
Adhered to solid [32]	1 mm Diameter probe	>1 mm	43 nm	0.1	27.6 MPa	Loading stiffness
Silicon [30]	Quartz strut – 2 × 0.5 mm cross section	15, 40, 500 µm	20–30 nm	N/A	0.22 - 0.25 MPa	Loading stiffness
Crystalline [33]	3-Sided pyramid	570–1100 nm	55–104 nm	N/A	0.9 - 1.23 Tpa	Bending stiffness
Silicon [34]	Berkovich	N/A	N/A	N/A	40 - 600 MPa	Continuous stiffness
SiC [16]	2, 10, 27 µm Diameter spheres	0.2 and 1.3 µm	1–3 nm	0.08, 0.03, 0.01	18 GPa	Loading stiffness
Freestanding film [15]	Parallel plates	3.4 mm	53 nm	N/A	0.9 - 2.2 MPa	Loading stiffness
Freestanding film [35]	Parallel plates	2.2 mm	50 nm	0.01	2.1 - 20.8 MPa	Loading stiffness
Freestanding film [17]	Parallel plates	860 µm	40 nm	0.22	12 MPa	Loading stiffness
Freestanding pillar [36]	Parallel plates	>1 cm	N/A	0.15	10 - 12 MPa	Loading stiffness

While changing growth parameters is a way to control CNT morphology and mechanical behavior of CNT forests, coating CNT forests could also be used to tailor mechanical behavior of CNT forests. Coating a CNT forest creates a hybrid nanostructure and adding material is expected to change the mechanical properties with changing the properties of individual CNTs and perhaps the degree of interaction between them. Moreover, the process to apply thin film coatings is more controllable than the typically variations observed through CNT synthesis techniques. Coated CNTs have attracted the attention of many researchers [24, 37-47] because of their potential applications as optical, electronic, catalytic, sensing, and magnetic materials or as reinforcement in composite materials. Different coating methods such as physical vapor deposition [45, 46], chemical vapor deposition [40, 42], electroless plating [37, 38], and atomic layer deposition [29, 48-50] have been employed to coat the CNTs. Understanding the mechanical behavior of coated CNT forests is important not only because they are under loading in some applications, but also because this investigation reveals the effect of intentional change of properties of individual CNTs and/or degrees of interaction between CNTs. Raney et al. [14] performed compression testing of CNT forests coated with SnO_2 and MnO_2 nanoparticles using solution-based and kinetically-controlled catalytic synthesis approaches. They reported higher energy dissipation in the coated CNT forests. The deformation mechanism such as bending, buckling, and failure mechanism still requires an extensive investigation. It is critical to understand how the mechanical response of such coated forests might differ from the response of pristine structures as this may change the performance of CNT forests in the application after coating. Also, the knowledge may be used for tailoring the properties of CNT forests by coating.

Observation of different mechanical behaviors in CNT forests with different degrees of entanglement [21] and correlations between morphology gradients along height of CNT forests and their deformation mechanism [17, 19, 21, 22] suggest that interaction between CNTs affect the collective mechanical response of CNT forests. CNTs interact with each other via well-known van der Waals forces. One of the factors that influence van der Waals forces between two objects is the medium between them [51]. However, previous investigations of the deformation and mechanical properties of CNT forests have been focused on CNT forests in air. The effects of medium such as fluids have not been investigated. Investigation of the effect of solvents on the mechanical behavior of CNT forests will be important for applications of CNT forests involving wetting of CNT forests (such as coating of CNT forests with polymers using polymer-filled solvents [52]), they may also provide an easy and practical way of tailoring CNT forest properties.

The use of CNT forests as thermal or electrical interface materials is an example of an application in which mechanical loading of CNTs and deformation within the CNT forest is critical in their performance. Conformability and compliance of interface materials, along with high conductivity, are critical factors in their performance because high values for these parameters increase the real contact area established with rough adjacent surfaces and decreases the interfacial resistance [25, 27, 53]. Park et al. [6] demonstrated that electrical resistance was decreased by using multiwall CNTs (MWCNTs) at a Cu-Cu interface due to the deformability. They also showed that increasing pressure on the interface decreases the resistance and hence suggests a potential use of the structure as a pressure sensor. CNT forests were also shown to perform as an excellent thermal interface material (TIMs) due to their high thermal conductivity and mechanical compliance [27, 54, 55]. Cola et al. [27] developed a model based on the mechanical properties of individual CNTs which predicts the real contact area at the free CNT tips in contact with an opposing surface. The mechanical model was employed to develop a thermal resistance model, which predicts that the interfacial thermal resistance at the CNT free ends is the dominant component of the total thermal resistance. This shows the importance of conformability and deformations of the CNTs in the thermal performance of CNT interface materials. Cola et al. [56] measured the pressure dependency of the thermal resistances of CNT forests grown on SiC substrates and observed an expected decrease in the resistance of the CNT forest interface on the C side of a SiC substrate and an unexpected increase followed by a decrease in the resistance of the CNT forest interface on the Si side of a SiC substrate upon loading. The increase was suggested to be due to weaker adhesion of CNTs to the Si side; again, indicating the important role interfacial mechanics plays in the performance of CNT TIMs. In 2011, Lin et al. [57] observed a significant decrease in thermal diffusivity in compression of CNT forests. They proposed that the observed permanent deformations (buckling) in the VACNT films could be a cause of decrease in thermal diffusivity at high pressures due to damage to the CNT nanostructure. All of the preceding issues related to the effect of loading and deformations upon loading in CNT forest interface materials call for a better understanding of the mechanical behavior of CNT forests and study of methods for tailoring the mechanical behavior of CNT forests. Although finding direct connections between the mechanical behavior and thermal performance is not the primary objective of this work, the knowledge gained in this dissertation will help to provide recommendations for future work.

1.2 Objectives

To address the aforementioned outstanding issues related to the mechanical behavior of vertically aligned CNT forests in the pristine form, coated, and solvent infiltrated, the objectives of this dissertation are as follows.

1) to investigate the effect of the morphology along height of CNT forests on the micro-compression response of the forests.

2) to study the deformation and failure mechanism in macro-compression of CNT forests.

3) to quantify the mechanical properties (e.g. stiffness and recoverability) and visualize the deformation mechanism of coated CNT forests where the coatings are applied on top or conformally along the height of the individual CNTs.

4) to examine the mechanical behavior of CNT forests soaked in solvents.

This dissertation seeks to provide new insight into the mechanical behavior of materials made from 1-D nanomaterials, more specifically, CNT forests. This is expected to be of interest to the nanomaterials community for use in the design of nanostructures for different applications. The next chapters are organized as follows:

Chapter 2 provides an overview of the relevant literature and background on growth, structure, coating, and mechanical characterization of CNT forests.

Chapter 3 explores the mechanical response of distinct carbon nanotube (CNT) morphologies by flat punch nanoindentation in a scanning electron microscope. Buckling behavior was studied and stiffness and recoverability were measured and compared for CNT forests with different heights and CNT forests grown using different methods.

Chapter 4 reports buckling-driven delamination of carbon nanotube (CNT) forests from their growth substrates in macro-compression of uncoated CNT forests and in micro-compression of CNT forests coated on top with aluminum. The structural causes of this failure mechanism were investigated.

Chapter 5 investigates the mechanical behavior of CNT forests coated from top to bottom with alumina by atomic layer deposition. Stiffness, recoverability, and failure mechanisms were explored.

Chapter 6 provides information on the mechanical behavior of carbon nanotube forests soaked in solvents such as toluene and acetonitrile. Effective stiffness of the structure was evaluated in the dry and wet condition by micro-indentation experiments.

Chapter 7 concludes this dissertation by providing a summary of the work and directions for future work.

Table 1.2. Overview of the dissertation.

Topic	Method	Major results	Chapter
Micro-compression of uncoated CNT forests	In situ flat punch indentation	• Synthesis of three types of CNT forests with distinct morphological gradients along height. • Connection between the location of initial buckle along height and the CNTs morphology. • CNT aerial density and tortuosity revealed to govern the micro-compression response of CNT forests.	3
Macro-compression of uncoated CNT forests	Ex situ macro-scale compression	• Observation of local delamination of CNT forests from the growth substrate. • Tensile loading of CNT roots due to bending of buckled CNTs suggested as the possible reason for delamination occurrence. • Elucidation of correlation between height nonuniformity of CNT forests and the location of delamination occurrence.	4

Table 1.2 continued.

Micro-compression of CNT forests coated with aluminum on top	In situ flat punch indentation	• Observation of delamination of coated CNT forests from the growth substrate. • Order of magnitude estimation of tensile strength of CNT forest-substrate interface using Euler-Bernoulli beam bending theory. • Experimental measurement of the tensile strength of CNT forest-substrate interface by macro-scale tensile testing to compare with the theoretical estimation-good agreement.	4
Indentation of CNT forests conformally coated with ALD alumina	In situ flat punch indentation and ex situ flat punch and Berkovich indentation	• Observation of fracturing of hybrid alumina-CNT nanotubes via in situ testing. • Identification of the effects of coating on the stiffness and recoverability of CNT forests using ex situ testing. • Theoretical estimation of increase in stiffness due to coating using compression and bending theories.	5
Indentation of CNT forests soaked in solvents	In situ flat punch indentation	• Evaluation of load-displacement of CNT forests soaked in different solvents. • Connection between changes in van der Waals forces between CNTs and the stiffness change by soaking CNT forests in solvents.	6

CHAPTER 2 BACKGROUND AND RELEVANT LITERATURE

2.1 CNT forest growth

After the report of the synthesis of nanoscale “needle-like” carbon tubes by Iijima in 1991 [58], many research groups have worked on the synthesis of CNTs. Among other common growth methodologies for multiwall CNTs such as arc-discharge and laser ablation, catalytic chemical vapor deposition is known for its flexibility and being commercially attractive [59]. While arc-discharge and laser ablation use solid-state carbon precursors and high temperatures for vaporization of the precursors, CVD utilizes lower temperatures (500-1000^{o}C) and hydrocarbon gases as carbon source [60]. While the other two methods only produce tangled CNTs, CVD is more controllable and can be used for synthesis of CNT forests in vertical direction [60]. A schematic of the mechanism of multiwall CNT growth by CVD [61] is shown in Fig. 2.1. In a well-accepted CNT growth mechanism, hydrocarbon decomposes and the carbon dissolves in the hot metal catalyst. After saturation of the metal particle, crystallization starts and carbon atoms form cylindrical walls of a multiwall carbon nanotube. The CNT could grow on the metal particle (root growth) or carry it to the top of the forest (tip growth). Transition metals such as iron, cobalt, and nickel have been successfully used as catalyst due to their ability to decompose gas molecules containing carbon source for CNT growth [59, 62]. Support layers such as Al_2O_3 and SiO_2 are usually used as support layer under the catalyst to provide support and stabilize the catalyst particle distribution by physical interaction with the catalyst layer [59]. Plasma enhanced chemical vapor deposition (PECVD) has also been used for production of vertically aligned CNTs by use of plasma during growth, which causes more alignment of CNTs [63]. Xu and Fisher [64] developed a trilayer structure composed of Ti, Al, and a transition metal (e.g., Fe, Mo, or Ni) for growth of dense vertical CNTs arrays via microwave PECVD on different substrates. A similar trilayer is used with a thermal CVD method in this work for the purpose of growth of dense CNT forests.

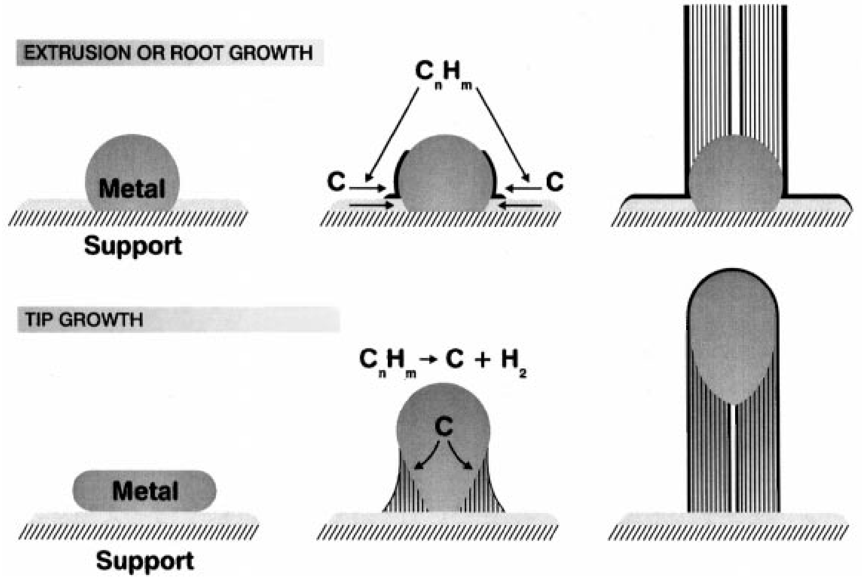

Fig. 2.1. CVD multiwall CNT growth mechanism [61, 62].

2.2 CNT forest structure

Understanding the mechanics of CNT forests requires an in-depth understanding of the microstructure complexities along the height. Previous researchers have investigated the morphology change of CNT forests along the height. CVD grown CNT forests usually have a crust layer of entangled CNTs on top [65, 66]. The crust layer on top provides support for the vertical growth of the CNTs [66]. Wu et al. [67] reported that

CNTs within a CVD grown forest were curlier at the bottom of the forest than at the top. They suggested that the curling of CNTs and the consequent increase in packing density are the causes of decrease in the growth rate and the growth termination by decreasing the diffusion rate of carbon source to nucleation sites on the substrate. Bedewy et al. [65] reported a decrease in CNT number density from top to bottom of VACNTs using mass density measurements vs. height change, while assuming the CNTs to be continuous straight hollow cylinders. They also quantified the time evolution of CNT alignment by synchrotron X-ray scattering and showed that CNT alignment emerges and stabilizes at the beginning of growth and then decays gradually before self-termination that coincides with formation of a random morphology close to the substrate. The loss of alignment has been suggested by other researchers [67, 68] to be caused by defect growth in CNTs or by gravity. In summary, the CNT forest growth has been suggested [65] (demonstrated in Fig. 2.2) to be composed of four major stages: (1) nucleation and self-organization of randomly oriented CNTs into a vertical forest, (2) steady state growth without a significant change of density, (3) CNT number density decay with time, (4) self-termination causing loss of alignment.

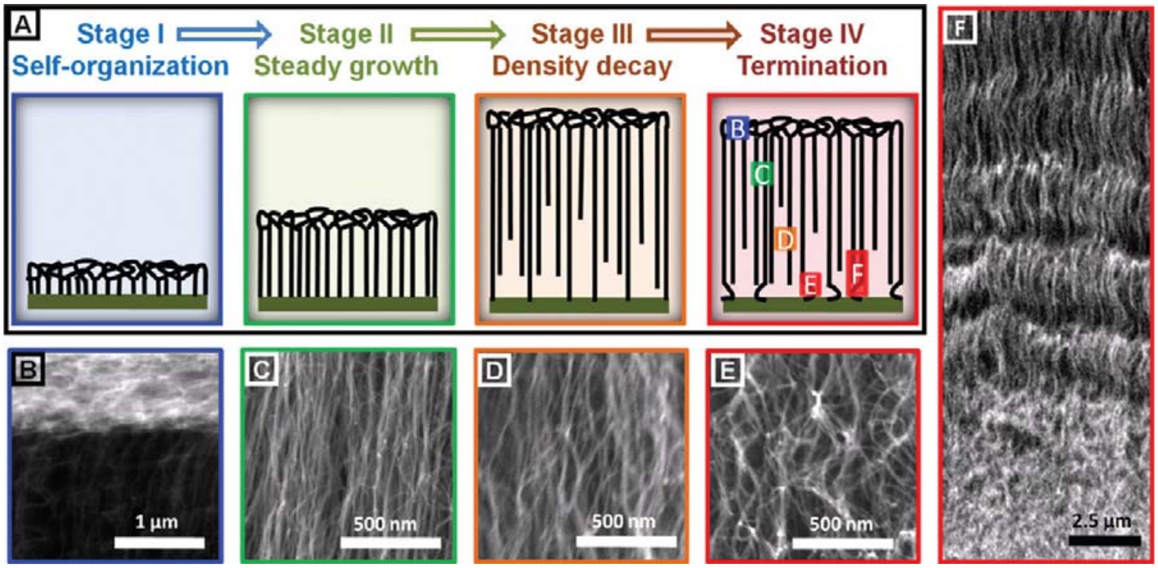

Fig. 2.2. CNT forest growth stages [65]. a) schematic demonstration of the CNT forest growth stages, and b-f) SEM images of locations marked on the right figure in part (a).

2.3 CNT forest adhesion to substrate

Adhesion strength of CNTs to the substrate is another critical property of substrate-supported CNT forests. Researchers have investigated the effects of microwaving [69], substrate [10], and LPCVD SiO_2 coating on the adhesion of the CNT forests to the substrate. Microwaving CNTs improves the adhesion by embedding the CNTs in a Ti underlayer [69]. Better adhesion has also been achieved on a carbon paper substrate compared to a SiO_2 substrate.[10] LPCVD SiO_2 coating of CNTs has also been reported to improve the adhesion of CNT forests to the substrate [47]. The majority of previous work to test CNT-substrate adhesion, however, has been qualitative using sonication [10, 69] or tape testing [47]. In the quantified tape testing methods [70, 71] shear stress for debonding of the CNTs from the substrate is measured to be 0.1-0.5 MPa for CNTs grown on metals (Fig. 2.3 [28]) and SiC. Lahiri et al. used a fully quantified nanoscratch test to measure the bonding strength of randomly oriented CNTs grown on a substrate. This method works by applying a compression load on the indenter to a specified load followed by a lateral load that debonds the CNTs from the substrate. No report of measurement of adhesion strength of CNT forest to substrates in tensile loading is available to the best of our knowledge. The tensile loading has been used for measurement of interface strength of CNT forests bonded using Ti/Au to other surfaces [72].

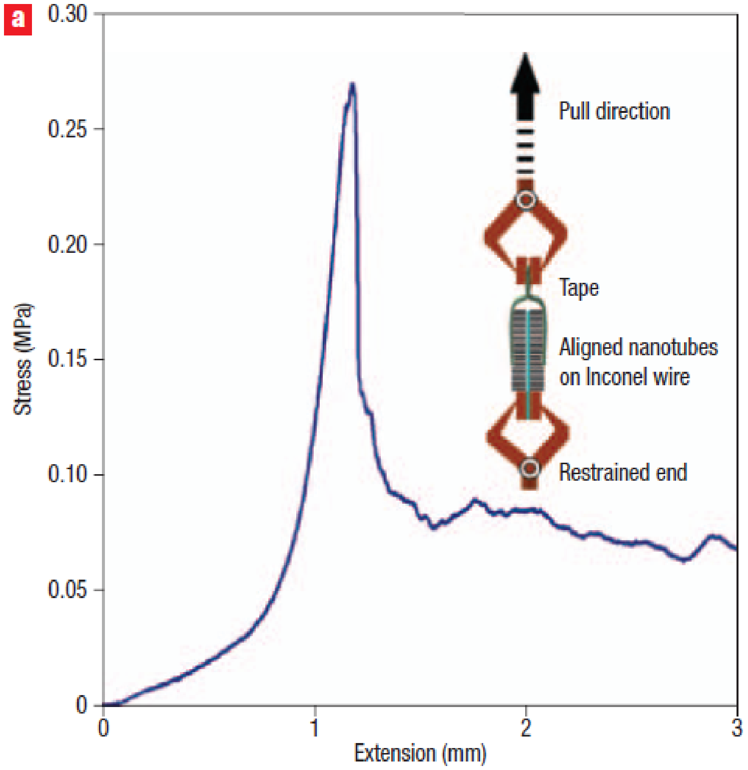

Fig. 2.3. Shear stress versus displacement in a tape test on CNT forests grown on an Inconel wire. The inset shows a schematic of the test setup [28].

2.4 CNT forest coating

Among various methods used by researchers to coat CNTs [24, 37-47], details of two methods that are used in this dissertation are as follows.

2.4.1 *Electron beam physical vapor deposition*

Electron beam physical vapor deposition (E-beam PVD) is a surface coating method that is known for relatively high deposition rate and high material use efficiency. The deposition takes place in a high vacuum chamber. A material is bombarded by an electron beam and the evaporated atoms are deposited everywhere in the vacuum chamber on the line-of-sight. This method is appropriate for coating of the top surface of a CNT forest. However, the side walls of the CNTs are not coated using this method since it is a line-of-sight method. A schematic is shown in Fig. 2.4.

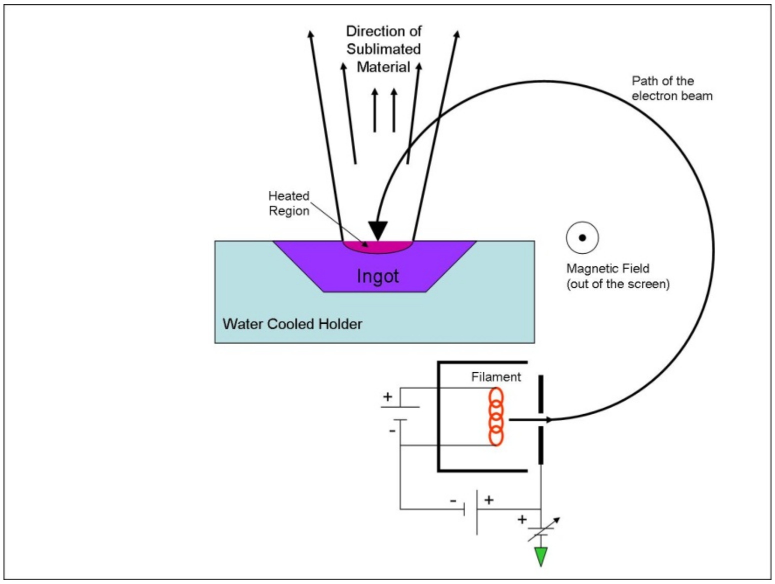

Fig. 2.4. A schematic of electron beam physical vapor deposition [73].

Cross et al. [72] coated CNT forests with Au using E-beam PVD for the purpose of bonding CNT forests to another surface and for transfer printing of CNTs. Au formed a discontinuous coating layer in the form of clumps on the top surface of the CNT forest (Fig. 2.5 [72]).

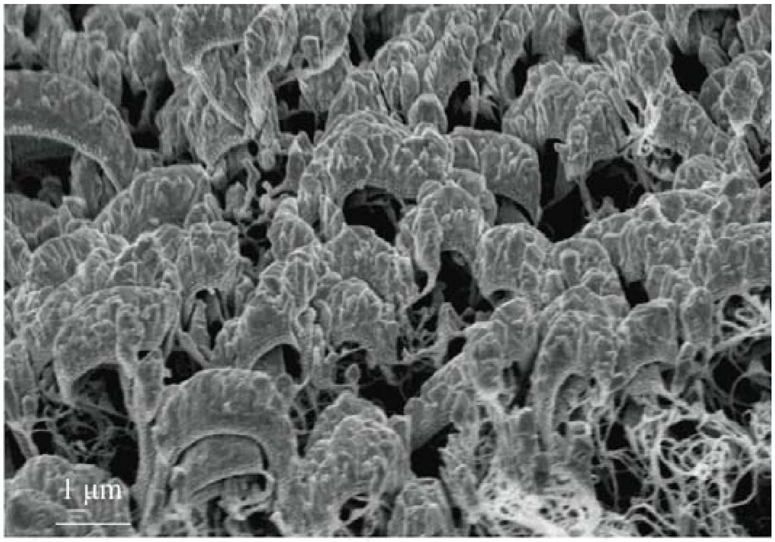

Fig. 2.5. Au coating on top of a CNT forest deposited by e-beam PVD method [72].

2.4.2 *Atomic layer deposition*

Atomic layer deposition (ALD) is a method of deposition of atomic-scale coatings. It is a relatively slow deposition process but has the advantage of coating high aspect ratio objects. Therefore, it can be used for coating the side walls of CNTs in a CNT forest to form hybrid nanotubes. The method cycles composed of two self-limiting steps (i.e. deposition of only one layer of atom or molecule in each step) by introducing the precursors into the chamber followed by purge or evacuation steps. For alumina deposition, for example, trimethyaluminum is the precursor for Al and water is the precursor for oxygen. A schematic of ALD deposition of alumina is demonstrated in Fig.

2.6. One layer of alumina is deposited in each cycle and the deposition rate is usually ~ 1.1 Å/cycle.

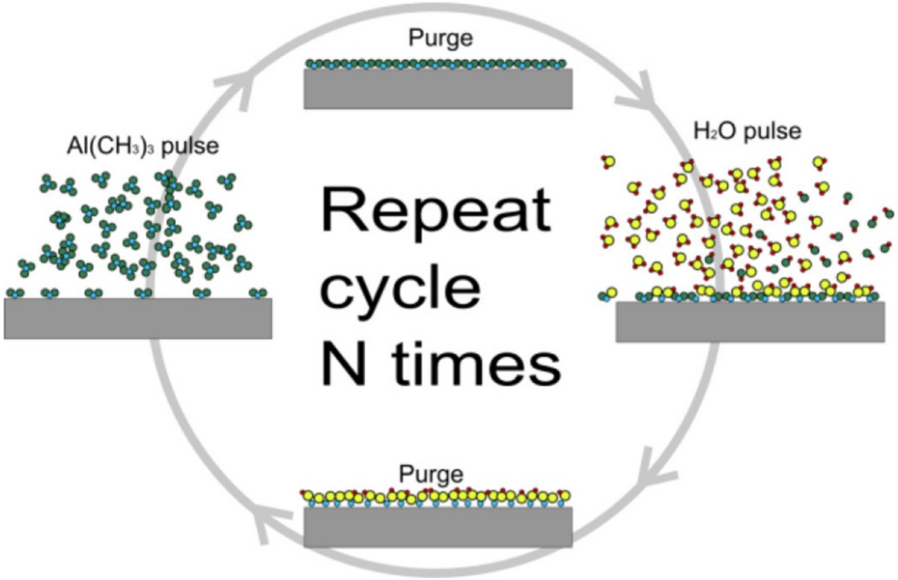

Fig. 2.6. Atomic layer deposition of alumina [74].

Using ALD, arrays of isolated CNTs have been coated with tungsten [46] and dispersed CNTs have been coated with transition-metal oxides [50]. Alumina, used in this dissertation, is a common ALD material that has been shown to behave well for isolating and insulating multiwall CNTs and as a seed layer for functionalizing the CNTs [49], and for enhancing the stability and capacity of CNTs as an anode in Li-ion batteries [42]. TEM images of ALD alumina coated CNTs are shown in Fig. 2.7. TEM image of dispersed CNTs coated with ALD alumina (Fig. 2.7,Fig. 2.8) show that CNTs are coated conformally with ALD alumina [39, 49].

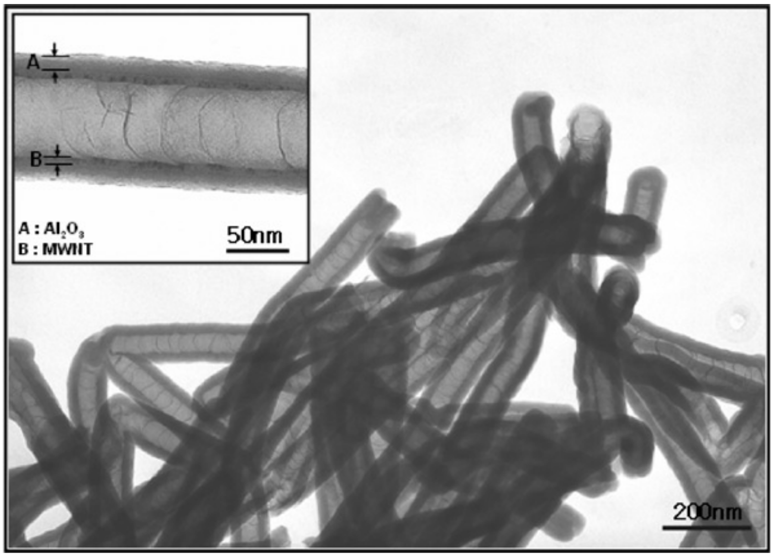

Fig. 2.7. TEM image of dispersed CNTs coated with ALD alumina [39].

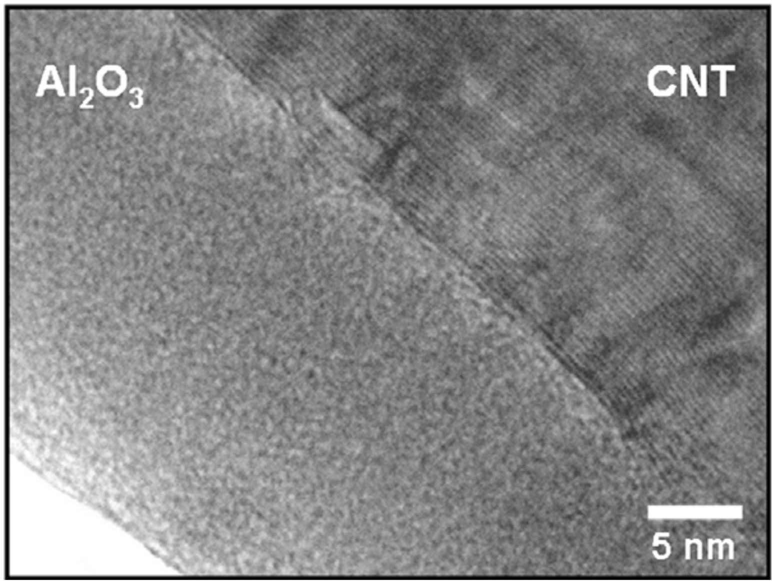

Fig. 2.8. TEM image of a MWCNT coated with 25 nm [49].

2.5 Nanoindentation

Nanoindentation is a small scale measurement of mechanical properties of materials. It is a non-destructive test for measurement of elastic modulus and hardness of thin films [75, 76]. In a nanoindentation experiment, load and displacement data are measured as indentation is made. A typical load-displacement curve is demonstrated in Fig. 2.9. Reduced elastic modulus is defined as

$$E_r = \frac{1-\nu^2}{E} + \frac{1-\nu_i^2}{E_i} \qquad \text{eq. 2.1}$$

where E and ν are the Young's modulus and Poisson's ratio for the specimen and E_i and ν_i are those for the indenter.

Reduced elastic modulus is calculated using

$$E_r = \frac{\sqrt{\pi}\, S}{2\sqrt{A}} \qquad \text{eq. 2.2}$$

where S is the stiffness of the top part of the unloading curve and A is the projected area of the elastic contact that is measured using area function of the indenter that is obtained experimentally by testing a material with known Young's modulus. Hardness (H), maximum mean pressure that material supports, can be calculated using

$$H = \frac{P_{\max}}{A} \qquad \text{eq.}$$

2.3

where $P_{\max}$ is the maximum load and A is the projected area at the maximum load. Use of nanoindentation for measurement of properties of CNT forests will be discussed in the next section.

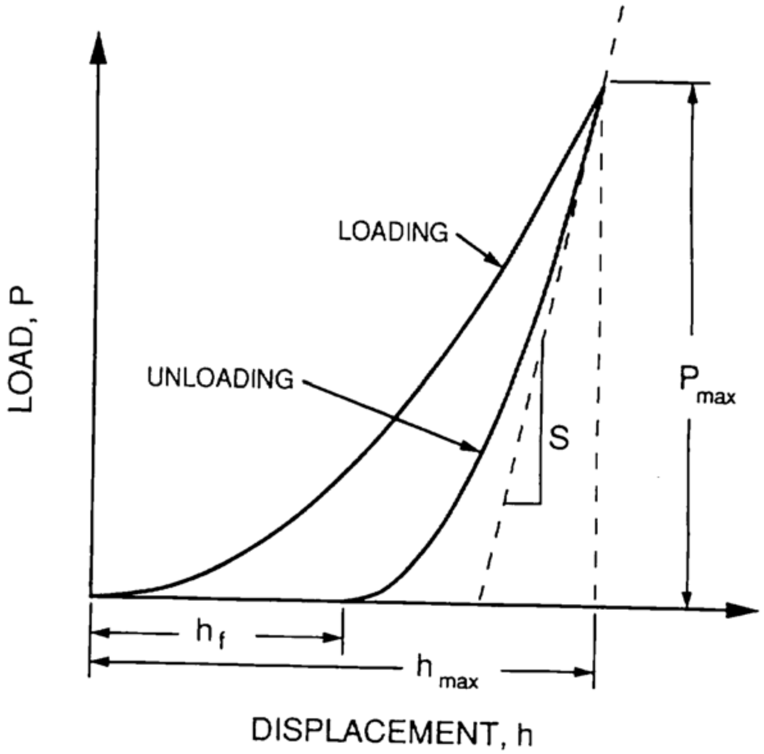

Fig. 2.9. A schematic representation of load-displacement curve for nanoindentation [75]. P_{max}: maximum load, S: stiffness, h_{max}: maximum displacement, and h_f: final depth of the indenter impression after unloading.

2.6 CNT forest mechanical behavior

McCarter et al. [11] used nanoindentation with a Berkovich tip (a three sided pyramid with a half angle of 65.35°) to measure the effective elastic modulus of CNT turfs. They showed that the effective moduli in compression of assemblies of CNTs (0.03-0.3 GPa) are orders of magnitude lower than the values for individual CNTs (higher than 1 TPa) [77]. Mesarovic et al. [15] showed that the reversibility of the deformation of CNT forests (their capability to be recovered to the initial state) caused by a Berkovich tip depends on the depth of the indentation. They related the high modulus of the CNT turf at the beginning of the indentation to the initial built-in bending strain energy of CNTs.

While CNTs are deformed mainly by local bending of the tips in nanoindentation using a Berkovich tip [78], they deform through a substantially different mechanism under pure compression loading. Deformation mechanism of free standing CNT forests under compression was reported by Cao et al. [17]. They observed buckling along the height of the CNTs in loading and unfolding to their near original shape in unloading. The stress-strain curve included three regions similar to the case of open-cell foams: (1) a stiff initial region, (2) a plateau region where buckles are forming, and (3) a densification region where stiffness increases. They also reported high compressibility and fatigue resistance of CNT turfs for thousands of cycles. Zbib et al. [79] observed coordinated buckling in the bottom layer of CNT turf pillars with different aspect ratios in compression. Their findings demonstrated that the initial buckle formed at nominal stresses of 4.3- 0.2 MPa. The buckling stress did not depend on the aspect ratio of the turf. Rather, it depended on the height and the effective modulus of the turf measured by local nanoindentation of the turf surface using a Berkovich tip. The stress-strain curve obtained from compression of the turf has a stress peak at the instability stress followed by a plateau with small stress oscillations due to formation of the other buckling wrinkles (Fig. 2.10). Hutchens et al. [19] performed in situ compression of micro-pillars that enabled a more detailed analysis of buckle formation in CNT bundles. It was found that buckles initiate from the surface of the pillar and subsequently propagate laterally in the structure. They found strain hardening and softening regions in the stress-strain curve that corresponded to the formation and propagation of buckles. The shape and size of the hardening and softening regions depended upon the strain rate although the wavelength of the buckles did not change with strain rate. Correlations between CNT forest morphology (e.g. density and orientation of CNTs) and the location of incipient buckling was suggested in the work by Cao et al. [17].

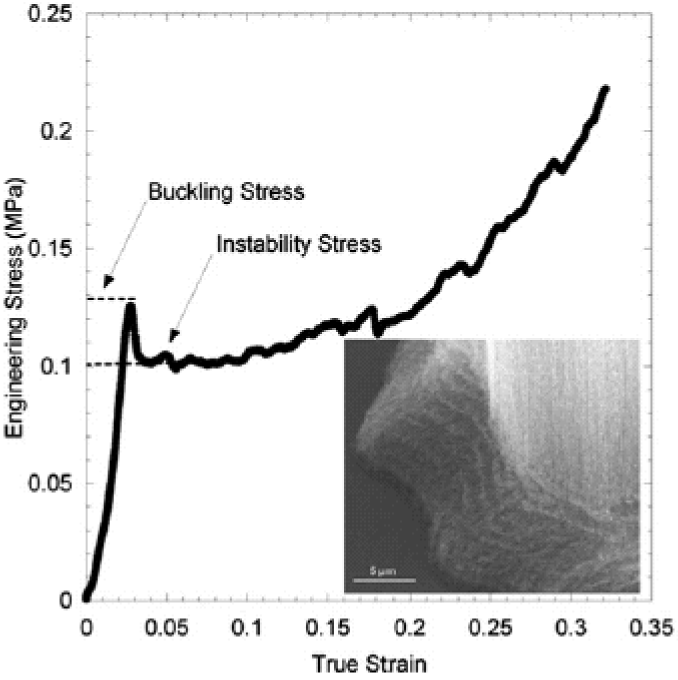

Fig. 2.10. Stress-strain curve for compression of a CNT forest pillar [30]. The SEM inset shows the formed wrinkles close to the base of the pillar.

Compression of CNT pillars advances the understanding of the deformation mechanism of CNT bundles. However, local indentation of CNT forests is a more realistic simulation of the real applications involving CNT forest contact with asperities of a rough surface. Indentation of a CNT forest is capable of showing the effect of interaction between CNTs directly and indirectly under the indenter on the deformation mechanism. A schematic of a pillar compression and an indentation experiment are shown in Fig. 2.11a, b respectively. The CNT forest surface in the case of indentation Fig. 2.11b shows schematically that deformations could expand beyond the CNTs directly under indenter due to interaction between CNTs. Maschmann et al. [21, 22] performed visualization of micro-indentation of CNT forest edges using a flat punch indenter. Buckling initiation from either bottom or top of the CNT forest was observed. Based on CNT morphology, two deformation mechanisms were observed for two types of CNT forests. A short forest with larger diameter (50 nm) and relatively straight CNTs has a column-like buckling behavior while longer CNTs with smaller diameters (10-20 nm) and more entanglement have a foam-like behavior (stress-strain curve composed of three regions: stiff-plateau-densification similar to a foam material).

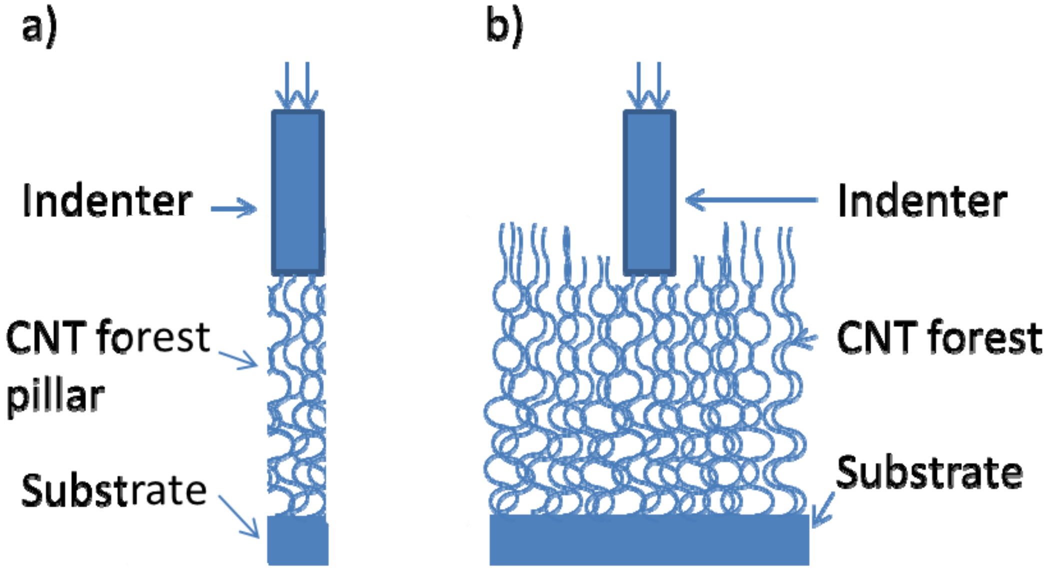

Fig. 2.11. Schematic comparison of compression of a CNT forest pillar versus CNT forest indentation. The indentation experiment shows the effect of interaction between CNTs under the indenter and those on the sides.

Previous results of the investigations of the mechanical properties and deformation mechanism of CNT forests are interesting and encouraging as those explain a wide range of mechanical properties (Table 1.1) and different buckling locations along the height of CNT forests [17, 19, 21, 22, 30]. Not all the questions could be answered in this dissertation. Instead, this dissertation addresses a few important issues. First, understanding of the effect of morphology gradients along height of the CNT forests on the deformation mechanism requires a comparison of CNT forests with distinct morphologies along their heights. This has not been the subject of previous investigations. Also, deformation mechanisms of coated and solvent-infiltrated CNT forests are still not well understood but are important because the knowledge is critical for the design of CNT forests involving interaction of CNT forests with other materials. Therefore, the objectives of this dissertation are as follows: finding direct relations between the growth-induced morphologies along the height and the micro-compression behavior, understanding the deformation and failure mechanism of CNT forests in macro-compression tests, and exploring the effects of top surface coating, conformal-coating, and solvent-soaking of CNT forests in their mechanical and failure behavior. The results are expected to advance the fundamental knowledge of CNT forests mechanical and failure behavior and suggest methods for tailoring the mechanical properties of CNT forests. This thesis is not focused on a specific application but the gained knowledge could be a baseline for the design of new nanostructures based on CNT forests.

CHAPTER 3 EFFECTS OF MORPHOLOGY ON THE MICRO-COMPRESSION RESPONSE OF PRISTINE CARBON NANOTUBE FORESTS

The in situ testing was performed in Dr. Greer's lab at California Institute of Technology. The author thanks Dr. Julia R. Greer and Dr. Shelby B. Hutchens for their help. This chapter is partly reproduced from Pour Shahid Saeed Abadi et al., Nanoscale 4, 3373 (2012).

3.1 Introduction

The morphology of CNTs and interaction between them change along the height of each CNT forest [17, 19, 65, 67]. The previous studies on the mechanical behavior of different CNT forests showed that mechanical properties such as modulus and stiffness could differ from sample to sample [11-14]. Moreover, local periodic buckling, which has been observed to the dominant deformation mechanism in compression of CNT forests, have been shown to begin at different locations along height such as bottom [17, 19, 22, 30] or top[21, 22] of the CNT forests. However, there is no literature on the mechanical testing of CNT forests that differ only in the vertical morphological gradients while maintaining all other aspects constant. This is required to investigate the connection between the structural variations within a forest and the mechanical response of the forest. Therefore, the relation between the morphology of CNT forests and their mechanical behavior is still not clear and requires further investigation. This chapter aims to advance the knowledge of this expectedly complicated relationship.

This work reports the results of a series of in situ flat-punch indentation experiments on CNT forests with distinct microstructural vertical gradients performed inside a dedicated nano-mechanical instrument, SEMentor, comprised of a scanning electron microscope (SEM) and nanoindenter module[80]. The microstructure of CNT forests was varied by changing CNT growth time, using different conditions for CNT growth (*e.g.*, pressure, gas flow rates, *etc*.), or by using a plasma treatment to create different catalyst morphologies prior to growth. The main differences between the forests studied were the relative change of morphology along the height of forests while the diameter of the CNTs was very similar between all forests. These differences were quantified by measurement of mass and aerial density and CNT average orientation along the height of each type of CNT forest. The location of initial instability (*i.e.*, lowest critical buckling load) or bending for CNT forests under a compressive load is revealed through the in situ analysis which allows for detailed comparisons between all samples.

3.2 Methods

3.2.1 CNT forest growth

Three types of CNT forests were grown on Si substrates coated with Ti (30 nm)/Al (10 nm)/Fe (3 nm) by electron beam evaporation. A commercial chemical vapor deposition system (Black Magic Pro 4”, Aixtron SE) was used for CNT growth on the catalyzed substrates. This tool and the growth chamber at the time that plasma is on are shown in Fig. 3.1. Low pressure CVD (LPCVD), near atmospheric pressure CVD (APCVD), and plasma pretreated LPCVD (P-LPCVD) recipes were used for synthesis of CNT forests.. The growth temperature was ~750 °C and acetylene was used as the carbon source gas in all three recipes. The chamber pressure was approximately 10 mbar in LPCVD using a C_2H_2/H_2 mixture and 720 mbar in APCVD using a $C_2H_2/H_2/N_2$ mixture. The P-LPCVD recipe was a modification of the LPCVD recipe that included a 120 W hydrogen plasma pretreatment of the catalyst layer for 5 min prior to growth. Each recipe produced multiwall CNTs with diameter ranges determined by transition electron microscope (TEM) to be 7.2 ± 1.4 nm for LPCVD CNTs, 8.8 ± 2.1 nm for APCVD CNTs, and 9.3 ± 5.5 nm for P-LPCVD CNTs. A representative low magnification image of a CNT forest grown with LPCVD is shown in Fig. 3.2 and representative TEM images of all three types of CNT forests are shown in Fig. 3.3. Aerial densities at the beginning of the growth were expected to be close for LPCVD and APCVD since the catalyst profiles are similar. However, the different growth conditions were used to create two different morphologies along the height of the forests as the pressure influences the growth rate and structural morphology within the forests. This plasma pretreatment acts to remove some catalyst particles and resulted in a forest with lower density. Details of the growth conditions for each sample are listed in Table 3.1.

Fig. 3.1. Black Magic Pro 4” CVD system. Left: growth chamber when plasma in on, and right: the outside look of the system.

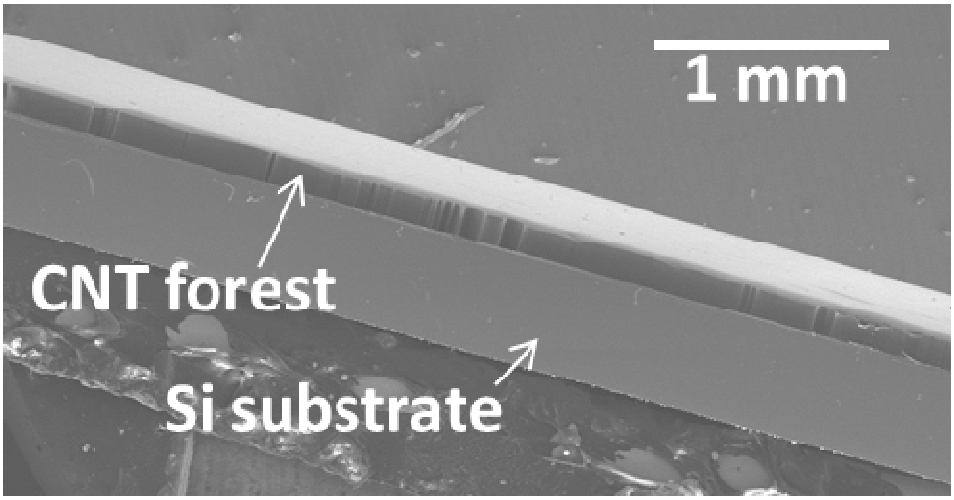

Fig. 3.2. Low magnification SEM image of a CNT forest grown on a Si substrate.

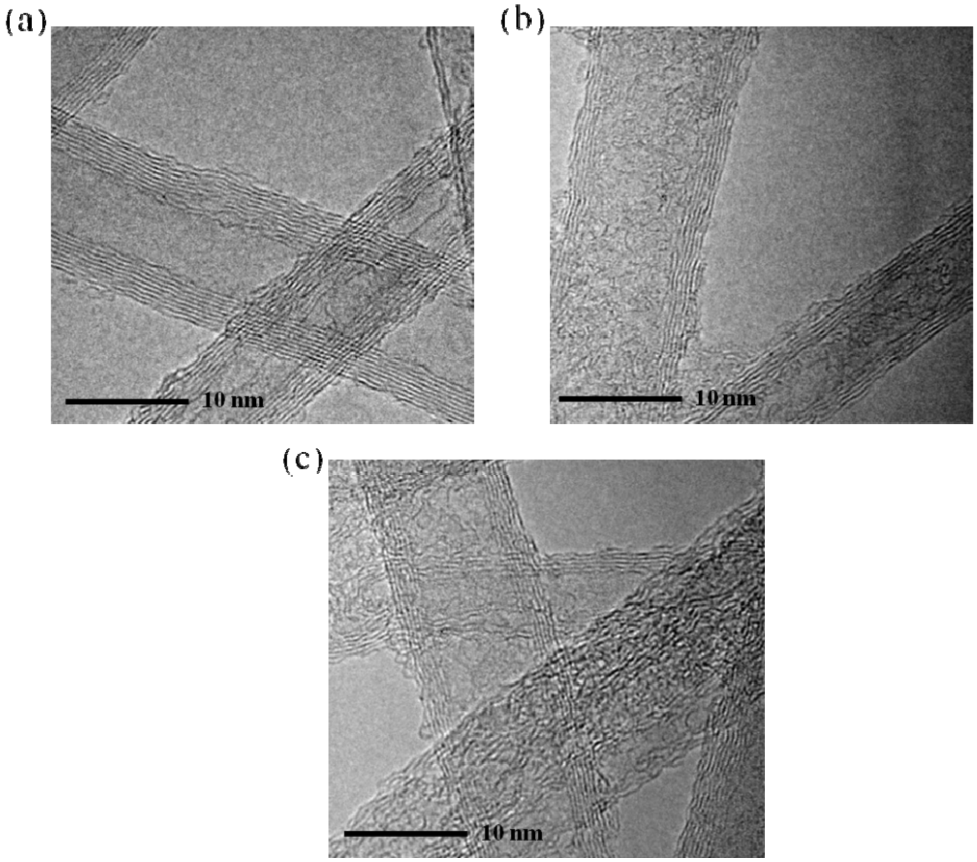

Fig. 3.3. TEM images taken by JEOL 4000EX from CNTs grown with a) LPCVD, b) APCVD, and c) P-LPCVD method.

Table 3.1. Parameters for LPCVD, APCVD, and P-LPCVD recipes.

Recipes	Growth duration (min)	Height (µm)	Temperature (°C)	Pressure (mbar)	Gas rates (sccm)			Pretreatment
					Acetylene	H_2	N_2	
LPCVD.shortest	2.5	70	750	10 mbar	100	700	-	-
LPCVD.medium	5	175						
LPCVD.tallest	15	285						
APCVD	30	110	750	720 mbar	160	100	7500	-
P-LPCVD	5	30	750	10 mbar	100	700		DC Plasma 120 W-5 min

3.2.2 Characterization of CNT Forests

The morphological differences between the three types of CNT forest were quantified by measuring the mass density (CNT mass divided by volume), aerial density (number of CNTs per unit area), and orientation (average deviation of CNTs from vertical orientation) at different points along the height of each forest type.

The LPCVD, APCVD, P-LPCVD recipes were used to grow CNT forest samples at different durations on 1 cm x 1 cm silicon substrates to create samples of different heights, and therefore – of different mass densities along the height of CNT forests. Other growth parameters were held constant for each recipe. A precision microbalance with 10 μg resolution was used to measure the mass of CNTs added to the substrate for each growth time and the heights of all samples were measured by taking several side view images in SEM. The volume of each forest was calculated by multiplying the average height by the area in which the CNT forest was grown. The average mass density as a function of normalized height (height divided by maximum obtained height for the same forest type) was calculated by dividing measured masses by volumes and is shown in Fig. 3.4a. The error bars show the standard deviation of several measurements at each point.

The mass density at each point along the height of a forest can be estimated from the measured average densities shown in Fig. 3.4a using

$$\rho_n = \frac{\rho_{avg,n}\, h_n - \rho_{avg,n-1}\, h_{n-1}}{h_n - h_{n-1}} \qquad \text{eq.3.1}$$

where ρ_{avg} is the average density, h is the height, and n-1, n are two adjacent points in average density vs. height data. The average densities interpolated using curves fitted to data in Fig. 3.4a were used in eq.3.1 to calculate mass densities. The resultant mass density vs. normalized distance from top surface (vertical distance from top surface divided by the height) is plotted in Fig. 3.4b.

As evident from Fig. 3.4b, the LPCVD forest displayed the highest relative change in mass density from top to bottom, and it appears that the gradient was almost constant along the height. APCVD forests displayed the same mass density gradient as LPCVD in the top half, but it showed a minimum density at the middle. Its mass density then increased from middle to bottom. P-LPCVD forests showed a relatively constant density along the height of the forest.

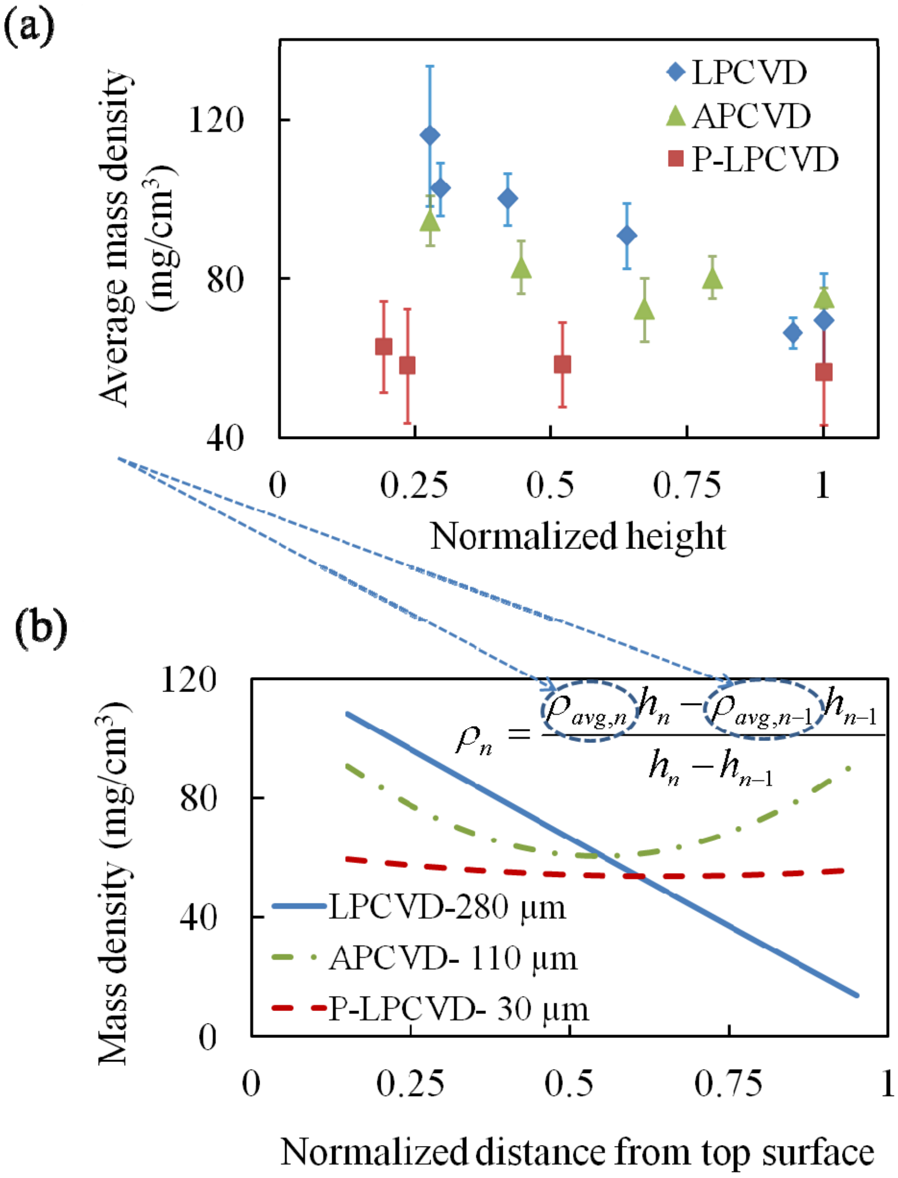

Fig. 3.4. Density data for the three types of CNT forests. a) average mass density vs. normalized height, and b) density vs. normalized distance from top surface; the solution to eq. 3.1.

The mass density depends on the orientation of CNTs and the areal density of the CNT forest (*i.e.*, number of CNTs per unit area of substrate) in each point along the forest height. Therefore, both orientation and areal density have to be compared for positions along the height of each type of CNT forest to help explain the trends observed in the mass densities. CNTs were counted along horizontal lines drawn across high magnification (400 kX) SEM images of the side view of CNT forests in different positions along the height of each CNT forest. The effective depth of field [13] (depth in which CNTs were counted) was held constant as much as possible by using similar SEM parameters (aperture radius, working distance, voltage, brightness, and contrast) to capture all images. The number of counted CNTs per unit length as a function of normalized distance from the top surface is plotted in Fig. 3.5. CNTs were counted along at least 18 lines for each data point and the average values are plotted in this figure. Generally, the areal densities can be calculated by dividing the number of counted CNTs per unit line by an effective depth of field, if it were known. For this study, we use the trends reported based on the counted CNTs per unit length (Fig. 3.5) to compare the areal densities since the depth of field is expected to be similar for all samples viewed in SEM here.

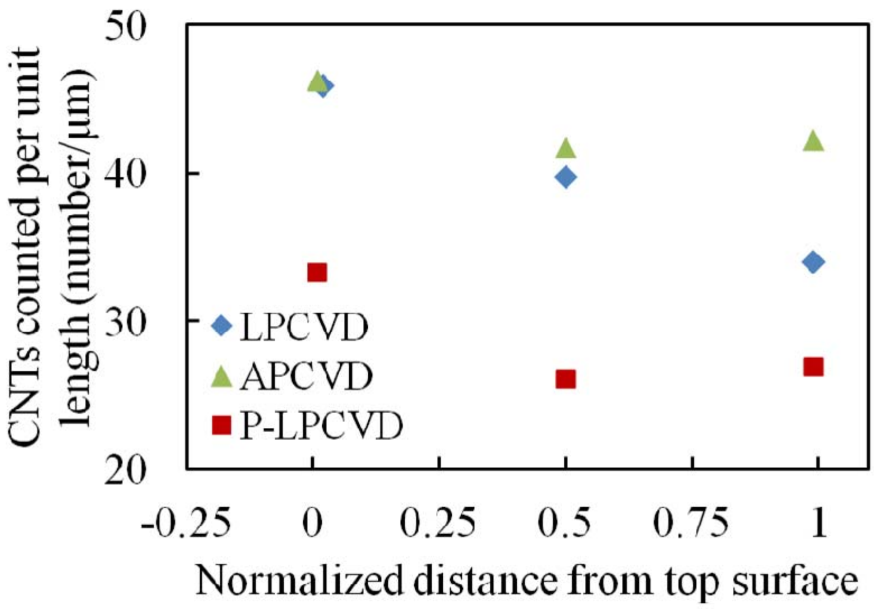

Fig. 3.5. counted CNTs per unit length vs. normalized distance from top surface for the three types of CNT forests.

We quantified the orientation of individual nanotubes in different sections along the height of each CNT forest by measuring their average offset angle from the vertical direction (0-90 degrees in either clockwise or counterclockwise direction) based on 400 kX-magnified SEM images. At such a high magnification, the individual nanotubes can be approximated as straight lines, and the angles between them and the normal direction can be calculated (an example processed image is shown in Fig. 3.6). The offset angle averaged over at least 70 linear CNT segments is plotted in Fig. 3.7. The larger angles in the microstructure were found in morphologies that had more randomly oriented CNT segments, which was an indication of the tortuosity of the forest.

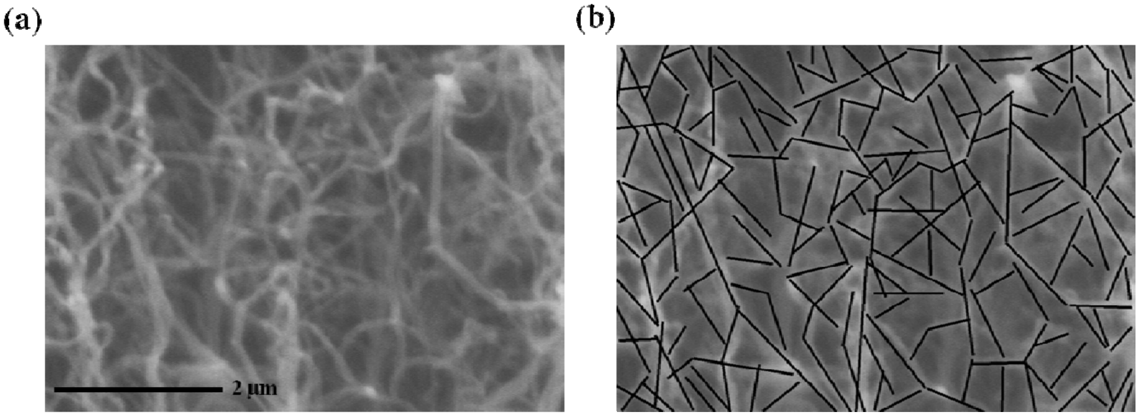

Fig. 3.6. a) A sample high magnification (400 kX) SEM image used for CNT counting and orientation measurements showing highly entangled CNTs at the bottom of a LPCVD forest. b) Left image with straight lines drawn on CNT pieces for the calculation of average angle between CNTs and vertical direction.

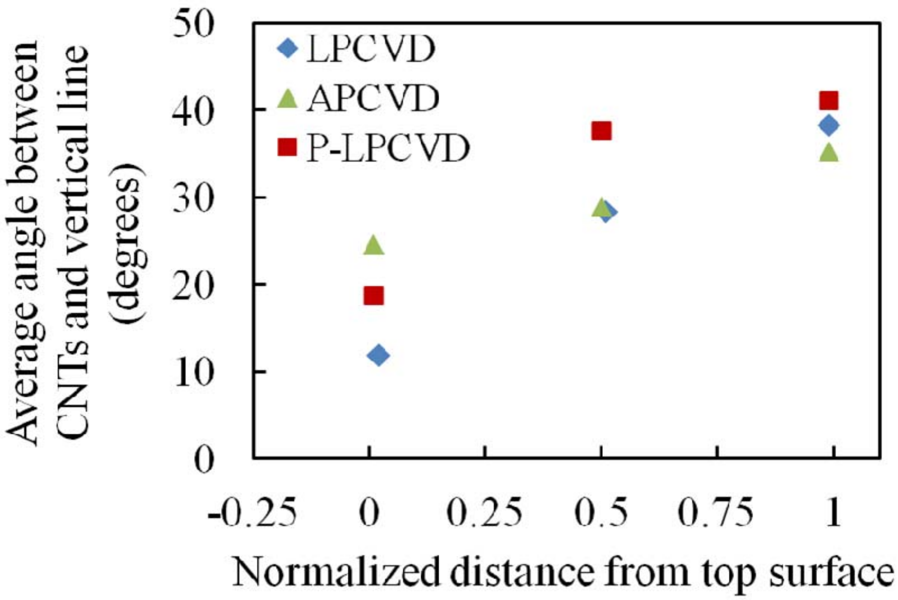

Fig. 3.7. Average angle between CNTs and vertical line vs. normalized distance from top surface for the three types of CNT forests.

Based on this methodology, Fig. 3.5and Fig. 3.7 show an overall decrease in areal density and increase in the average orientation angle from the top to bottom of all three forests types. However, the different gradients in areal density and change in orientation along the heights produced different trends in the change in mass density for LPCVD, APCVD, and P-LPCVD forests. We found the areal density of LPCVD forests to decrease linearly from top to bottom (Fig. 2c), which is consistent with the trend shown in the point mass density data (Fig. 2b). There is a significant difference between the areal densities measured in the top and middle parts of APCVD and P-LPCVD forest, yet the measured areal densities are practically constant for these forest types in the region spanning from the middle to the bottom (Fig. 2c). The mass density of APCVD forest decreased from the top to the middle (Fig. 2b), which is consistent with the measured decrease in the areal density (Fig. 2c). We attribute the increase in mass density from the middle to the bottom of APCVD forest to the increase in orientation angle from the middle to the bottom of the forest combined with a nearly constant areal density in this region. The relatively constant mass density of P-LPCVD forests (Fig. 2b) despite their larger areal density on top compared to the other regions (Fig. 2c) was due to the high degree of alignment on the top as compared with the underlying regions (Fig. 2d).

3.2.3 Mechanical testing

Nanoindentation testing was performed in a custom-built in situ nanomechanical testing instrument, SEMentor, comprised of a nanoindentation arm (Nanomechanics Inc.) inside a field emission scanning electron microscope (SEM) (FEI Quanta200 FEG)[80]. The schematic is shown in Fig. 3.8. All samples were loaded and unloaded at a constant displacement rate of 50 nm/s using a custom-machined, rectangular cross section (60 μm × 80 μm) diamond flat punch indenter tip (Fig. 3.9). To detect the top surface, an oscillating load was applied when indenter was approaching the surface. The surface was detected with measurement of the harmonic stiffness as large as 50 N/m. Nanoindentation experiments were performed by loading to a maximum displacement of 20-30 μm followed by complete unloading. The instrument's contribution to the measured raw load-displacement response of the samples was obtained by performing an identical test in vacuum and subtracting these load values from the CNT forest experimental data. In situ videos were recorded along with load-displacement data that could be matched to find out the deformation characteristics of the material and the load-displacement curve.

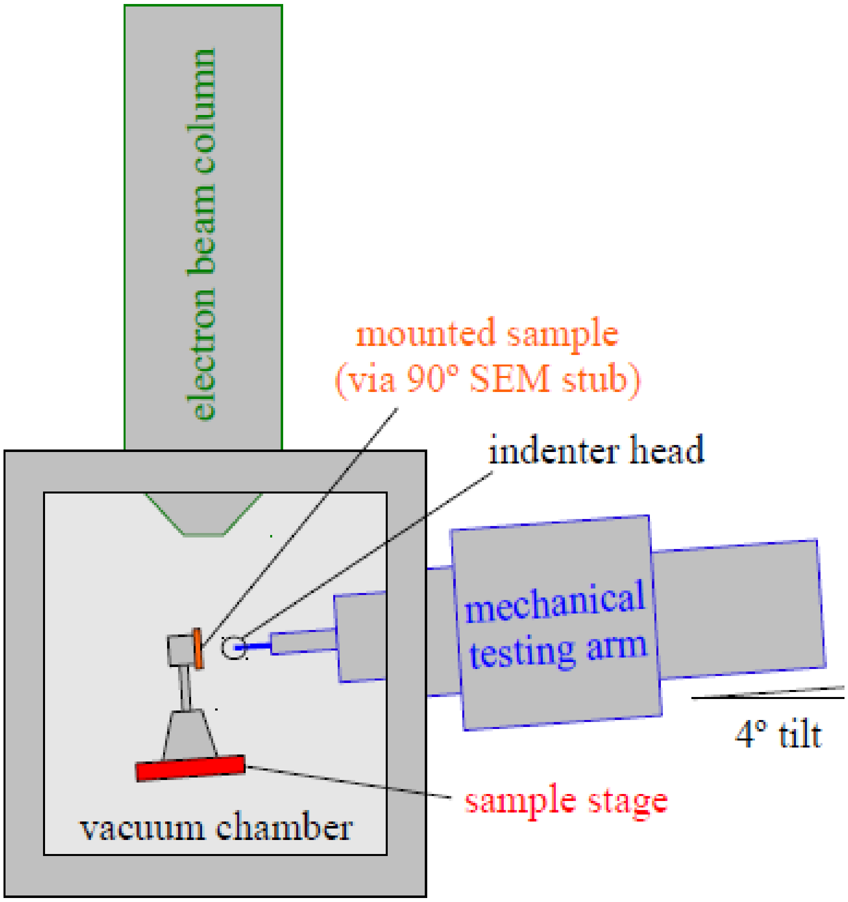

Fig. 3.8. A schematic of SEMentor, the in situ nanoindentation instrument (in California Institute of Technology) [81].

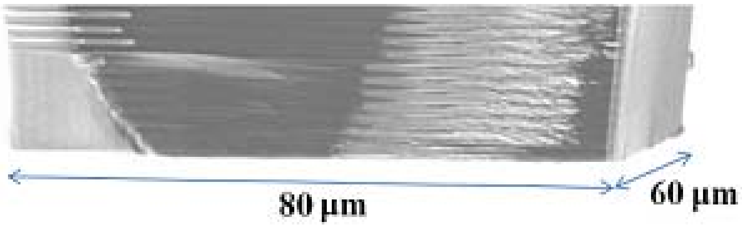

Fig. 3.9. Flat punch tip used in the experiments.

Besides the tests performed in the bulk regions of the CNT films, several indentations were performed along the cross-sectional edges for each sample in order to visualize the deformation in SEMentor (See Fig. 3.10). While the boundary conditions and constraints for these on-edge indentations are different from the in-bulk tests, they are helpful to elucidate some of the specific aspects of deformation mechanisms for each growth condition. A minimum of two on-edge indentations were performed on each sample and all observed deformations for a given sample were similar. Moreover, the distance between the indentation points were large enough (a few times larger than the indenter width of 80 μm) to prevent adjacent locations on a sample from influencing deformation characteristics. Also, in-bulk locations were selected as far as possible from the edge to ensure that the deformation is not affected by the free edge.

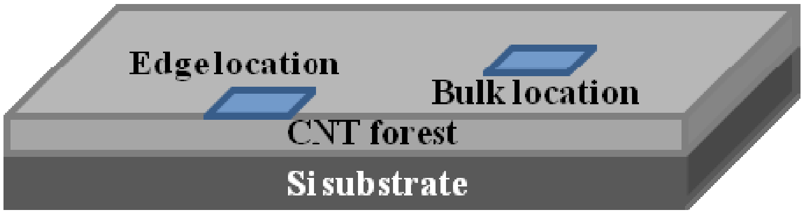

Fig. 3.10. Schematic diagram (not to scale) of on-edge and in-bulk locations.

3.3 Results and Discussion

LPCVD CNT forests of three heights (70, 190, and 280 μm) were indented to depths of 20-30 μm. The axial indentation strain was calculated by dividing the measured vertical displacement by the initial height of each forest. The axial indentation stress was calculated by dividing the applied force by the area of contact between the indenter and the surface of CNT forests. Use of a flat punch makes the calculation of the axial indentation stress more straightforward because the apparent contact area does not change during indentation, as it does for sharp indenter tips like Berkovich or a cube corner.

The deformation of the CNT arrays after indentation is shown in Fig. 3.11. In the case of 70 μm and 190 μm tall LPCVD forests, it appears that the local progressive buckling started at the bottom of the forest at the very beginning of the compression tests. Multiple curved shape buckles formed close to the substrate as shown in Figs. 2.a, b. This region for the 190 μm forest is magnified in Fig. 3.11d. The buckles exceeded the projection of the indenter cross-sectional width and the widest buckles are as large as 2-4 times the width of the indenter. The characteristic wavelength of the buckles was about 1-4 μm, in the same range with previous work with similar CNT types [21, 22]. The bottom progressive buckling continued from the very low measured strain to about 0.10-0.15 strain. At this point, a small number of buckles formed along the height and vertical shear offsets started forming along the vertical projection line of the indenter edges. For the case of 280 μm tall LPCVD forest, the position of the first local buckle was not at the bottom, as is the case for the forests with 70 μm and 190 μm heights, but rather it was approximately 100 μm, above the bottom of the CNT forest as shown in Fig. 3.11c. Also, a single buckle formed at the initial buckling location as opposed to formation of multiple buckles close to substrate (Fig. 3.11d) in the case for the two shorter forests.

The typical stress-strain curves for the on-edge indentation of LPCVD forests with different heights are shown in Fig. 3.12a. The initial sections of the stress-strain curves were linear with similar slopes for the samples of all three heights (Fig. 3.12a) followed by a nonlinear deformation response that depended on the height of the forest. Again all samples were deformed to approximately the same total depth, but the strain is smaller in samples with longer CNTs because the deformation is normalized by the CNT height for calculation of strain. In Fig. 3.12b, the stress-strain curves for the on-edge and in-bulk locations on a 70 μm tall LPCVD forest are compared. As expected, the maximum applied force was higher for the bulk locations as compared with the edge due to the boundary constraints in the former. For 70 μm tall forest the maximum stress was 1.3 MPa for a bulk point compared to 1 MPa for a point on the edge as shown in Fig. 3.12b. Again the slopes of the initial linear sections were similar. Based on our in situ observations, it appears that the points of discrete drops in load likely correspond to the initiation of buckles or vertical shear offsets. Further, we find that similar global softening regions after the peak points in the stress-strain curves for 190 and 280 μm tall forests were caused by the instabilities due to the formation of additional buckles above the initial one (s), as shown in Fig. 3.11. The undulations in the curve for the 70 μm tall forest were related to the progressive buckling initiated from the substrate. These undulations were very similar to previous observation of undulations in a stress-strain curve due to periodic buckling initiated from the substrate in the case of CNT pillars[19, 22, 30, 82].

Formation of periodic buckles initiated from the substrate in the case of medium height (190 μm) CNT forest did not cause such prominent undulations in the stress-strain curve as in the case of short (70 μm) height CNT forest. This is likely due to the effect of the larger CNT forest height, which makes the ratio of the buckled region to the entire height smaller and causes a smaller decrease in load *via* buckling.

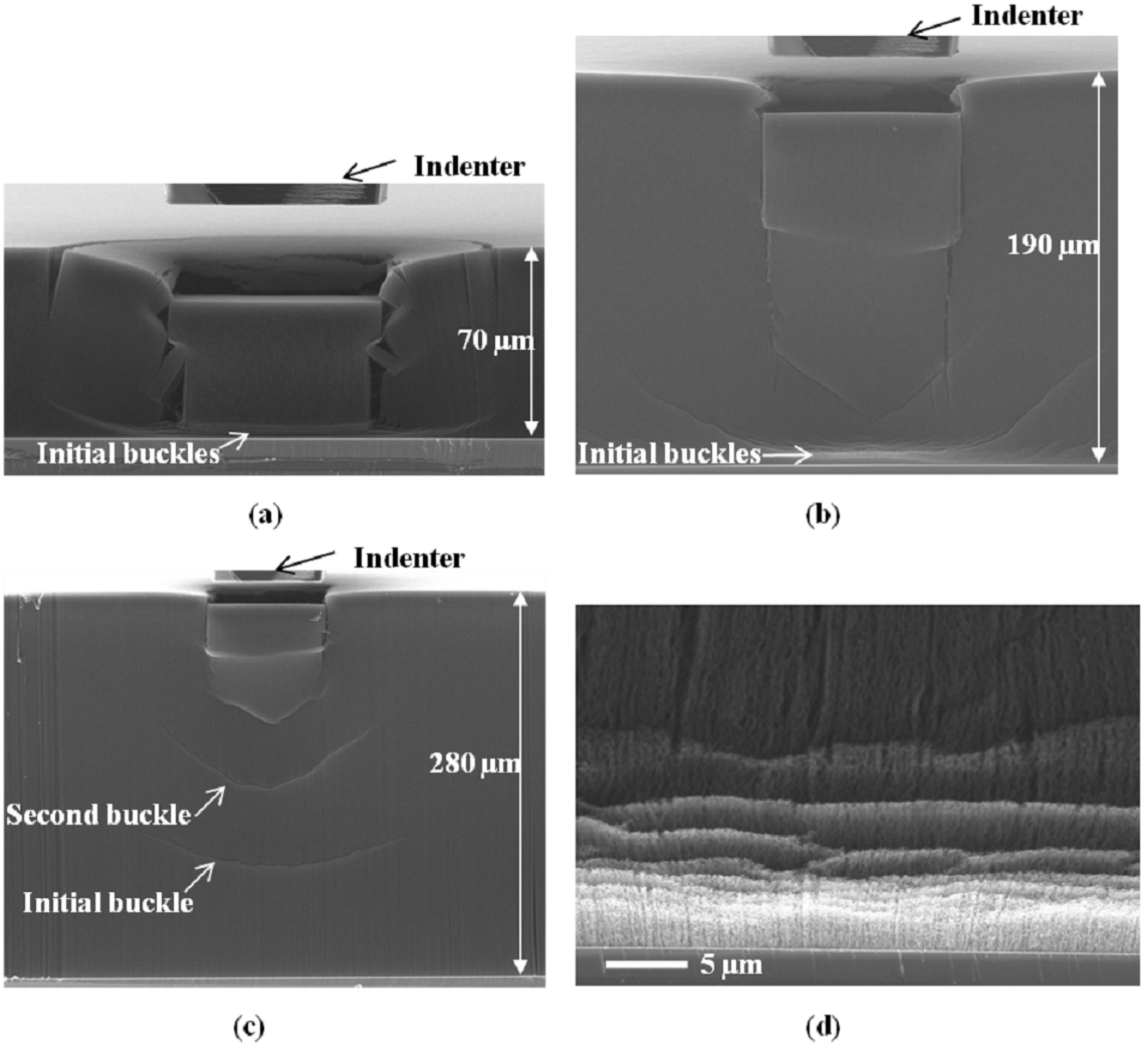

Fig. 3.11. CNT forest edge after indentation of LPCVD forest. a) shortest, b) medium, c) tallest forest, and d) magnified view of local buckles close to substrate in medium case which is also representative of shortest case.

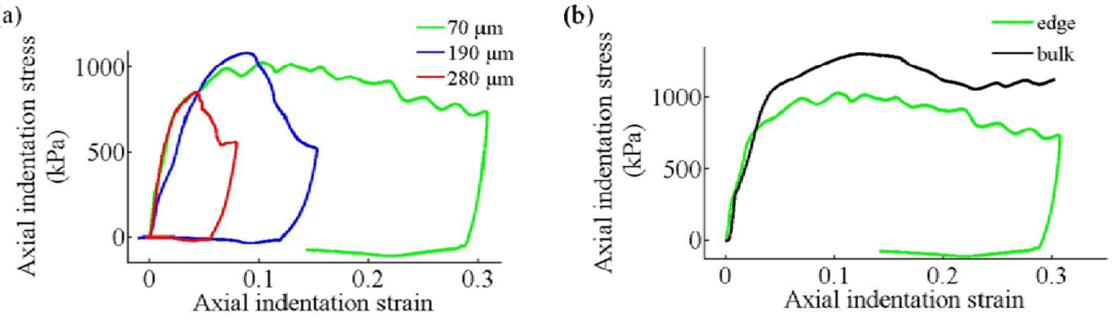

Fig. 3.12. a) Axial indentation stress-strain curves for indentation on the edges of LPCVD forests of three heights. b) Axial indentation stress-strain curves for shortest LPCVD forest for edge and bulk points.

A typical deformed APCVD CNT forest is shown in Figs. 4a-c. When an APCVD CNT forest with a height of 110 μm was indented on the edge to a strain of ~0.02, the initial buckle formed at a distance of 40-50 μm from the top surface representing ~35-45% of the total height. Such formation of the first buckle in the upper half of the APCVD forest did not occur in any LPCVD forests, suggesting the existence of significant differences in the forest morphology between these two types of CNT forests. A zoomed-in view of the region where the initial buckle occurred is shown in Fig 6b. The typical stress-strain curves for locations on the edge and in the bulk of the APCVD forest are shown in Fig. 3.13d. The stress-strain data from the edge showed a very small drop in stress at a strain of approximately 0.02 as the result of the initiation of the first buckle in the forest. We assume that the similar drop in load in the bulk indentation curve at a strain of about 0.04 was due to the formation of buckles as well.

At the strain of ~0.05, the second buckle formed ~10 μm above the first one in the APCVD samples, upon which the compressed section sheared off vertically underneath the indenter edges. The larger drops in stress – on the order of 500-800 kPa – for both curves correspond to these points. Fig. 3.13c shows a magnified view of the out-of-plane deformation and the location of the second buckle. Notably, the drop in load for the edge indentation was 1.5 times that in the bulk of the sample, probably as a result of reduced side constraints, which allowed the separated block to deform (see Fig. 3.13a). The sheared-off block of CNT forest under the indenter (Fig. 3.13a) is smaller than that of LPCVD forests. This precipitous drop in load was not observed in the stress-strain curves for LPCVD forests due to the small block of the deformed APCVD sample separating from the parent matrix as opposed to the LPCVD forests, where this did not occur.

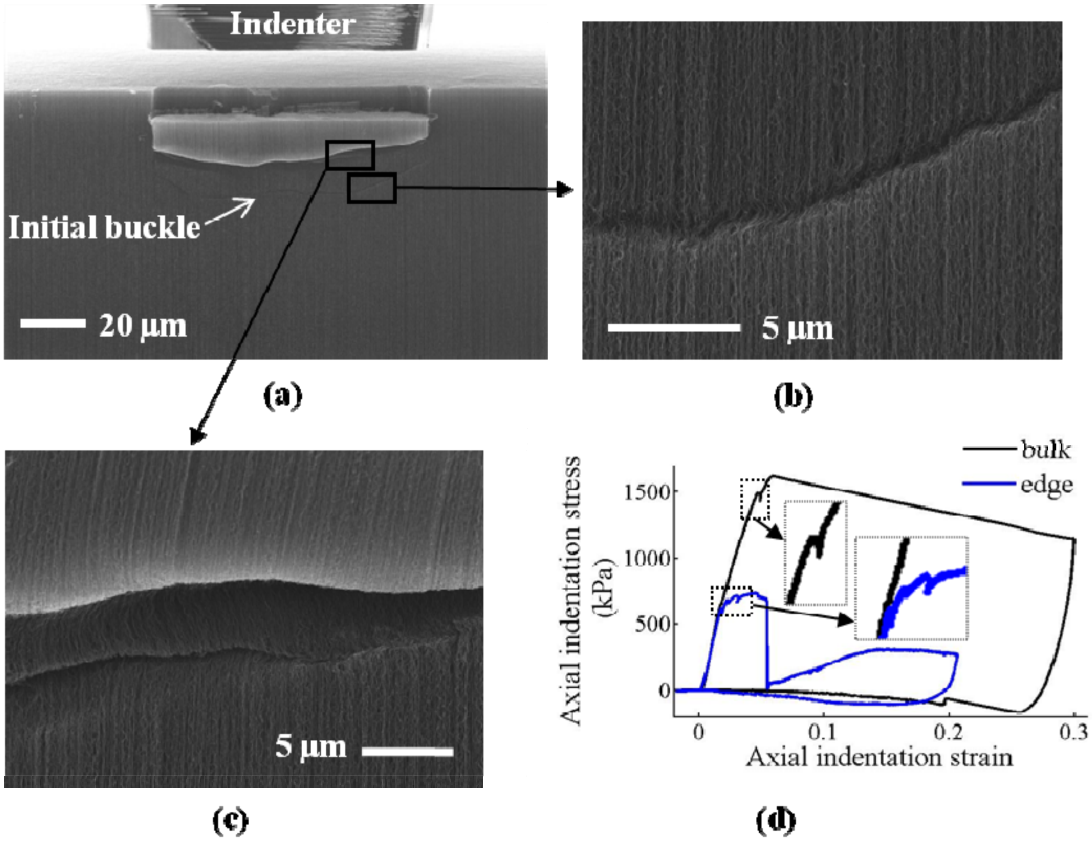

(a) (b)

(c) (d)

Fig. 3.13. a) APCVD CNT forest edge after indentation, b,c) high magnification view of the details of buckles inside rectangles in (a), d) Axial indentation stress-strain curves for edge and bulk points.

SEM images of the deformed P-LPCVD forests and a typical stress-strain curve for the on-edge and in-bulk points are shown in Fig. 3.14. This deformation started with bending of the CNT tips in contrast to what was seen in the LPCVD samples. The top image in Fig. 3.14b is the indenter in contact with CNT tips at the beginning of deformation and the bottom image shows the same point after additional displacement of the indenter causes CNT tips to bend enough to appear clearly in the image. At the strain of ~0.15-0.2, two buckles formed – one in the top 20% and another – in the bottom 80% of the forest height for both edge and in-bulk curves. The formation of these buckles corresponds to the first plateau region followed by the first hysteretic loop in the curves shown in Fig. 3.14d.

The out-of-plane deformation that was increased by continued displacement after formation of buckles is shown in the top-view SEM images in Fig. 3.14c. We attribute the formation of additional hysteretic loops in the stress-strain curves with further compression of the CNT forest to buckling of segments of forest under the indenter that could not be visualized in our testing (these segments are covered from view by the buckled layer). The initial parts of the curves for the indentation test of the P-LPCVD forest both on the edge and in-bulk are similar, as is the case for the APCVD and shortest LPCVD forest; however, the extra constraints on out-of-plane displacement in the in-bulk testing lead to higher stiffness at larger displacements as shown in Fig. 3.14d.

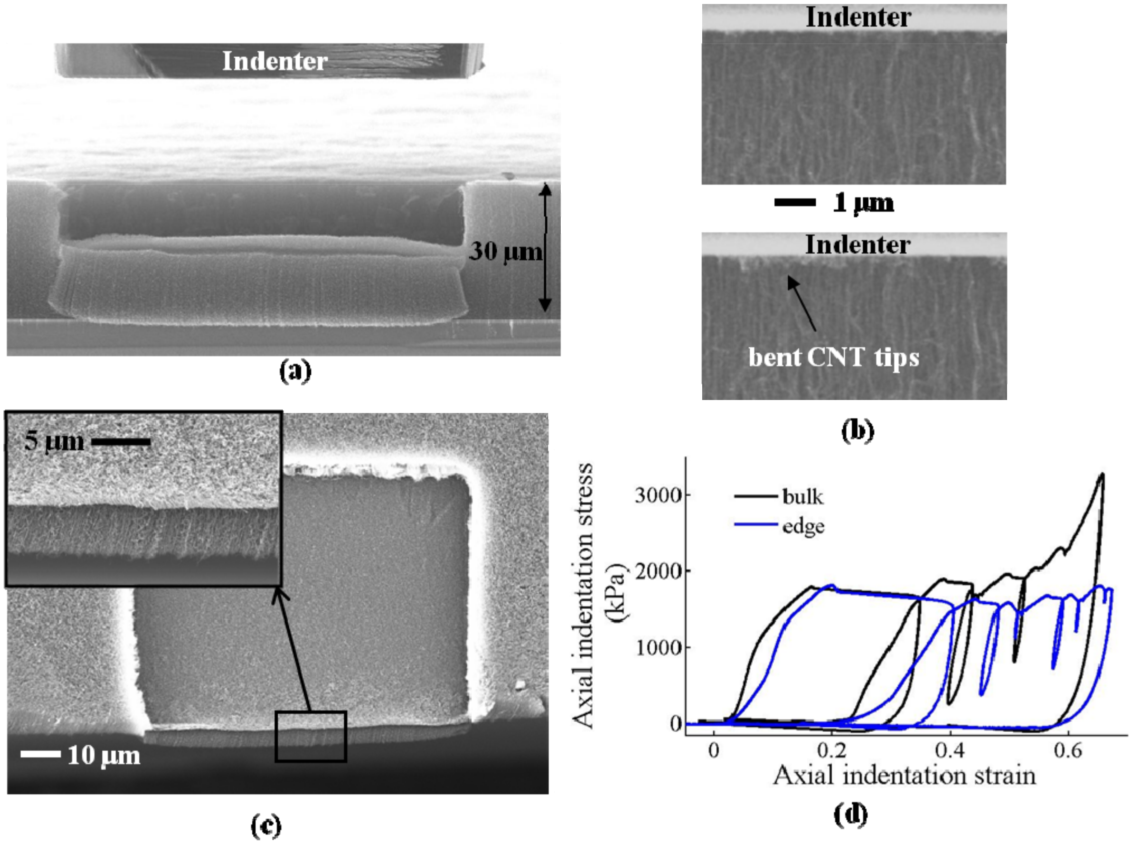

Fig. 3.14. Indentation of a P-LPCVD forest on edge. a) side view of the deformed spot, b) side magnified view of the section under indenter before (top image) and after (bottom image) appearance of CNT tips, c) top view of the deformed spot with magnified view of the out of plane deformation in the drawn rectangle, d) Axial indentation stress-strain curves for edge and bulk points.

The change of the growth recipes resulted in significantly different morphologies along the height of the CNT forests. The aforementioned deformation mechanisms of the CNT forests are connected to the different microstructures along their cross-sectional height. The change of microstructure of the LPCVD forests with height is demonstrated in the high magnification SEM images in Fig. 3.15. The images are taken from three locations near the top, bottom, and a point in between which is at the middle of the 70 and 180 μm tall CNT forests and below the middle where the first buckle formed in the 290 μm CNT forest. The images illustrate well-aligned and high density CNTs on the top sections of the CNT forests with three different heights. CNTs appear to become more tortuous at the middle and bottom sections of the forests. CNT aerial density was shown in Fig. 3.5 to decrease from top to the bottom of the CNT forests. a similar trend has also been reported in the literature for similar CNT forests [65]. The reason for the loss of adhesion between some CNTs and the substrate during growth, causing the aerial density decay, is yet to be investigated. The lower aerial density at the bottom part is likely the reason for formation of the first buckles close to the substrate in the 70 and 180 μm tall CNT forests. Low density has also been suggested as the dominant factor in previous studies of the formation of buckles close to the substrate [17, 19, 22]. Interestingly, the buckles formed approximately 100 μm above the substrate in the 290 μm tall CNT forest. The SEM images depicted in Fig. 3.15 show a visually discernible unique morphology close to the substrate of the 290 μm CNT forest. High tortuosity of the CNTs close to the substrate is the morphological characteristic of a catalytic CVD grown CNT forest that is self-terminated or approaching the self-termination point[65, 67]. The lower average growth rate of this forest compared to the shorter forests is also an indication of approaching self-termination[67]. We hypothesize that the reason for the formation of the first buckle ~ 100 μm above the substrate is the existence of this tangled layer. The tortuosity of the CNTs decreases by distance from the substrate. The CNTs about 100 μm above the substrate are less tortuous and appear to be more similar in directionality to those observed in the locations of first buckles in the 70 and 180 μm tall CNT forests.

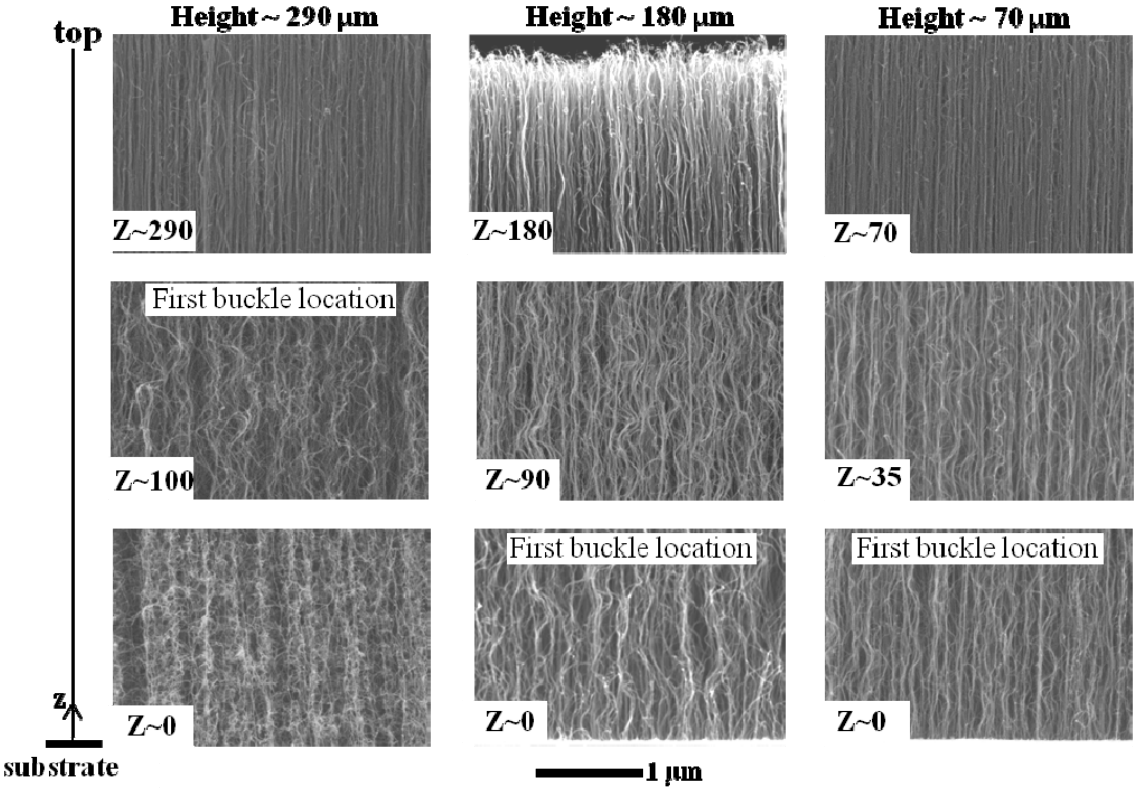

Fig. 3.15. SEM images at 80 kX magnification showing orientation and entanglement of CNTs along the height of LPCVD CNT forests with three different heights - left: 290 µm, middle: 180 µm, and right: 70 µm. The scale bar is 1 µm for each image. The distance from the substrate (Z) is labeled in each image. The locations of the first buckle are also marked.

Three locations along the cross-sectional height of CNT forests grown with APCVD and P-LPCVD recipes – close to the top, middle, and bottom – were imaged using an SEM. In Fig. 3.16, these SEM images are compared with those taken from a 70 µm tall LPCVD forest. The height of the APCVD CNT forest (110 µm) lies between the heights of the two shorter tested LPCVD CNT forests (70, 180 µm). However, the first buckle did not initiate from the bottom as it did for the two LPCVD CNT forests. It formed slightly above the middle of the height – approximately 40-50 µm from the top surface. The location of the first buckle, as shown in Fig. 3.16, appears to have an average orientation similar to that of the location at the middle and bottom of the 70 μm tall LPCVD forest. In the APCVD forest, the CNTs tortuosity increases from the location of the first buckle to the bottom of the forest (Fig. 3.7 and Fig. 3.16). The high degree of tortuosity of the CNTs at the bottom half of the height is the possible reason for the first buckle to not form at the bottom of the CNT forest despite the likely lower CNT number density in that location. The increase in tortuosity is likely due to approaching self-termination in the growth of the APCVD forest [65, 67].

The bending of tips, formation of a local buckle near the top of the forest, and formation of a large buckle under the top buckle in the P-LPCVD forest did not occur in the LPCVD and APCVD CNT forests. We attribute the bending of tips and the formation of a local buckle near the top of this CNT forest to the much higher degree of alignment of CNT tips compared to that of the middle and bottom sections of this CNT forest. A high degree of uniform tortuosity of the CNTs in the middle and bottom sections of P-LPCVD forest was not observed in the other two CNT forest types (Fig. 3.7) and appears to be the likely cause of the formation of the large buckle that follows under the top buckle. This did not occur in the other two CNT forest types presumably because of the larger gradients along their heights. The unique microstructure of the P-LPCVD forest is probably due to the effect of plasma in removing some catalyst particles and creating a CNT forest that appears to have a smaller aerial density than a LPCVD CNT forest. P-LPCVD CNTs were shorter than the other two types (LPCVD and APCVD) due to an early self-termination. High tortuosity of CNTs might be the cause of early self-termination[67]. The deformation mechanism appears to be dependent upon the unique microstructure of CNTs rather than the shorter height. CNT forests with similar morphology (aligned CNTs on top of highly tortuous CNTs) and different heights are expected to deform in a similar manner.

The above observations suggest that highly tortuous CNTs in any location along the height of any of the CNT forests (*e.g.* at the bottom of the APCVD and 290 μm tall LPCVD CNT forests, and at the middle and bottom of the P-LPCVD forest) were not prone to buckling. This is possibly due to the extra constraints that result from the greater number of contacts between the adjacent CNTs. Less interactions between the CNTs in the less tortuous sections caused the CNTs to be more prone to bending and buckling. The CNT forests without highly tortuous CNTs (*e.g.* 70 and 180 μm tall LPCVD CNT forests), however, buckled at the bottom sections which are the locations of lowest CNT aerial density. Thus, we conclude that aerial density and tortuosity are two factors dictating the location of the initial instability in the CNT forests. The first buckle forms close to the base of the CNTs, which is the location of the lowest aerial density, unless the CNTs are highly tortuous.

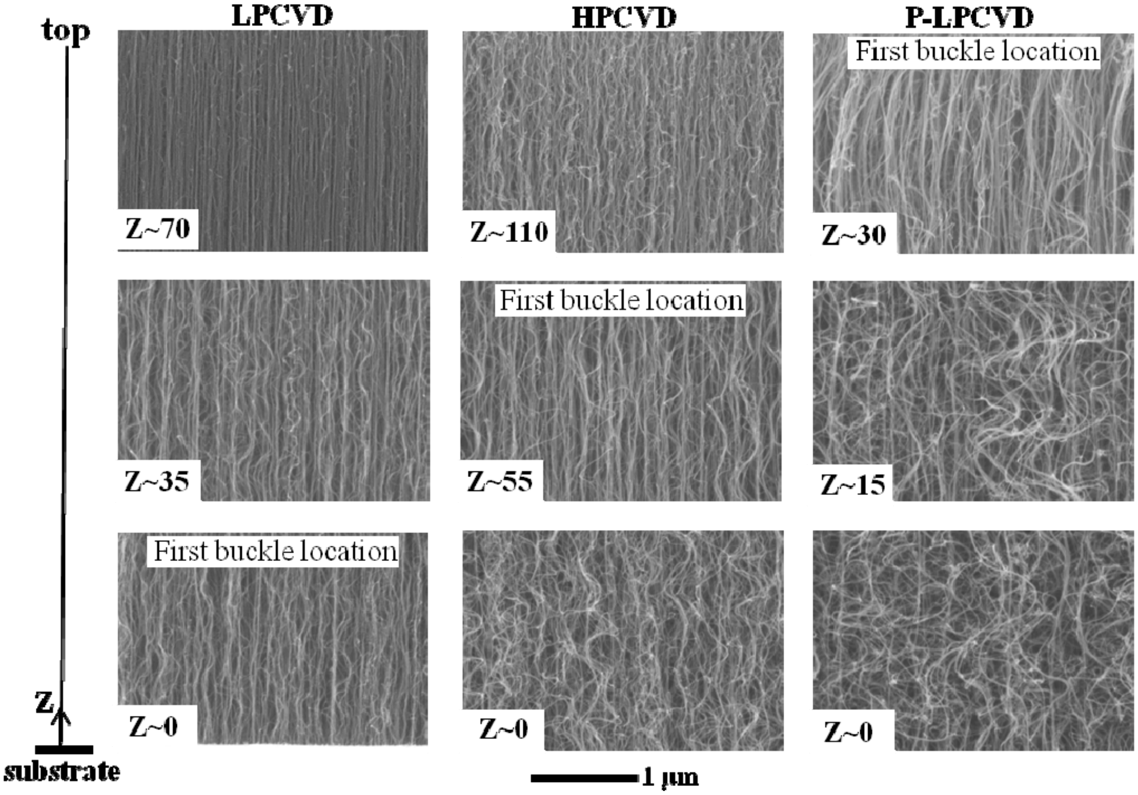

Fig. 3.16. SEM images at 80 kX magnification showing orientation and entanglement of CNTs along the height of LPCVD, APCVD, and P-LPCVD CNT forests. The distance from the substrate (Z) is labeled in each image and the images from the locations of the first buckle are also marked.

Table 3.2. Unloading stiffness, effective elastic modulus, elastic recovery ratio, largest buckle width ratio, and maximum value of negative stress during unloading for different CNT forests.

Recipe	LPCVD-shortest	LPCVD-tallest	APCVD	P-LPCVD
Average height (μm)	70	285	110	30
unloading stiffness (N/m)	6240	1680	4560	19200
Effective elastic modulus (MPa)	91	99.75	104.5	120
Elastic recovery ratio (%)	13	55	46	45
Largest buckle width ratio	2.0	2.8	1.1	1.0
Maximum negative stress (kPa)	53	22	166	82

In addition to the differences in the mechanism of deformation of CNT forests, there are differences in other mechanical parameters for each forest type as summarized in Table 3.2. Stiffness is one of the parameters. Table 3.2 shows that the stiffness of CNT forests is influenced primarily by the height of the forests. With the maximum displacement fixed at 20-30 μm for all compression tests, the shorter CNT forests were deformed to higher strains, and hence – closer to the incompressible height of the forest[27], which gave the forest a stiffer overall response. The unloading portions of load-displacement curves correspond to the elastic recovery. Therefore, the slopes of the initial portions of unloading of the in-bulk locations were used to calculate the unloading stiffnesses and the effective elastic moduli of the different CNT forest types, as commonly done in nanoindentation studies[75, 83]. We find that the elastic modulus of 90-120 MPa is virtually independent of forest height, consistent with previous observations[33]. Calculation of modulus using stiffness and indenter area with the assumption of indentation of an elastic half-space (as is commonly done in nanoindentation experiments on monolithic materials) is not suitable for this type of indentation that involves separation of a block of CNTs from the rest of the forest. The importance of studying the deformation mechanisms of forests and not relying strictly on their elastic modulus for use in mechanical applications is emphasized by the fact that elastic modulus is practically constant, and independent of morphology and height for the three different types of CNT forests studied here.

Other significant differences among the samples tested here were the amount of elastic recovery of the deformation, magnitude of the "negative stress" during the unloading steps, and the extent to which CNTs not directly under the indenter deformed. These characteristics are quantified in Table 3.2. Elastic recovery ratio was calculated by dividing the magnitude of recovered displacement by the maximum displacement using data from test on the sample edge. The magnitude of recovered displacement was measured using recorded videos of indentation of CNT forests by subtracting the permanent displacement of the CNT forest sample from the maximum indentation depth. The elastic recovery was lowest (13%) for the shortest LPCVD forest and highest (55%) for the tallest LPCVD forest. If the formed buckles remained permanent, the lowest recovery for the shortest LPCVD may be explained by the presence of the largest number of buckles in the deformed regions. This is consistent with only a few buckles having been formed in the tallest LPCVD forest and both the APCVD and P-LPCVD forests, all of which have similar recovery ratios (45-55%). The ratio of the width of the largest buckle, measured for the on-edge indentation points, to the width of the indenter shows the extent of deformation to CNTs not directly under the indenter. This parameter was close to 1 for P-LPCVD and APCVD forests, which means only an area equal to the area of the indenter was deformed. The buckle width to indenter width ratio was the highest for the LPCVD forests. This difference may be because of the location of first buckles farther from the indenter for LPCVD forest and also because of the relatively high CNT entanglement at the top surface of the LPCVD forest compared to the other two types. The apparent negative stress arising from negative measured loads during the final stages of unloading is likely a result of adhesion between the diamond indenter tip and the tops of the CNT forest, as commonly observed previously[11, 15, 84]. The maximum negative stress was measured for in-bulk points and is much higher for APCVD forest than the other two types. Additional investigations are warranted to clearly explain the effects of CNT forest morphology (global and local) on the elastic recovery ratio, negative stress, and extent of deformation of CNTs not under the indenter.

3.4 Summary

We synthesized CNT forests with three different heights and also three types of CNT forests to elicit samples with distinct morphologies, all of which were subjected to identical in situ flat punch nanoindentation tests. We find that CNT aerial density and tortuosity represent two key factors governing the overall mechanical response of the CNT forests to local compressive loading. We find that all CNT forests undergo an initial instability manifested as the formation of a buckle. These local buckles that determine a major part of the deformation mechanism of CNT forests form at the location of best combination of low density and less tortuous CNTs along the height. We show that the location of initial buckling moves up from the bottom of the forest if the CNTs near the substrate are highly tortuous. The LPCVD forests begin to buckle at the lower half of the forest while the first buckle in the APCVD is formed close to the middle. P-LPCVD forests buckled in yet another way, with the formation of a smaller buckle at the top and a larger one beneath it. We believe that this study provides insights into establishing a link between the differences in the density and tortuosity along CNT forest height and the distinct deformation mechanisms, which suggest that new synthesis methods could be developed to control CNT forest morphology and tailor the mechanical response to suit the needs of specific applications.

CHAPTER 4 BUCKLING-DRIVEN DELAMINATION OF CARBON NANOTUBE FORESTS

The in situ testing was performed in Dr. Greer's lab at California Institute of Technology. The author thanks Dr. Julia R. Greer and Dr. Shelby B. Hutchens for their help. This chapter is partly reproduced from Pour Shahid Saeed Abadi et al., Applied physics letters, in press (2013).

4.1 Introduction

The deformation of CNT forests under compressive loading was found to be dominated by periodic buckling of the compressed CNT forest pillars[12, 19, 30, 85, 86], and by the combination of buckling and shear offsets in flat punch indentations of CNT forest films (chapter 3 and refs [13, 17, 20-22, 87]) While the visualization of micro-scale compression of CNT forests adds useful insight into the mechanics of these structures, such visualization is not able to capture all deformation and failure modes that occur in compression of larger scale CNT forests.

This chapter reports delamination of CNT forest films revealed by macro-compression of CNT forests. Post-compression scanning electron microscope (SEM) images of 1 cm x 1 cm CNT forests reveal local delamination of the CNT forest films at the nominal pressures as low as 50 kPa. Buckling-driven delamination has been observed in monolithic thin films where the compressive residual stress in the film led to local buckling of the film, which drove propagation of the delamination at the interface[88, 89].This type of delamination occurs in thin films with an existing flaw (debonded region) which buckles under compressive loading and the buckle drives the crack and delamination propagation. A picture of buckling driven delamination in a mica thin film on an aluminum substrate [88] is shown in Fig. 4.1. Buckling in the case of monolithic films is the “thin plate” type of buckling, in the direction perpendicular to the film surface. Delamination of CNT forests is shown here to be column buckling of high aspect ratio CNTs in the direction perpendicular to the CNTs (*i.e.,* parallel to the film surface). Therefore, the phenomenon is different than buckling of monolithic films and cannot be explained without consideration of nanoscale features. We show that delamination is facilitated by the bending moments on the CNT-substrate interface, formed as a result of buckling and stress concentrations associated with the nonuniformity of CNT heights. Furthermore, we demonstrate a method for tailoring the degree of interaction between CNTs to cause delamination in micro-scale indentation of CNT forests. Coating CNT tips with a thin layer of aluminum caused delamination in the on-edge indentations that did not occur in the original structure. This emphasizes the significant effect that mechanical constraints from CNT interactions can have on the delamination occurrence and informs the design of structures to take advantage of this phenomenon.

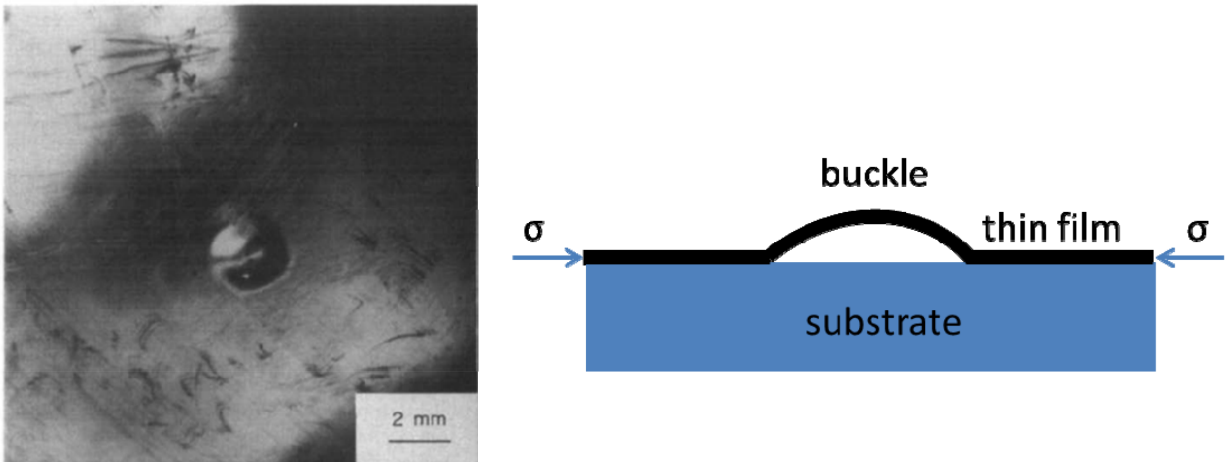

Fig. 4.1. Buckling driven delamination in a mica thin film on an aluminum substrate [88] (left), and a schematic showing the side view and the stress that cause buckling (right).

4.2 Methods

4.2.1 CNT growth and metal coating

CNT forests were grown on 1 cm X 1 cm Si substrates coated with Ti (30 nm)/Al (10 nm)/Fe (3 nm) by electron beam evaporation (e-beam). Low pressure CVD (LPCVD) was used for synthesis of CNT forests in a commercial CVD system (Black Magic Pro 4”, Aixtron SE). The growth temperature was ~750 °C and acetylene was used as the carbon source gas. The chamber pressure was approximately 10 mbar using a C_2H_2/H_2 mixture. A growth time of 5 minutes was used and the CNT forest height ranged from 130-190 μm. The recipe produced multiwall CNTs with diameter ranges determined by transmission electron microscope (TEM) to be 7.2 ± 1.4 nm. The average number of walls was measured to be 6. TEM images are provided in previous work[87]. Aluminum was deposited on top of some of the CNT forests by e-beam evaporation. A deposition rate of 1 angstrom/sec was used.

4.2.2 Nanoindentation

Nanoindentation testing was performed in a custom-built in situ nanomechanical testing instrument, SEMentor, comprised of a nanoindentation arm (Nanomechanics Inc.) inside a field emission scanning electron microscope (SEM) (FEI Quanta200 FEG). A rectangular cross section (60 µm × 80 µm) diamond flat punch indenter tip was used. Nanoindentation experiments were performed by loading to a maximum displacement of 20-30 µm followed by complete unloading. A displacement rate of 50 nm/s was used for loading and unloading of the CNTs. The average loading modulus for each stage of loading was measured by dividing the increase in stress by the increase in strain. Additional details on the SEMentor and testing methodology are presented in chapter 3.

4.2.3 Macroscale compression testing

Macroscale compression and tension tests were performed on CNT forests grown on 1 cm x 1 cm substrates. Compression testing was performed by placing weights on top of the CNT forest while weights were centered as much as possible to create the most possible uniform loading. The compressed samples were then imaged in SEM to observe the deformations.

4.2.4 Macroscale tension testing

For tension testing, the growth substrate and CNT forest top surface were bonded to loading grips using superglue and carbon tape respectively. Then, tension loads with the rate of 100 µm/s were applied in a DTS compression/tension loading unit up to the point of delamination of CNTs from substrate. To prevent failure due to bending moments, a soft string was used to connect the top grip and the instrument. The load at which delamination occurred (the maximum load in the load-displacement curve) was divided to the sample area to calculate the tensile strength. The set-up is shown in Fig. 4.2.

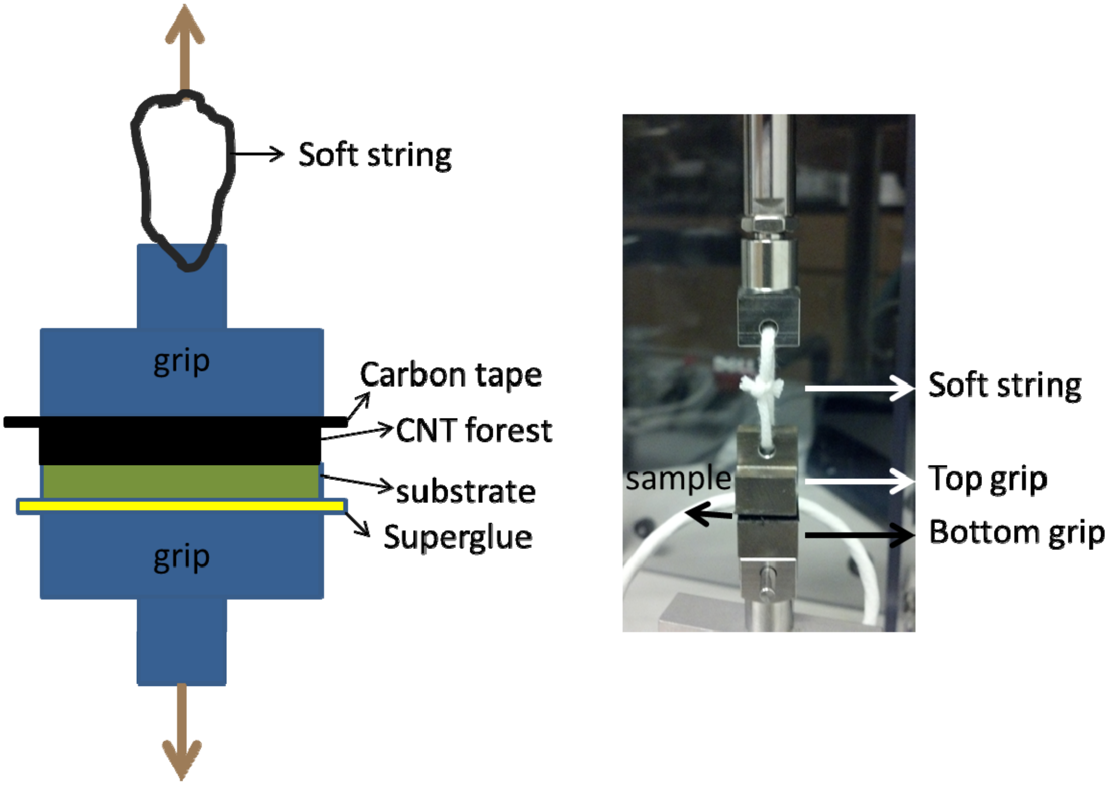

Fig. 4.2. Tensile testing set-up. Left: schematic showing the grips and details of the sample bonded to the grips and the soft string to eliminate the bending moments, and right: real tensile testing set-up.

4.3 Results and discussion

Macro-compression testing was performed on CNT forests grown on 1 cm x 1 cm Si substrates. Nominal pressures of 50 and 100 kPa were applied to the CNT forests by placing 0.5 and 1 kg weights on the samples. SEM images taken from deformed CNT forests are shown in Fig. 4.3. Periodic buckles formed close to the substrate (Fig. 4.3a), as was the case in the indentation of CNT forests grown with the same recipe[87]. Local buckling within CNT forests and the location in which the buckle forms have been shown to result from the density, tortuosity, and entanglement of the CNTs which vary along the height of CNT forests[17, 19, 87]. The buckle formation was not uniform in any of the compressed macroscale CNT forests. The number of buckles along any given edge region ranged from zero to ~ 20. This is likely due to the inherent nonuniformity of the sample height - ~ 10-50% height difference in each sample - which causes a nonuniform distribution of the compressive stress within the sample. Height variance is a common issue in macroscale CNT forests grown by chemical vapor deposition (CVD)[22, 90], likely caused by the flow and temperature variations in the growth chamber. Local delamination of the CNT forest films from the growth substrates was observed in the macroscale compression tests (Fig. 4.3b,c). Delamination occurred in all tested CNT forests within a span of 1 mm along the edge under 50 kPa of nominal pressure. The rest of the edge – a span of 9 mm – remained bonded. The length of the delaminated region increased to greater than 2 mm when the nominal pressure was doubled. Delamination was not observed in microscale flat punch indentation testing of CNT forests grown with the same recipe and loaded to indentation stresses that were higher than the nominal stress applied in macroscale compression[87].

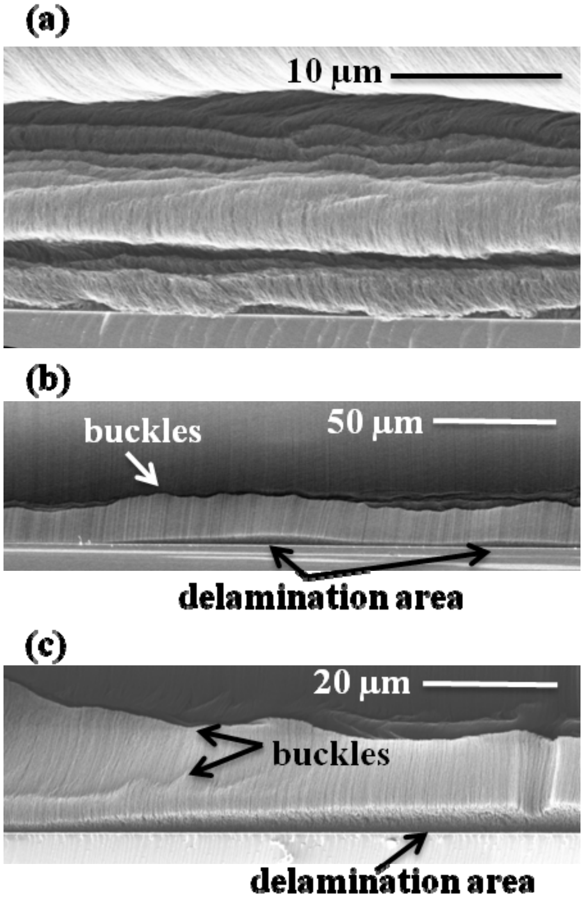

Fig. 4.3. SEM images of the bottom edges of CNT forests illustrating permanent deformation in the CNT forests after macro-compression. a) SEM image of an edge region with multiple buckles but no delamination, b) SEM image of a location illustrating multiple buckles and delamination of CNTs c) a magnified view of a region where CNTs buckled and interface delamination occurred.

Delamination similar to the case of macroscale compression of CNT forests occurred in micro-indentation of CNT forests coated with a 1 μm thick Al layer on the top surface using E-beam evaporation. Indentation on the edge of the 140 μm tall CNT forest to the depth of 20 μm was performed with *in situ* visualization using SEMentor[19, 87], a combination SEM/nanoindenter, allowing visualization of the deformation of the structure during indentation.

The deformation mechanism of the CNT forest coated with a 1 μm thick Al film is illustrated in Fig. 4.4. Images were taken from the recorded video in SEMentor. Fig. 4.4a shows the edge of the coated CNT forest in contact with the indenter before applying pressure. At very small strains, a buckle initiated 35 μm above the substrate representing 25% of the total height (Fig. 4.4b). The buckle propagation was the apparent dominant deformation mode up to a strain of 5.5% where delamination of the CNTs from the substrate initiated at the center and vertical cracks appeared under the indenter edges (Fig. 4.4c). Fig. 4.4d illustrates the maximum displacement of the indenter. At this point, the detached region expanded laterally by 230 μm, and the crack opening between the delaminated CNT forest base and the substrate reached a maximum of 17 μm. Shear offsets also propagated and spanned over 70% of the height. The vertical crack propagation did not break the top coating. Therefore, the CNT tips remained adherent to the coating throughout the test. Approximately 30% of the total deformation was recovered upon unloading. The residual crack opening displacement of the delamination was about 50% of the maximum crack opening displacement along the CNT-substrate interface on the edge (Fig. 4.4d,e).

The indentation stress-strain data are shown in Fig. 4.5. The axial indentation strain was calculated by dividing the measured vertical displacement by the initial height of the CNT forest. To calculate the axial indentation stress, the nanoindenter force is divided by the homogenized contact area underneath the indenter. This area is equivalent to the nanoindenter footprint and remains constant during the test. Data points corresponding to the images in Figs 2a-e are marked on the indentation stress-strain data in Fig. 4.5. Two deformation regimes are apparent: (1) before buckling, characterized by the loading modulus of 75 MPa, and (2) after buckling, where the loading modulus was measured to be 4-6 MPa. Transition between the two regimes occurred gradually, over the strain range of 1-2%. Indentation stress drop from 885 to 870 kPa occurred at point (c), likely due to the initiation of the delamination and the offset vertical cracks, which occurred faster than the prescribed strain rate. At this point, the load dropped to maintain the constant prescribed displacement rate. The loading modulus decreased by 20% from 6 to 4.7 MPa at point (c).

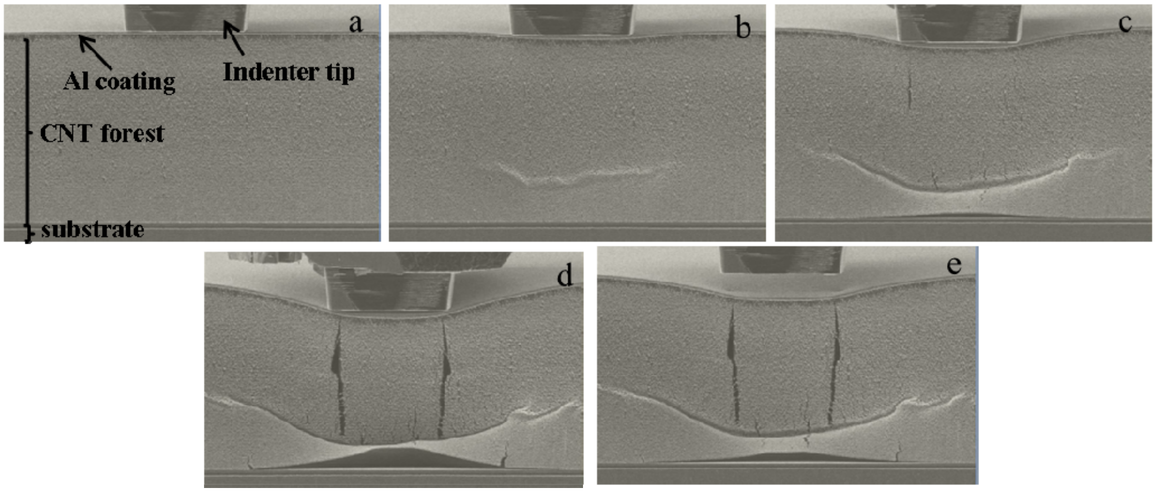

Fig. 4.4. SEM images illustrating the deformation of a CNT forest coated with 1 μm Al that was indented on the edge. Corresponding points on the indentation stress-strain curve are labeled a-e.

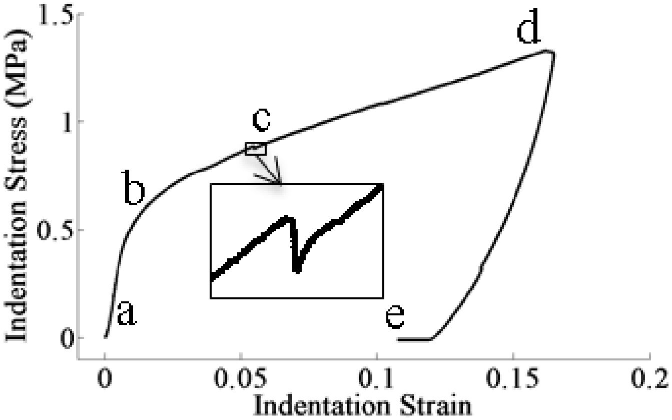

Fig. 4.5. Stress-strain curve of indentation on the edge of a CNT forest coated with 1 μm Al. Points corresponding to those in Fig. 4.4 are labeled a-e.

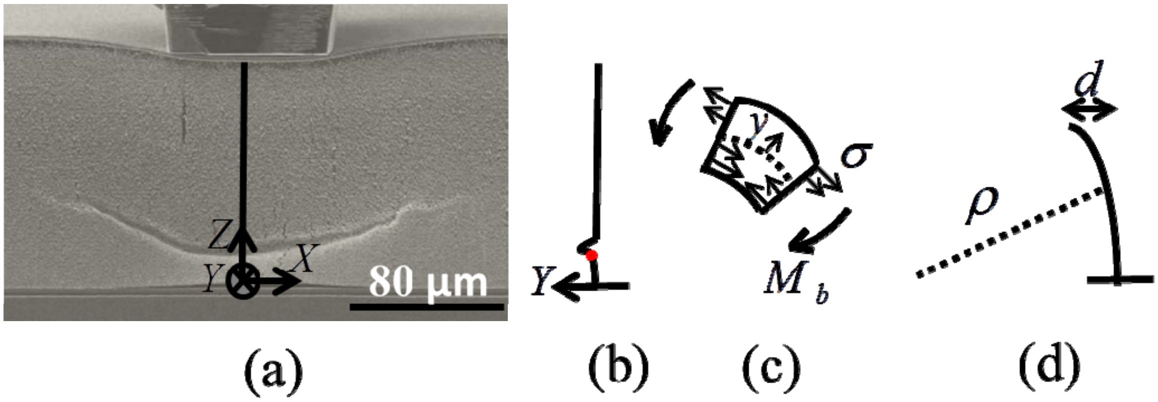

Fig. 4.6. a) The same image as in Fig. 4.4c with a vertical line at the center to guide the eye. The inward arrow shows the direction of the buckling, b) side view of the out-of-plane deformation of the CNT forest along the vertical line in (a). The left arrow shows the direction of the buckling, c) schematic of the bending moment and stress distribution in an element highlighted in (b), d) Curvature of the section of CNT forest under the buckle location.

To gain insight into the stress distribution within the CNT forest that causes its delamination from the substrate, we employed the Euler-Bernoulli beam bending theory and show that it estimates the range of interfacial strength to be on the same order of magnitude as the experimental measurements. Fig. 4.4c, which shows the starting point of the delamination in the indentation of the metal-coated CNT forest, is repeated in Fig. 4.6a. A schematic side view of the CNT deformation along the vertical line in Fig 3a is depicted in Fig 3b, demonstrating the out-of-plane bending of the structure. A differential element of the highlighted section in Fig 3b is shown in Fig. 4.6c showing the associated bending moment and the stress distribution on the element. Bending moment, M_b, and curvature, κ, in an elastic, isotropic, and homogenous beam are related by

$$M_b = E\,I\,\kappa = \frac{E\,I}{\rho} \qquad \text{eq. 4.1}$$

where *E*, *I*, and ρ represent the elastic modulus, second moment of inertia, and radius of curvature respectively. Since the CNTs interact with neighboring CNTs, eq. 4.1- for an isolated beam- is not applicable to the case of an individual CNT. Rather, the group of CNTs under the indenter that buckles together is represented as a single isolated, isotropic, and elastic beam. It should be noted that although the buckling of CNTs is inelastic in this type of forest, the pure bending of CNTs was observed to be mainly elastic as evidenced by the more than 50% decrease the crack opening displacement along the delaminated CNT-substrate interface on the edge upon release of the load (Fig. 4.4d, e). The nonhomogeneity of the CNT forests along the height is taken into account and the collective properties of CNTs close to the substrate are used. The curvature observed in the deformed CNT forest provides evidence of the presence of a moment in the direction schematically depicted in Fig. 4.6c. This bending moment produces normal tensile and compression stresses. As demonstrated in Fig. 4.6c, the bending moment in the depicted direction induces tensile normal stresses on the outer surface of the element, which is the observable edge in the SEM image and videos. The normal stress due to bending can be calculated using

$$\sigma_b = \frac{M_b\, y}{I} \qquad \text{eq. 4.2}$$

where σ and y, depicted in Fig. 4.6c, represent the stress and distance from the neutral axes respectively. We assume the depth of the buckled region into the plane of view in Fig. 4.6a to be 120 µm - twice the depth of the indenter. This assumption originated from the observation of the width that the buckle spans to the left and right outside the extent of the indenter width (the width extended in the left and right directions is approximately equal to the width of the indenter; see Fig. 4.6a). Therefore, y_{max}- half of the depth of the buckled mass - is approximately 60 µm. A first order estimation of the stress at the CNT-substrate interface at the start of delamination is done by combining eq.s 4.1 and 4.2, and results in

$$\sigma_b = \frac{E\, y_{\max}}{\rho} \qquad \text{eq. 4.3}$$

A positive $y_{\max}$ results in a positive σ_b. The positive sign of $y_{\max}$ shows the location of the outer edge and the positive sign of σ_b shows that the stress is tensile (Fig 3c). To estimate ρ, we assumed that the entire part under the buckle formed an arc as shown in Fig. 4.6d. The horizontal displacement of the buckled region as demonstrated in Fig. 4.6d, *d,* is estimated as the vertical displacement of the indenter from the time of buckle initiation to delamination (~10 μm). The deformation of the CNT forest above the buckle area is assumed to be negligible at the time of buckle formation due to no visible deformations at those locations. This assumption makes the displacement of the indenter equal to the maximum out-of-plane displacement of the buckled region of the CNT forest. Using $d = 10\,\mu\text{m}$, ρ is approximately 70 μm. The effective elastic modulus close to the base of CNTs grown with CVD has been measured by a spherical nanoindenter to be in the range of 0.2-1.4 MPa [91]. Therefore, σ_b is estimated to be in the range of 0.2-1.2 MPa at the time and location of the start of delamination. To compare the theoretical estimation with experimental measurements, we performed macroscale tensile testing of the substrate-supported CNT forests. Adhesion strength was measured to be in the range of 0.2-0.4 MPa, which falls into the range of the estimated bending stress that caused delamination at the interface. This agreement shows that, indeed, the tensile stress caused by post-buckling bending of CNTs is the cause of delamination and that use of Euler-Bernoulli beam bending theory for the group of entangled CNTs results in a reasonable estimation of the interfacial strength. This also demonstrates the influential role of entanglement of CNTs in delamination occurrence at the interface.

Based on these observations, a buckling-induced bending moment is expected to also form on the CNT-substrate interface during flat punch indentation into the as-grown CNT forests. However, no delamination was observed for indentations up to the same depth as the coated samples, of 30 μm[87], (Fig. 4.7a). This suggests that the tensile stresses within the CNT forest were lower than the interfacial adhesion strength. This could be attributed to the more relaxed constraints in the deformation of the uncoated CNTs, which enabled additional mechanisms to carry the mechanical strain, like forming severed vertical shear offsets under the indenter edges. This causes CNTs directly under indenter to separate from the rest of the CNT forest as they can more freely slide against the surrounding[87, 92, 93]. In contrast, the coated CNT forests deform via out-of-plane bending of the buckled area, likely because of the mechanical constraint caused by the top coating. Larger out-of-plane displacements typically correspond to the lower radii of curvature, which generate a greater bending moment and tensile stresses acting on the interface. On-edge indentation of similar CNT forests with thinner 100 nm Al coatings resulted in fracture of the coating and deformed similarly to that observed in the case of uncoated CNT forests, i.e. no delamination (Fig. 4.7b). The three characteristic deformation morphologies, corresponding to the no coating, 100 nm-thick and 1 µm-thick Al coating are illustrated side by side in Fig. 4.7a-c.

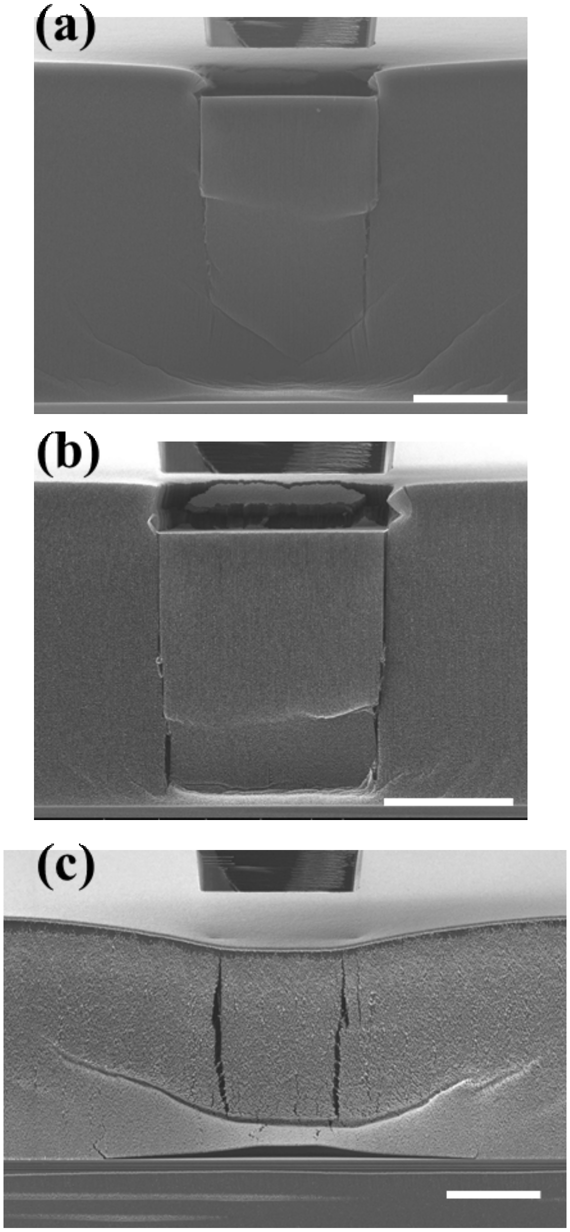

Fig. 4.7. Permanent deformation morphologies that resulted from flat punch indentation on the edge of a) an uncoated CNT forest, and CNT forests coated with b) 100 nm and c) 1 μm Al coatings. The scale bars are 50 μm.

Increased mechanical constraints that arise from the top metal coating layer in the case of coated CNT forests did not exist in the case of delamination of uncoated CNT forests during macroscale compression tests. However, the global compression load created larger buckles (Fig. 4.3) than the case of local micro-indentation of same CNT forest (Fig. 4.7a). The height nonuniformity was responsible for non-uniform buckling (Fig. 4.3b,c) that likely led to stress concentrations causing delamination. SEM images in Fig. 4.8 further clarify this effect. It is noted that nonuniformity in the height has a minimal effect on the micro-scale tests since CNTs are more uniform at the length scale of the nanoindenter contact surface.

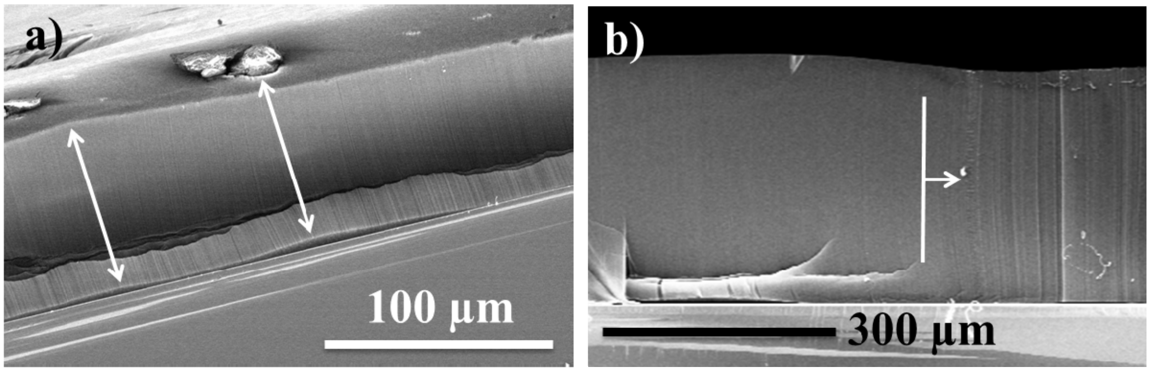

Fig. 4.8. Deformed CNT forests showing the effects of uncoated CNT forest height nonuniformities on the buckling-induced delamination. a) Two locations of local delamination –showed by arrows - directly under two hills. b) a taller – 300 µm - CNT forest buckled and delaminated similar to the case of 100 µm tall CNT forest. The right side showed by arrow is a region with lower height in which no buckling and delamination occurred.

4.4 Summary

We reported delamination driven by buckling in compression of CNT forest films on Si substrates. In macroscale compression of CVD grown CNT forests, delamination initiated under nominal pressures as low as 50 kPa. The observed delamination was attributed to local tensile loading of CNT-substrate interface due to post-buckling bending of CNTs. The stresses exceeding the strength of the interface arise from the interaction between adjacent CNTs and the inherent nonuniformity of forest height. Delamination occurred during micro-scale indentation of a film-coated CNT forest and no delamination occurred in a similar, uncoated CNT forest. This result demonstrates that mechanical constraints are critical factors that can cause loads on the buckled region that are in excess of the strength of adhesion between CNTs and their substrate. Euler-Bernoulli beam bending theory was employed for the population of CNTs that buckle together to estimate the tensile stress leading to delamination. The magnitude of the tensile stress was on the same order of magnitude as the measured interfacial tensile strength. Delamination may reduce the functional properties of the CNT forest. For example, thermal or electrical conduction paths through the CNTs can be severed by delamination, which would cause decay in the functionality of the CNT forest film as an interface material. We postulate that buckling-driven delamination was the main reason for an observed increase in the thermal resistance of a CNT forests grown on the Si side of a SiC substrate with loading[94]. While our results provide a warning to be heeded in the design of CNT-based interface materials, we believe that the delamination mechanism of entangled, high aspect ratio nanomaterials revealed here could also be used in the design of new micro-electromechanical systems. For instance, decreased electrical conductance in CNT forests coated with metal films could potentially be utilized to design nano-based mechanical pressure and impact sensors that work based on interface delamination.

CHAPTER 5 DEFORMATION AND FAILURE MECHANISM OF CONFORMALLY-COATED CARBON NANOTUBE FORESTS

5.1 Introduction

While the mechanical behavior of CNT forests could be tailored using growth techniques (chapter 3), the addition of thin film coatings could also be utilized for this purpose. By coating a CNT forest, a hybrid nanostructure is created that is expected to have a different mechanical behavior due to the change of properties of individual CNTs as well as the change in interaction and constraints within the CNT forest. Moreover, processes to apply coatings are more controllable than the typical morphology variations observed through CNT synthesis techniques. Depending on the coating material and method, coated CNTs have many potential applications such as optical, electronic, catalytic, sensing, and magnetic materials as well as reinforcement in composite materials and have attracted the attention of many researchers [24, 29, 37-50, 95]. Different coating methods such as physical vapor deposition [45, 46], chemical vapor deposition [40, 42], electroless plating [37, 38], and atomic layer deposition (ALD) [39, 48-50] have been employed to coat the CNTs. Despite the recent attention of researchers to visualization and characterization of the mechanical behavior of pristine CNT forests, the deformation and failure mechanism of coated CNT forests are not well known. Raney et al. [14] coated CNT forests with SnO_2 and MnO_2 nanoparticles and tested the coated CNT forests in compression. They reported increased energy dissipation in the CNT forests owing to the nanoparticle coating. Changes in deformation mechanisms such as bending and buckling behavior still need to be investigated. In situ mechanical testing facilitates the visualization of the deformation and failure. The mechanical behavior of conformally-coated CNT forests (i.e. CNTs coated from top to bottom with a continuous layer of a second material) is expected to be different from the behavior of CNT forests coated with discrete particles. This requires further investigation and is the focus of this chapter. Here, the mechanical behavior of CNT forests coated with different thicknesses of aluminum oxide (alumina) using atomic layer deposition is reported. ALD is a chemical vapor phase deposition technique that is capable of depositing high purity conformal coatings on high aspect ratio structures. It relies on subsequent self-limiting deposition of alternate atomic layers. In this work, we coated high aspect ratio, nominally vertical, and entangled CNTs with ALD Al_2O_3. Alumina was selected because it is a common ALD material that has been shown to behave well as a seed layer for functionalizing the CNTs [40], isolating and insulating CNTs [40], and enhancing the stability and capacity of CNTs as an anode in Li-ion batteries [42]. In situ flat punch indentation of the hybrid structures was performed to observe the mechanical behavior. Furthermore, ex situ flat punch and Berkovich indentation testing was performed to quantify the stiffness and recoverability of the hybrid structures. We report multiple local buckling at the bottom of CNT forests with a 2 nm coating, similar to the deformation of uncoated CNT forests. CNT forests coated with 10 nm of alumina, however, failed by fracture of alumina/CNT nanotubes. Increases in the stiffness of CNT forests were measured using ex situ flat punch and Berkovich indentation of CNT forests. The amount of increase fell into the range as predicted by the theories of bending and axial compression of individual CNTs.

In addition, deformation to small strains resulted in higher recoverability. The observed fracture should be taken into account for determination of the load limit on coated CNT forests. The new results could also be a baseline for designing new structures for applications that require higher stiffness or recoverability.

5.2 Methods

An Aixtron Black Magic CVD system was used to grow CNTs on Si substrates coatd with Ti (30 nm)/ Al (10 nm)/ Fe (3nm) as a catalyst sack. LPCVD recipes for 2 and 3.5 min growth were used and led to 10 and 40 μm tall CNT forests. Additional details are described in chapter 3.s

ALD coatings were carried out in a Cambridge NanoTech ALD system at 250^{o}C. Trimethylaluminum (TMA) and water were used as sources of aluminum and oxygen respectively. Every alumina deposition cycle included TMA dosing, Ar purging, water dosing, and Ar purging. Alumina coatings with approximate thicknesses of 2, 5, and 10 nm were deposited using 20, 50, and 100 cycles, respectively.

In situ flat punch indentation was performed to observe the deformation mechanism under compression loading. A micro-indenter with a tip cross-section of 40 μm x 40 μm was used to indent the edge of the CNT forests in a scanning electron microscope (Fig. 5.1). A piece-wise displacement scheme was used in which the indenter tip was held at a constant displacement while the SEM rastered a micrograph. Each micrograph acquisition was 60 – 90s in duration. The indenter tip traveled at a displacement rate of 250 nm/s between displacement steps. To visualize the deformation, a micrograph image was collected each 750 nm of indenter displacement. Taking each image took between 60-90s. A schematic of the stage, sample, indenter tip, loading unit, and actuator is depicted in Fig. 5.1a. a photograph image of set-up is showed in Fig. 5.1b.

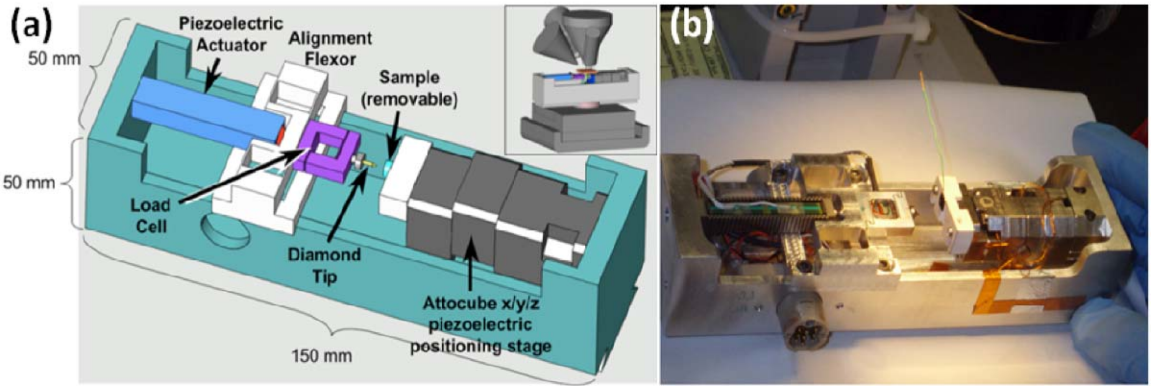

Fig. 5.1. Micro-indentation apparatus used to visualize compression loading of CNT forests (in Air Force research lab). a) a schematic showing the functional components of the sample stage and loading unit – the inset shows the apparatus configured inside the SEM, b) photograph of the apparatus outside of the SEM.

5.3 Results and discussion

In situ flat punch indentation testing was performed on three CNT forests, all with the same height but different alumina coating thicknesses (no coating, 2, and 10 nm). The deformations to similar strains of 30-50% are shown in Fig. 5.2. Both the uncoated CNT forest (Fig. 5.2a) and the one with the 2 nm coating (Fig. 5.2b) exhibited formation of local periodic buckles starting from the bottom of the CNT forest. The deformation was similar to the deformation of the uncoated CNT forests grown with the same recipe (chapters 3, 4). Fig. 5.2c and d show magnified views of the buckles. Multiple buckles close to the substrate can be seen in Fig. 5.2c with the top most buckle being the most visible. Highly deformed coated CNTs are shown in Fig. 5.2d, without any visible fracture. Fig. 5.2e shows the deformation of the CNT forest with the 10 nm coating. Although the indentation depth was similar, different deformation and failure mechanisms were observed, the nanotubes fractured in a brittle manner. The nanotubes that moved towards the viewing pane are magnified in Fig. 5.2f and g. Bare CNTs are observable in the high magnification images. Arrows are used to indicate a few of the bare CNTs in both Fig. 5.2f and g. The fractured ends of the CNTs that are most visible in Fig. 5.2g show that CNTs are also fractured.

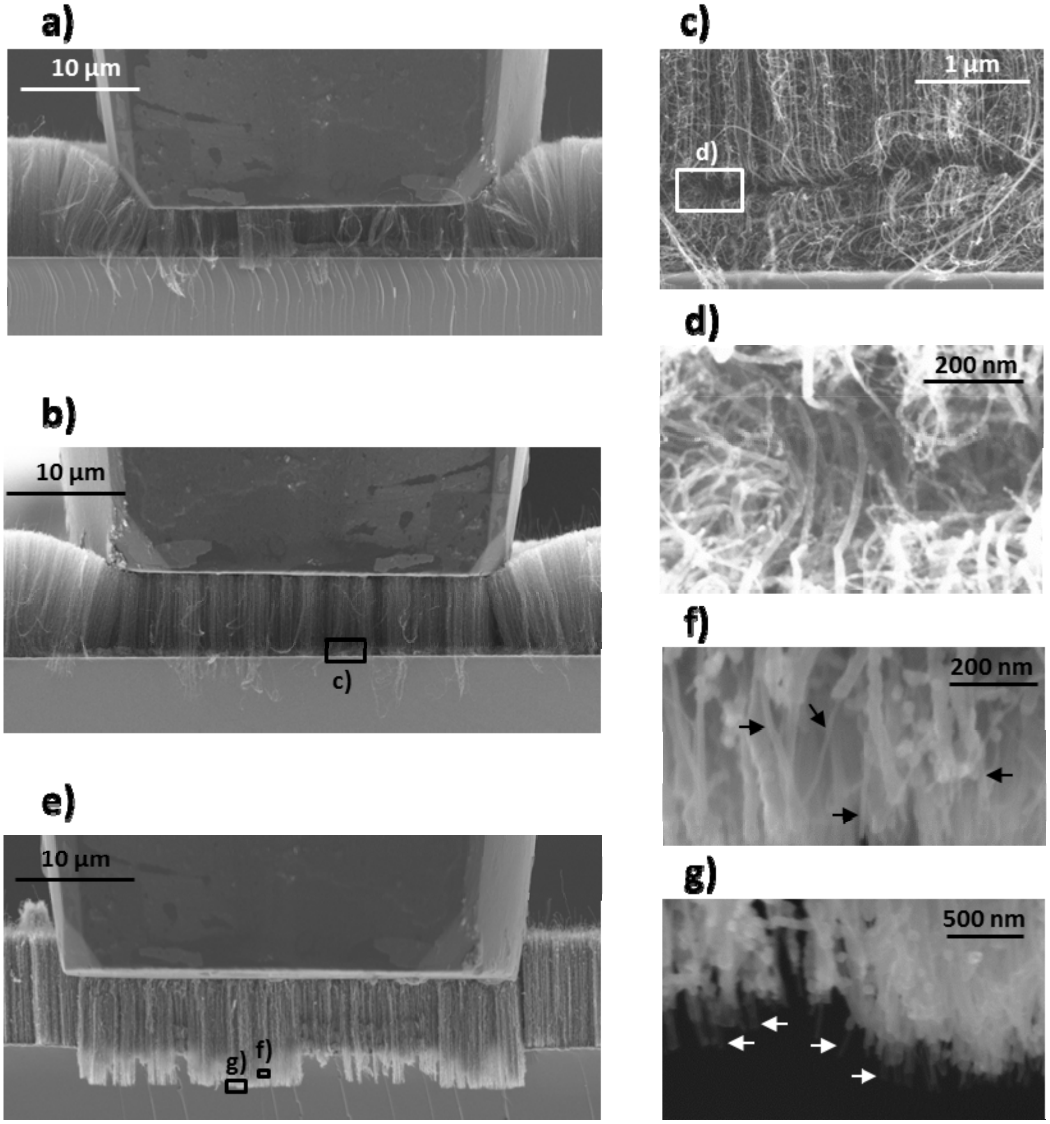

Fig. 5.2. Deformed uncoated and alumina-coated 10 μm tall CNT forests after micro-indentation. a) uncoated CNT forest buckled from bottom, b) CNT forest with 2 nm coating buckled from bottom similar to uncoated CNT forest, c) magnified view of the area inside the rectangle in (b) showing the multiple buckles close to substrate, d) magnified view of the area inside the rectangle in (c) showing curved CNTs in the top most buckle with no fracture, e) CNT forest with 10 nm coating showing nanotube fracture, f), and g) magnified view of the rectangles in (e) showing fractured nanotubes – arrows indicate some of the bare CNTs pulled out of the alumina coating.

To examine the deformation and failure mechanism in taller CNT forests, micro-indentation experiments similar to those performed on 10 μm tall CNT forests were performed on 40 μm tall CNT forests. The length of 40 μm is approaching the maximum length that could be coated almost uniformly from top to bottom with the used ALD recipe. The deformation mechanism for an uncoated CNT forest, and those coated with 2 and 10 nm are shown in Fig. 5.3a, b, and c respectively. Similar to the case of 10 μm tall CNT forests, 40 μm tall CNT forests without coating or with the 2 nm coating were deformed by formation of multiple local buckles close to the substrate (Fig. 5.3a, b) while the CNT forest with the 10 nm coating failed by fracture of the nanotubes (Fig. 5.3c).

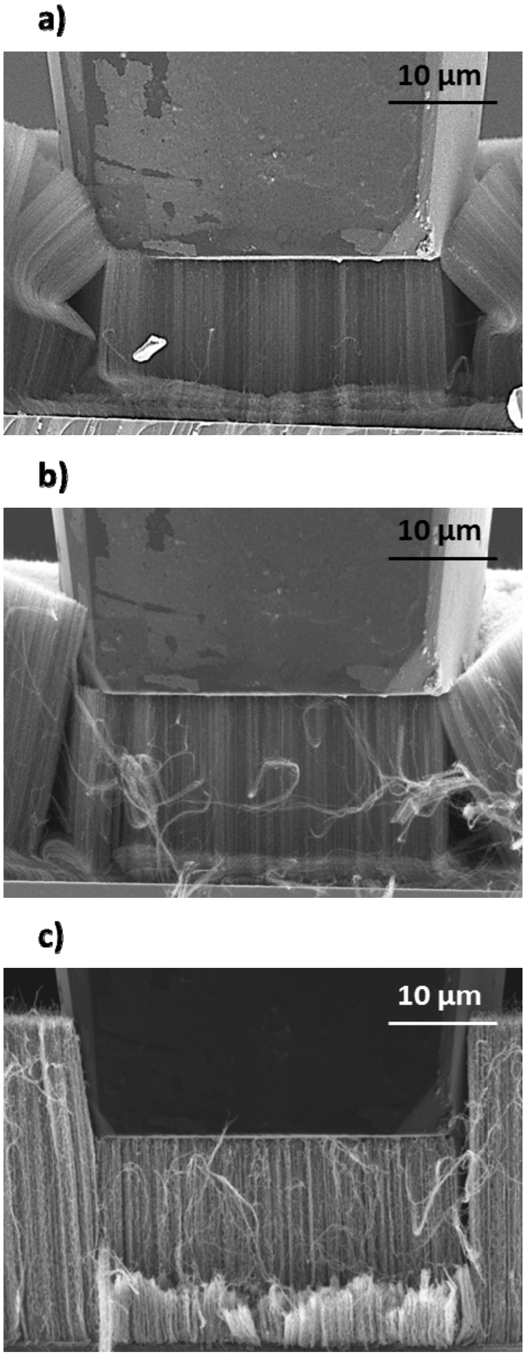

Fig. 5.3. Deformed uncoated and alumina-coated 40 µm tall CNT forests after micro-indentation. a) uncoated CNT forest buckled from bottom, b) CNT forest with a 2 nm coating buckled from bottom similar to uncoated CNT forest, c) CNT forest with a 10 nm coating showing nanotube fracture.

SEM images of step-by-step deformation and fracture of the 40 μm tall CNT forests coated with 10 nm alumina are featured in Fig. 5.4a-e and the corresponding points on the load-displacement curve are marked in in Fig. 5.4f. Point (a) shows the start of indentation of the CNT forest. The first visible deformation occurred at point (b) where a wrinkle was formed. The wrinkle progress led to fracture of the nanotubes, and can be distinguished more clearly in points (c)-(e). The top fractured section moved further away from the viewing pane and the fractured tips of the bottom section moved toward the viewing pane. Formation of the wrinkle was associated with a small drop in load and a sudden displacement at point (b) while the complete fracture of the CNT/alumina nanotubes was associated with a larger drop in load and sudden displacement at point (c). Point (d) shows the indenter at maximum displacement before the start of unloading. Point (e) shows the unloaded sample with almost no recovery, as expected due to fracture.

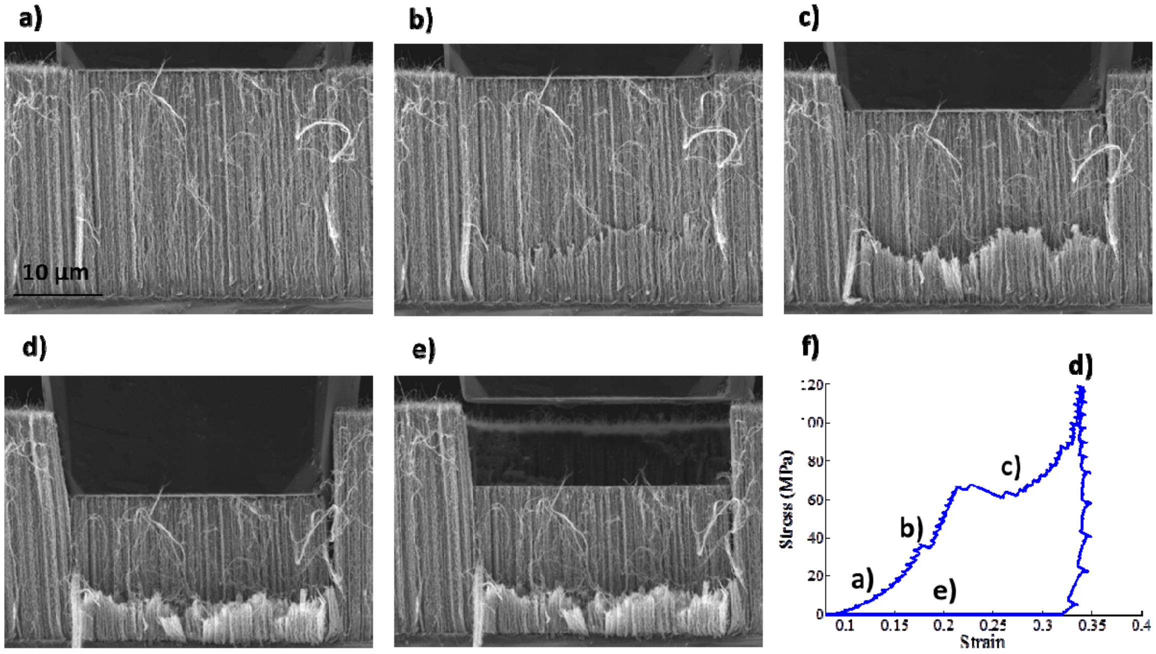

Fig. 5.4. Deformation of a CNT forest coated with 10 nm of alumina. a) initiation of compression loading with no visible deformation, b) after formation of a local buckle, c) progress of the buckle leading to fracture of nanotubes, d) maximum displacement of the indenter – broken nanotube tips are observable on the bottom section, e) unloaded state, and f) stress-strain curve with marked points associated with images a-e.

In the case of 2 nm coating, alumina deposits on the CNTs in the form of nanoparticles as shown in Fig. 5.2d. This causes the deformation mechanism of the CNT forest with 2 nm coating to remain similar to the deformation mechanism in an uncoated CNT forest. In the case of 10 nm coating, however, the coating is continuous and an alumina nanotube forms around each CNT (Fig. 5.2f,g). Unlike the CNTs, alumina nanotubes do not have enough flexibility to fold and buckle without fracturing; hence the observed fracture of CNTs coated with a continuous film of alumina was not unexpected. The consequent fracturing of CNTs, however, requires further clarification. Fracture due to tension loading as illustrated in Fig. 5.5 is a likely scenario for CNT fracture. The CNT bridges the fractured alumina nanotube pieces at first but eventually fractures after some increase in length. Bare CNTs shown in Fig. 5.5d are the experimental evidence of this elongation and bridging. The bridging is believed to be similar to the CNT bridging in CNT-alumina composites. For instance, Fig. 5.6 [96] shows CNTs bridging a crack in a CNT-amorphous alumina powder. This mechanism has been proposed to increase the toughness of the ceramic composites. The fracture in CNT probably initiates from the defects usually existing in CVD grown CNTs [23, 28] or from defects caused by contact with the fractured edge of the alumina nanotube. The highly defective structure of CVD grown CNTs results in a wide range of tensile strength. The tensile strength has been reported to be in the range of approximately 20-200 GPa for individual CVD grown CNTs with a diameter range of 20-25 nm [23, 97] with half of the data being between approximately 50-150 GPA. It is not possible to get a reasonable estimation of the tensile stresses at the fracture locations due to the complexities of the structure. However, tensile stresses close to the range measured for MWCNTs [23, 97] is expected in the bare CNTs which fractured.

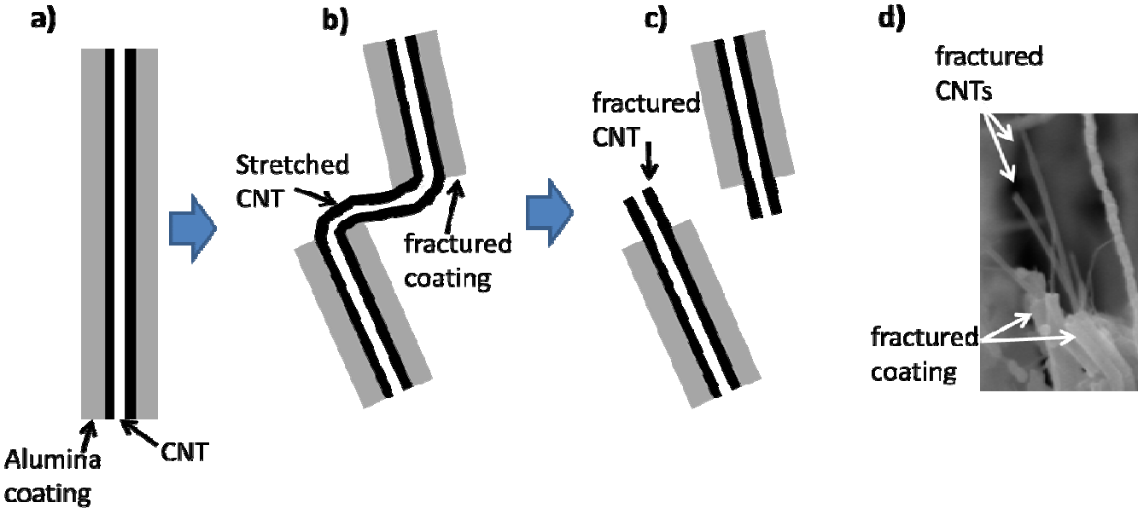

Fig. 5.5. Fracture of a coated CNT. a) a coated CNT before fracture, b) after fracture of the coating, c) after fracture of both coating and CNT, and d) fractured alumina/CNT after indentation of a 40 μm tall CNT forest coated with 10 nm of alumina.

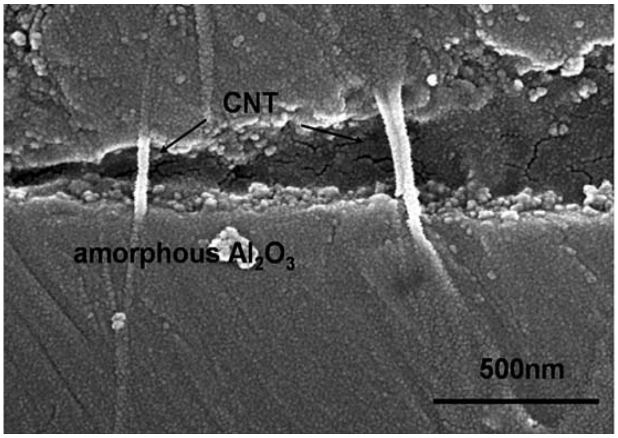

Fig. 5.6. CNTs bridging a crack in an alumina-CNT composite [96].

Ex situ indentation testing was done on the top surface of the CNT forests with no coating and with 5, and 10 nm coating. Two indenter types, a Berkovich tip and a flat punch with a 30 μm diameter circular cross section, were used. A minimum of six measurements to the depth of 2-3 μm with loading rate of 850 μN/s was performed on each sample. The unloading stiffness was measured for indentation by both tips. The results are shown in Fig. 5.7 with a schematic demonstration of tip geometries and CNT deformations using each tip. A Berkovich tip bends the CNTs to the sides but a flat punch compresses the CNTs downward. This was the objective for using two indenters – *i.e.* to investigate the effect of coating on the stiffness in two modes of deformation caused by the two indenters. A significant increase in the stiffness due to coating was measured. The Berkovich tip measured lower stiffness values compared to the flat punch. This is expected because of the smaller contact area between the CNTs and the Berkovich tip. The increase in stiffness with 10 nm coating was measured by the Berkovich tip to be 14-fold and by the flat punch to be 4-fold. The effects of coating on the stiffness of CNTs were compared with theoretical estimations using simple compression and bending theories to facilitate the understanding of the measured differences. Stiffness is proportional to the product of Young's modulus and area, *EA,* with the assumption of deformations being in pure axial compression mode while it is proportional to the product of Young's modulus and bending moment of inertia, *EI,* with the assumption of deformations being in pure bending mode. Young's modulus has been measured to be in the range of 0.8-1.3 TPa for multiwall CNTs [98-100] and 170-180 GPa for ALD alumina .[101] Calculations in this work were performed using 2.9 and 7.2 nm as the inner and outer diameters of CNTs (the average value measured in TEM images), 1TPa as Young's modulus of CNTs, and 180 GPa as the Young's modulus of ALD alumina. The results are listed in Table 5.1 for bare CNT and for CNT coated with 5 and 10 nm alumina. Pure compression theory predicts a 4-fold increase in stiffness with 10 nm alumina coating and pure bending theory predicts a 40-fold increase. Both sets of experimental data (using flat punch and Berkovich tip) fall in range predicted by assumption of pure compression and pure bending. The value measured by flat punch is the same as prediction by pure compression theory. This is likely because the release of the axial loads is dominant in the initial portion of the unloading. The reason for the discrepancy between the value of increase in stiffness measured by the Berkovich tip and the prediction by bending theory is likely due to the fact that Berkovich indenters are not perfectly sharp but have a radius of curvature of hundreds of nanometers. The deformation caused by the initial curved section is more similar to that caused by a flat punch (compression mode) and hence, causes a decrease in the measured change of stiffness.

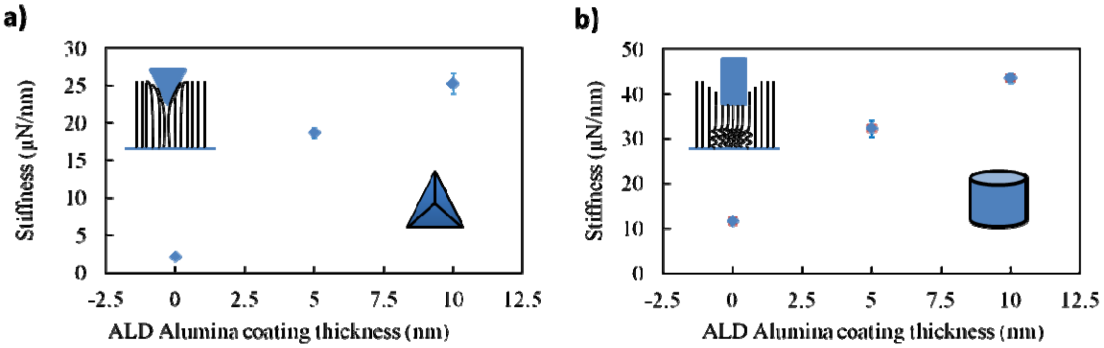

Fig. 5.7. Stiffness data for CNT forests with no coating and 5 and 10 nm coating measured by a) a Berkovich tip, and b) a flat punch. Schematic of The tip shapes and deformation mechanism using the two indenters are shown in the figures.

Table 5.1. Theoretical estimation of EA and EI for bare and coated CNTs.

	EA (μN)	EI (X 10^{-17} μN)
CNT	34	13
CNT coated with 5 nm alumina	67	88
CNT coated with 10 nm alumina	130	490

The locations indented by the Berkovich tip were imaged using scanning probe microscopy (SPM) to measure the size and depth of the permanent imprints. SPM was performed by moving the Berkovich tip across the indented area while controlling the height to maintain a constant force of 2 nN. Size and depth of the imprints were smaller in the coated samples than uncoated samples. This is shown for a CNT forest with 10 nm coating in Fig. 5.8. The maximum depth as shown in the scale bars was decreased by approximately 40% (from 689 to 434 nm) with the 10 nm coating. This is due to higher vdW forces between bare CNTs compared to coated CNTs that keep them together when bent. VdW forces are proportional to Hamaker constant [102] which has been reported to be 15 x 10^{19} for alumina [103] compared to 47 x 10^{19} for graphite [51]. The greater restoring force resulting from the increased bending stiffness of the nanotubes could also have contributed to the increased recoverability. The recoverability was almost negligible in the case of flat punch indentation due to the fracturing of nanotubes. In the case of Berkovich indentation, less fracturing is expected since bending of CNTs are more prevalent.

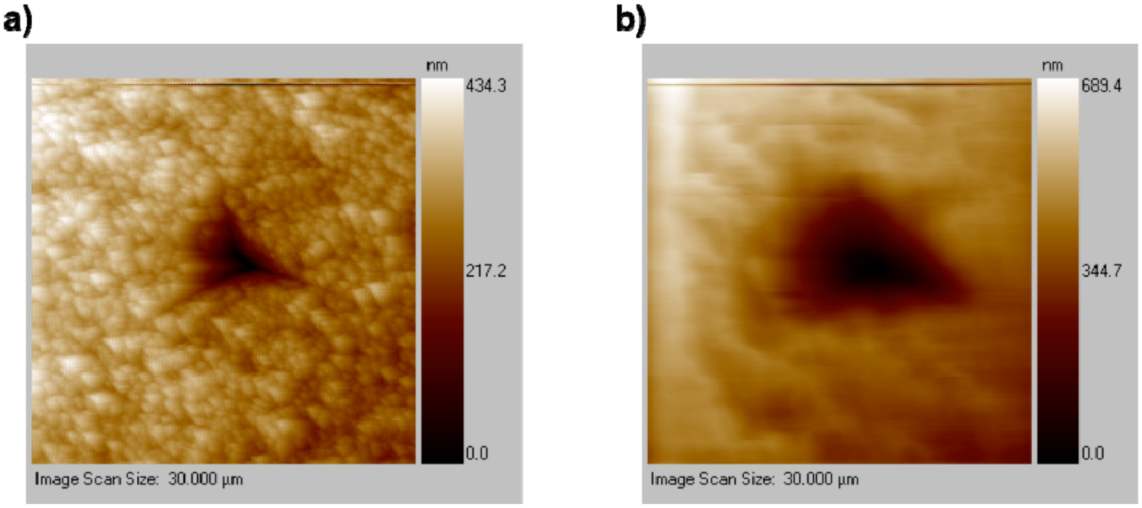

Fig. 5.8. Permanent deformations after indentation by a Berkovich tip and scanned using the same tip. a) the CNT forest with 10 nm coating, and b) the uncoated CNT forest.

5.4 Summary

Results of in situ flat punch indentation and ex situ flat punch and Berkovich indentation of CNT forests with different thicknesses of ALD alumina coating were reported and compared with the values for CNT forests without coating. In situ flat punch indentations showed that while a continuous layer of coating could cause fracture of CNT/alumina hybrid nanostructure, thinner coatings that form particles on the CNTs do not change the deformation mechanism significantly. The fracture of CNTs coated with a continuous film of alumina is likely due to tensile loading of CNTs after fracture of the alumina nanotubes. The ex situ indentations were performed to precisely quantify the effective stiffness of ALD alumina coated CNT forests. The results indicated that the thickest examined coating (10 nm) increases the stiffness measured by a flat punch by 4-fold and the stiffness measured by a Berkovich tip by 14-fold. The difference is related to the fact that the stiffness measured by a flat punch originates dominantly from pure compression while the one measured by the Berkovich tip originates from a combination of bending and compression. Furthermore, recoverability of the deformation after Berkovich indentation was measured by scanning the indented area after indentation of both uncoated sample and the sample with 10 nm alumina coating. An increased recoverability of 40% was measured from uncoated to 10 nm alumina coating. The information on both increased stiffness and recoverability could be useful for designing new hybrid structures. The load at which nanotubes fracture (e.g. 30-40 MPa for the case of 10 nm alumina coating) should be considered as the load limit of the structure.

CHAPTER 6 EFFECT OF SOLVENTS ON MECHANICAL BEHAVIOR OF CARBON NANOTUBE FORESTS

6.1 Introduction

It was shown in the previous chapters that the degree of interaction between CNTs affect their mechanical behavior. Minimum density close to the substrate caused buckling initiation from the bottom of the CNT forest and high tortuosity of CNTs close to the substrate moved the incipient buckling location to the middle and top of the forest (chapter 3). The results suggest that the interaction between individual CNTs, which is through van der Waals forces, affects the collective mechanical response of CNT forests. The extent of this influence needs further investigation and is the focus of this work. This work provides a better fundamental understanding of the complex structure of CNT forests.

VdW forces between any two object could change by changing the medium through which the objects interact [102]. We use this fact to intentionally manipulate the interaction between CNTs in as-grown CNT forests. We soak CNT forests in different solvents. Then, we examine the mechanical behavior of the CNT forests in the presence of solvents. This is performed to clarify the effect of interaction between individual CNTs in the collective mechanical behavior of CNT forests. The effect of capillary forces due to evaporation of fluids such as solvents on densification and self-assembly of CNT forests have been investigated [104-110] and shown to affect the mechanical properties [108, 109]. However, the mechanical properties of the CNT forests in the presence of solvents are still unknown. In addition to the fundamental understanding of the factors affecting the mechanical response of CNT forests, this knowledge is necessary for the analysis of self-assembly due to capillary forces and also for applications where a CNT forest wetted by a solvent is under mechanical loading [52]. In the latter case, CNT forest thermal interface materials were wetted by a solvent in order to facilitate coating of them with polymers to increase the thermal conductance at the CNT contact surface.

In this chapter, we investigate the compressive response and deformation mechanism of the CNT forests in the presence of solvents by flat punch micro-indentation and post-evaporation SEM imaging of macroscale CNT forests which are compressed in the presence of solvents and then dried under compression. We report up to 80% reduction in stiffness. Furthermore, we find that deformation mechanism changes from local buckling close to substrate to local buckles distributed along height in addition to global buckling of CNTs. The effect of solvents on the vdW forces between individual CNTs are quantified. Our results quantify the effect of vdW forces between CNTs in the stiffness of CNT forests. They also show how the change in interaction between CNTs affects the buckling behavior. This demonstrates the importance of interaction between CNTs in the collective mechanical response of CNT forests and will hopefully lead to new applications of CNT forests.

6.2 Methods

MWCNT forests were grown using a low pressure CVD method on Si substrates coated with Ni (100 nm)/Ti (30 nm)/Al (10 nm)/Fe (3 nm) as the catalyst stack. The growth was performed in an Aixtron Black Magic CVD system at a temperature of 750^o C and a pressure of 10 mbar. Two growth times were used: 10 min and 30 min that resulted in height ranges of 25-40 and 115-150 µm respectively. Acetylene and hydrogen were used with the rates of 100 and 700 sccm respectively. The average diameter and the average number of walls were measured using transmission electron microscopy to be 7 nm and 6 respectively. More information on the growth parameters and TEM images are provided in chapter 3.

Mirco-indentation testing was performed using a 100 µm diameter cylindrical flat punch in an Agilant nanoindentation system. Short (25-40 µm) and long (115-150 µm) CNTs were indented to 10 and 20 µm depth respectively. Strain rate of 0.1 s^{-1} was used except in the case that change of strain rate was being investigated when three strain rates (0.01, 0.1, and 1 s^{-1}) were used. First, micro-indentation testing was performed on as-grown samples in air. Then, samples were placed in a pool of solvent and similar indentation testing was performed on the samples soaked in solvent (Fig. 6.1). Experiments on each sample were performed in a relatively short time before a significant amount of evaporation of the solvent and decrease in the solvent level.

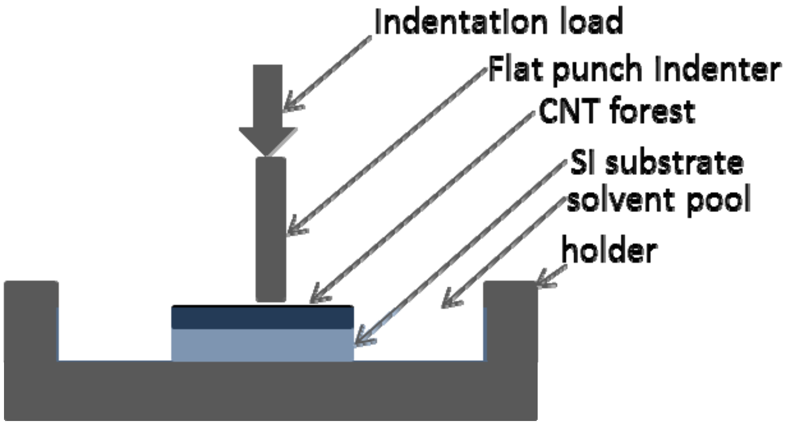

Fig. 6.1. Schematic of indentation of a CNT forest inside a solvent pool.

6.3 Results and discussion

Samples with two different ranges of height were tested in two different mediums: 1) air, and 2) toluene. Each sample was indented on 20 spots to examine the uniformity of the samples. The load-displacement curves for the case of in-air and in-toluene testing of short (25-40 μm) and tall (115-150 μm) CNT forests are demonstrated in Fig. 6.2a, b respectively. The tight distribution of the curves shows the uniformity of the samples. Each load-displacement curve consists of a stiff section up to ~ 3 μm depth followed by a plateau which continues to the point of unloading at 10 μm depth.

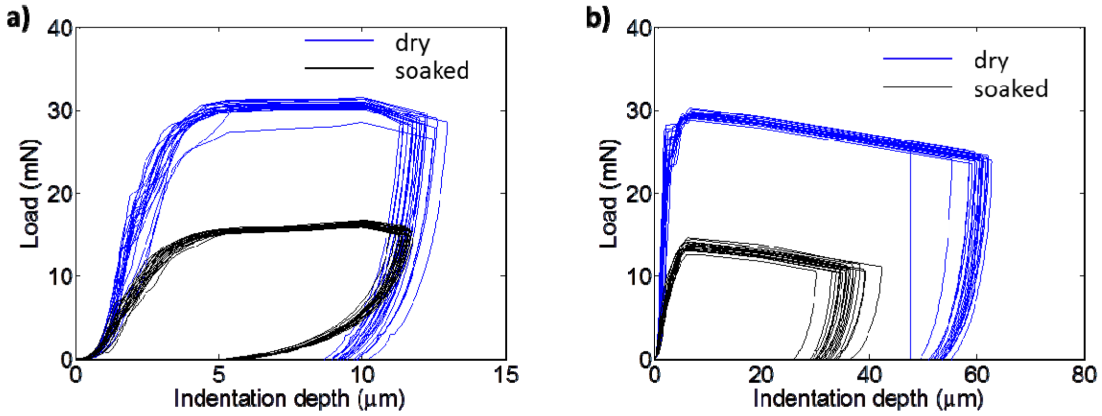

Fig. 6.2. Load-displacement curve for dry and toluene-infiltrated CNT forests with initial average height of a) 30 μm and b) 130 μm.

The deformation mechanism of dry CNT forests grown with LPCVD recipe was reported in chapter 3 using in situ indentation. Local buckles form progressively from the bottom of CNT forests – i.e. close to the substrate – from the very beginning of the indentation at the initial stiff part of the load-displacement curve. The sudden change of slope and start of the plateau region is related to the formation of shear off-sets under the indenter edges and sliding of the indenter into the CNT forest. Visualization of deformation of the wet sample at the time of indentation is not possible due to the limitations of high magnification SEM imaging of wet samples. Since the plateau regions for dry and wet samples are similar, sliding of the indenter into the CNT forests similar to the case of dry sample likely happens in wet samples. However, the buckling behavior of the wet forest is still unknown. To gain insight into the buckling behavior, a different method was used to visualize the deformation of wet CNT forests as much as possible. We performed macroscale compression of dry and wet samples (immersed in toluene) by pressing 1 cm x 1 cm samples using known weights to apply pressures up to 700 kPa which are in the range applied to the samples in the micro-indentation experiments.. All samples were under pressure for more than 6 hours to make sure that wet samples were completely dried under pressure. The deformed CNTs after dry out are expected to have similar morphologies to the deformed wet CNTs. Fig. 6.3a-d show the side and top views of the deformed CNTs after dry and wet compression respectively. The deformation of the dry sample (Fig. 6.3a) is similar to the reported morphology in chapter 3: periodic buckling from the bottom of the CNT forest. The top part remained undeformed and hence the top view image (Fig. 6.3b) is similar to the case of undeformed CNT top image. Deformation under wet compression is observed (Fig. 6.3c,d) to be substantially different from that under dry compression. Local buckles were distributed along the height and CNTs were bent globally – i.e. along the entire height - (Fig. 6.3c) similar to the first buckling mode in Euler buckling of isolated columns. The tips as a result look substantially flattened (Fig. 6.3d). This likely increases the area of CNT to surface contact

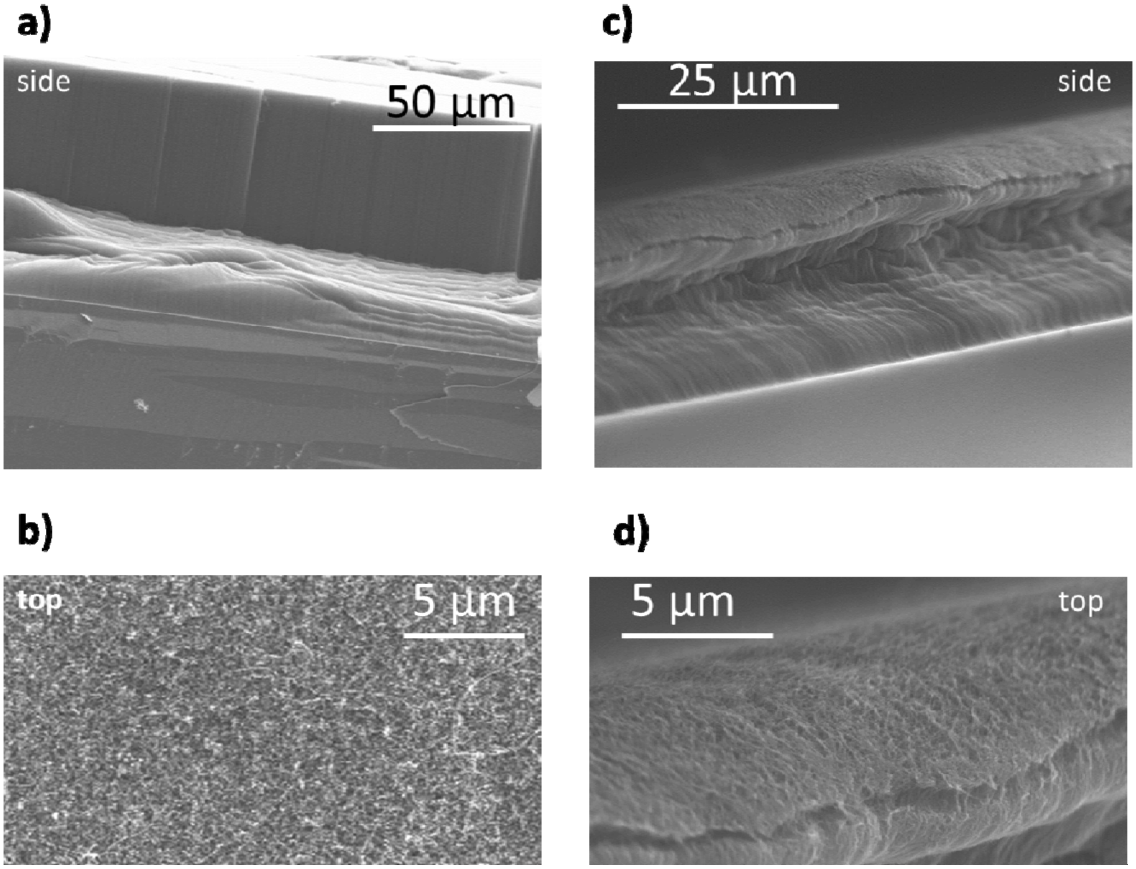

Fig. 6.3. Deformation mechanism of dry and wet CNT forests. a) dry sample – side view, b) dry sample – top view, c) wet compressed and then dried – side view, and d) wet compressed and then dried – top view.

The major differences between the load-displacement curves for the two cases of dry and wet indentation are the stiffness of the CNT forest and the plateau load which is related to the formation of shear off-sets. The load at plateau decreased from 30 mN to 13-15 mN by wetting for both short and long CNT forests. The slope in both initial and unloading sections of the load-displacement curve is smaller for the case of wet samples. Stiffness was measured by the common method [75] of calculating the slope of a fitted power law curve to the unloading curve (last stage of the load-displacement curve) at the beginning of unloading. Wetting the CNT forest with toluene decreased the stiffness from 62.1 ± 13.8 and 36.2 ± 4.0 to 12.1 ± 0.8 and 7.4 ± 0.5 kN/m in the short and long CNT forests respectively. Harmonic (dynamic) stiffness measurement was also performed with 10 nm unloading steps along the indentation path. This method provides information on how stiffness changes with indentation depth. The plots showing the trends of stiffness change with indentation depth are shown in Fig. 6.4. Stiffness increases by increasing depth until the point of shear off-set formation where there is a drop in the stiffness. In both dry and wet states, the maximum harmonic stiffness for the short CNT forest is higher than that for the long CNT forest which is consistent with the observations in chapter 3. The results also show that harmonic stiffness decreases by soaking samples in solvents for both sample heights.

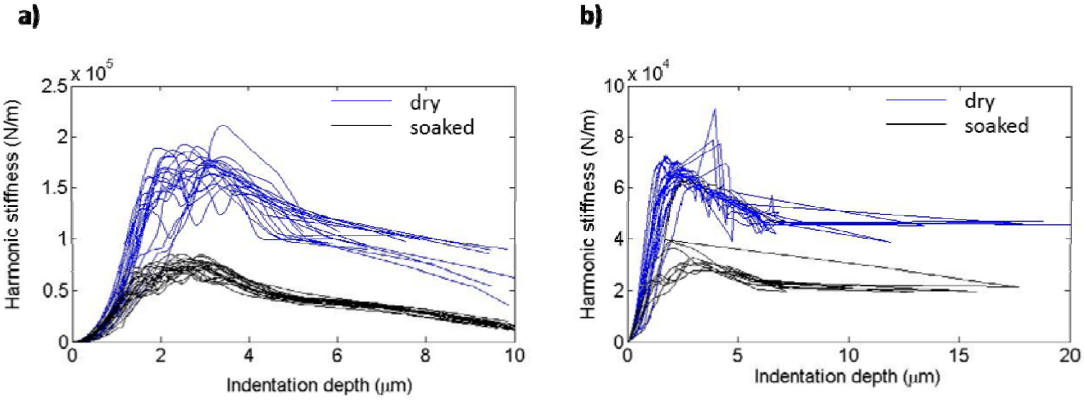

Fig. 6.4. Harmonic stiffness for dry and toluene-infiltrated CNT forests with initial average height of a) 30 μm and b) 130 μm.

Two other solvents - namely acetonitrile and IPA - were used to wet CNT forests and nanoindentation testing was performed on them at a minimum of 10 points. Similar to toluene, these two solvents decreased the stiffness of the CNT forests. The extent of stiffness reduction by solvent infiltration depended on the original stiffness of the CNT forest (i.e. stiffness before hydration). Nine samples with different stiffness were mechanically tested before and after being wetted by the three solvents (three samples with each solvent). The reduction in the maximum harmonic stiffness (the stiffness before formation of shear offsets) versus the original maximum harmonic stiffness is shown in Fig. 6.5. There is an overall increase in the stiffness reduction with the increase in the initial stiffness of the CNT forests. The relationship appears to be approximately linear for every solvent. The slope is in the range of 0.4-0.5. The difference between the trends for the acetonitrile and IPA is not statistically significant. Toluene causes slightly higher reduction in the stiffness compared to the other two solvents.

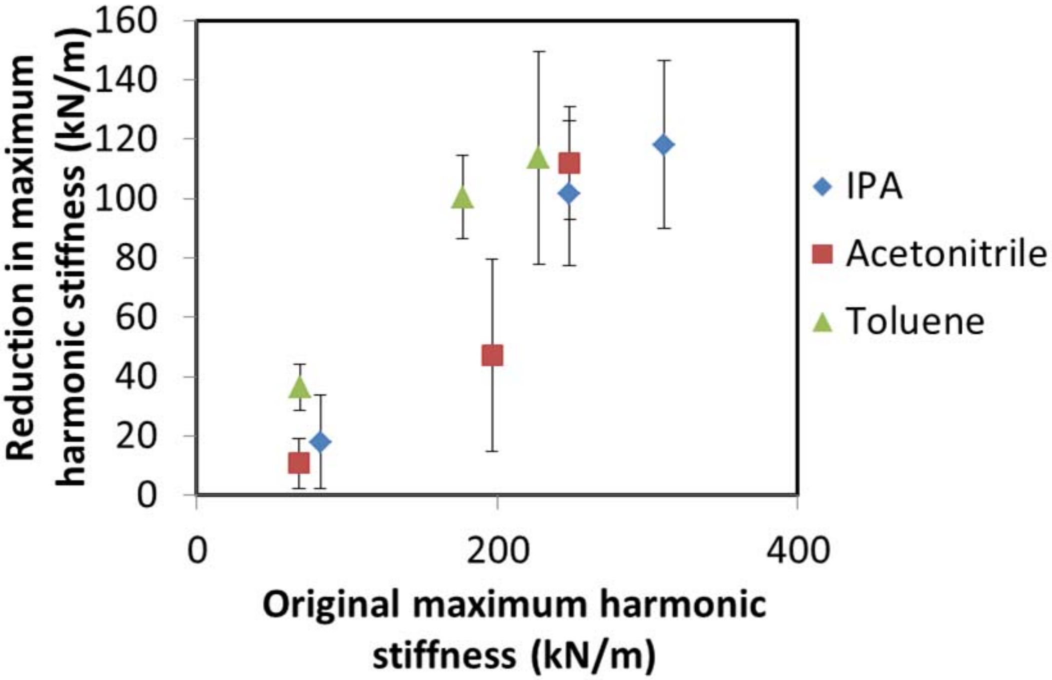

Fig. 6.5. Change of reduction in the maximum harmonic stiffness with the original maximum harmonic stiffness for samples wetted with the three solvents.

The interaction between CNTs was suggested to affect the mechanical response of CNT forests in chapter 3. Here, it is proposed that the effects of solvent on the stiffness and deformation mechanism of the CNT forests are related to the change of the degree of interaction between CNTs. The effective stiffness of CNT forests can be expressed as the combination of two elements. The first element is the stiffness of individual CNTs such as axial compression stiffness and bending stiffness. The second component originates from the interactions between CNTs - mostly at contact points - which provide mechanical support and constraint opposing deformation. Interaction between CNTs is via vdW forces which are due to induced dipole interactions through the act of an electric field from a dipole on the neighbor dipole [102]. Medium that fills the space between the two objects involved in vdW interaction diminishes this dipole-dipole interaction and reduces the vdW force between them [102]. The values of the vdW forces are proportional to Hamaker constant which depends on the macroscopic properties of the interacting objects and the medium such as dielectric constant and refractive index [111]. Effective value of the Hamaker constant A_{121} for evaluating the vdW forces between similar bodies (1) in a medium (2) can be estimated [102] using the values of Hamaker constant for the medium A_{22} and for the objects in vacuum A_{11}.

$$A_{121} = (A_{11}^{1/2} - A_{22}^{1/2})^2 \qquad \text{eq. 1}$$

With the assumption of the Hamaker constant for CNTs being close to graphite, since Hamaker constant for graphite is known [51], the ratio of the Hamaker constant for the case of CNTs in air medium to solvent medium was roughly calculated by using the Hamaker constant for graphite in air. The values for the three solvents, graphite in air, and graphite in the three solvents (calculated using eq. 6.1) are listed in Table 6.1.

Solvents as the medium reduced the Hamaker constant to ~ 40-50% of the original value. While acetonitrile and IPA produced similar values of Hamaker constant, toluene produced slightly lower Hamaker constant compared to the other two solvents. This is probably the reason for the similar effects of acetonitrile and IPA on the stiffness in Fig. 6.5 and slightly higher effects in the case of toluene. We postulate that the slope of the line in Fig. 6.5 is approximately equal to the ratio of the reduction in Hamaker constant with solvent medium divided by the original Hamaker constant, averaged over all significant CNT interaction sites in the forest. Calculation of this average value is beyond the scope of this work because an accurate assessment of the number of CNT interaction sites in a forest is complex and difficult to achieve. However, the slope in Fig. 6.5 (40-50%) being relatively close to the range of Hamaker constant reduction for graphite - 50-60% - provides an evidence for the possibility of this relationship.

Table 6.1. Hamaker constant for solvents and graphite-graphite interactions in solvents. The values for graphite-graphite interactions in solvents are calculated using eq. 6.1.

Interface	**Hamaker constant (e-19 J)**
toluene	0.54 [102]
acetonitrile	0.42 [112]
graphite-air-graphite	4.7 [51]
graphite-toluene-graphite	**2.0**
graphite-acetonitrile-graphite	**2.3**
graphite-IPA-graphite	**2.4**

Both short and long CNT samples were also tested at the dry state after acetonitrile evaporation. Soaking and drying was repeated twice after that and the samples were indented on multiple points in each step. The harmonic stiffness for both samples in all steps are shown in Figure .6. The samples in the dryout condition appear to have greater stiffness values than the original ones. This greater stiffness is due to the densification of CNT forests due to capillary forces. The samples at these steps also have a large variation in the stiffness. This is due to the nonuniformity of surface after densification (a portion of the indenter area comes into contact with CNT surface and this portion varies from point to point). The second and third soaking cause more reduction in the stiffness than the first soaking. This is likely due to reconfiguration of the CNT morphology and contacts during evaporation due to capillary forces.

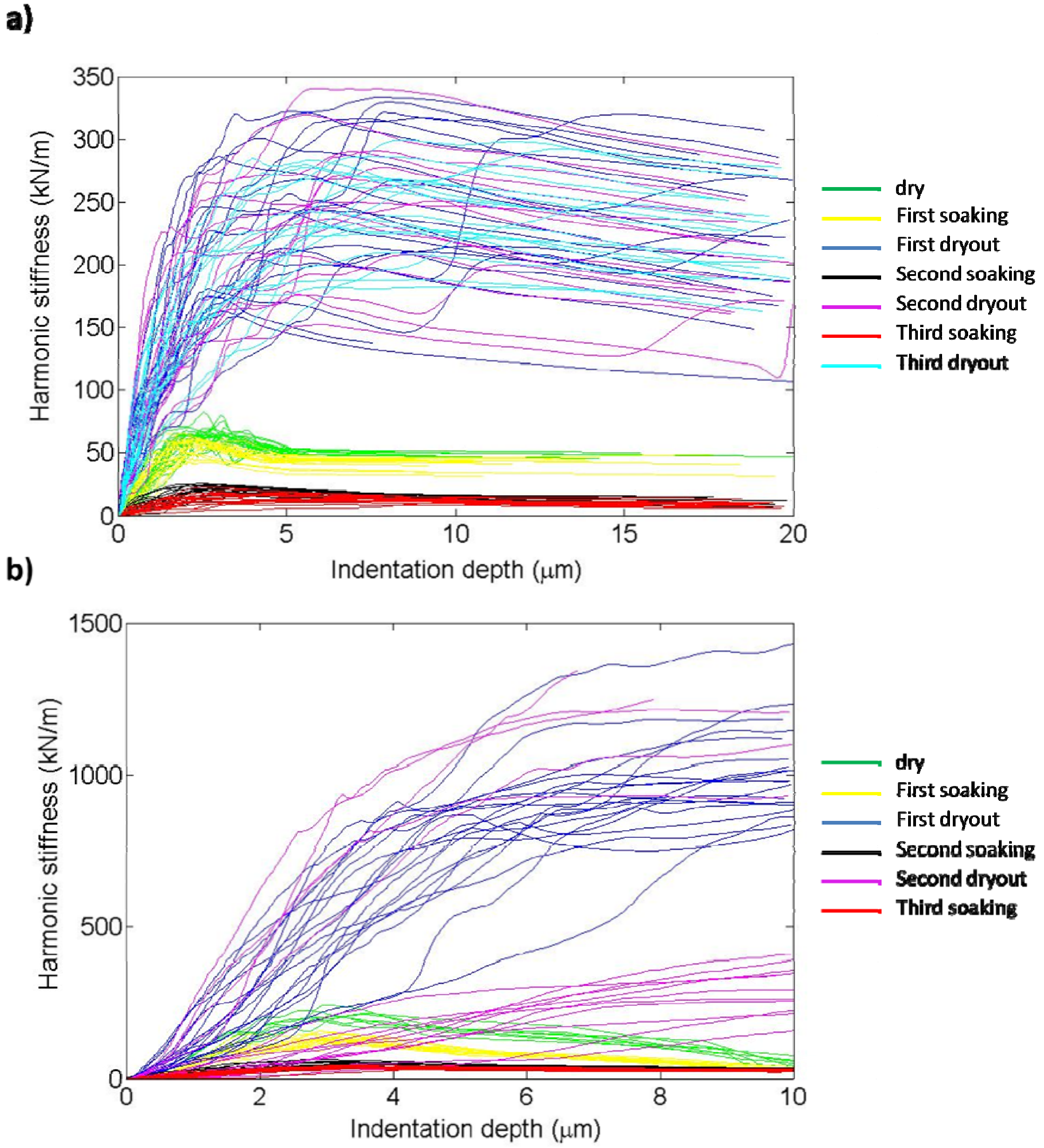

Figure 6.6. Harmonic stiffness of the CNT forests soaked and dried multiple times with acetonitrile. a) a long CNT forest and b) a short CNT forest.

In addition to reducing vdW forces between CNTs, fluids could also act as lubricants that decrease the friction between CNTs as they slide against each other. VdW forces could also play a role in this scenario as normal forces that change the friction forces. To investigate the significance of the lubrication effect (or any significant load-carrying role of solvents) we performed strain rate testing of CNT forests with and without a solvent – toluene was chosen. The results are shown in Fig. 6.7 Since stress and strain rate are proportional in fluids in general[113, 114], changing the strain rate is expected to produce a significant change in the stiffness of the CNT forests in solvents if the solvent is carrying a major part of the stress (e.g. as the lubricant). Stiffness increases by 30 % in the case of dry CNT forest between the strain rates of 0.1 and 1 s^{-1}. This could be related to the viscoelastic nature of CNT forests which has been reported in previous reports[19, 35, 115]. However, no such significant change of stiffness was observed in the wet CNT forest by changing the strain rate by two orders of magnitude. This does not rule out the possibility of the effect of solvents on the stiffness as a lubricant but shows that it is not significant. Therefore, the effect of the vdW is suggested here to be the most significant cause of the decrease in the stiffness of the CNT forest.

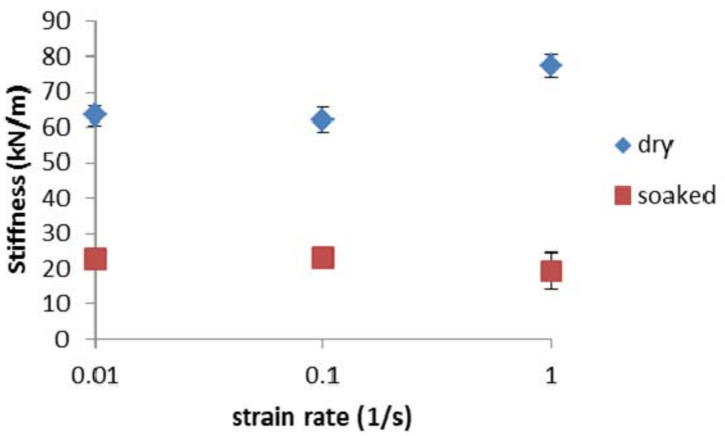

Fig. 6.7. Effect of strain rate on the stiffness of a dry and a wet CNT forest.

The results on the change of stiffness agree qualitatively with the previously reported effects of fluids on the mechanical properties of bucky papers or porous CNT mats. Whitten et al. [116] studied the effects of fluids on the elastic modulus of bucky papers using tensile testing of strips of bucky paper. The testing was performed on dry samples as well as samples in wet condition of water and the ionic liquid 1-butyl-3-methyl-imidazolium tetrafluoroborate. They measured lower modulus in presence of fluids. As the interaction between CNTs in bucky papers have been reported to be dominant by vdW forces [117], the effect of the solvent on the elastic modulus of the bucky papers could be a further support of our conclusions in this work on the effect of vdW forces on the stiffness of CNT forests.

The change in the deformation mechanism can be explained by the effect of solvent on property gradients along the height of CNT forests. It has been previously suggested that gradients of properties such as density and tortuosity affect the location of formation of local buckles along height of CNT forests (chapter 3 and ref. [17, 19]). The gradients are due to both change in the first component of the effective stiffness (stiffness of individual CNTs) and change in the second component (as the result of interaction between CNTs). The latter is less significant in a CNT forest immersed in solvent due to smaller vdW forces between CNTs. This is likely the reason for observation of global (Euler) buckling of CNTs in the case of CNT forests in solvent. Euler buckling was previously observed for CNT forests with less amount of tortuosity and interaction [21].

6.4 Summary

Mechanical behavior of carbon nanotube forests soaked in three solvents were examined. Effective stiffness of CNT forests with two different heights was evaluated in the dry and wet condition by micro-indentation using a 100 μm diameter flat punch. We found that stiffness decreases by using solvent as medium. In addition, deformation mechanism changes from local buckling concentrated close to the bottom of the CNT forest to local buckles distributed along the height and also global buckling of the entire length of CNTs. It was hypothesized that the change in vdW forces at neighboring CNTs by wetting is the major reason for the change in stiffness and deformation mechanism in CNT forest. Other factors such as lubrication effect of the solvent were shown not be as significant by strain rate dependency test. The repeatability of the soaking was examined. It was shown that the stiffness decreases more in the second and third soaking. The results suggest that soaking CNT forests in solvents could be useful for applications such as interface materials where lower stiffness of CNT forests and higher contact area with adjacent surfaces are needed.

CHAPTER 7 SUMMARY AND RECOMMENDATIONS

7.1 Summary

The deformation and failure mechanism of uncoated, top-coated, conformally-coated, and solvent-soaked CNT forests were studied. The results revealed how growth-induced morphology gradients along height of CNT forests, coating of top surface, conformal-coating of the CNTs, and solvents as medium cause or change bending, buckling, delamination, and fracture in CNT forests under compressive loading.

Micro-indentation on the edge of CNT forests revealed the dependence of the location of local buckling along height of CNT forests on the aerial density and tortuosity of CNTs. Deformation started form bottom, middle, and top of the CNT forests grown with LPCVD, APCVD, and PLPCVD respectively. It was shown that regions along the height of the CNT forests with lower density or lower tortuosity are more prone to bending and buckling. While no delamination occurred in micro-indentation of uncoated CNT forests, macro-compression testing of CNT forests with 1 cm^2 area and micro-indentation of CNT forests coated on the top surface with Al using e-beam physical vapor deposition resulted in delamination at the CNT-substrate interface. Tensile stresses on the CNTs close to substrate due to post-buckling deformations caused the delamination and can be estimated using beam bending theory for the population of buckled CNTs under indenter. Nonuniformity of buckling due to height variations in the macroscale CNT forests was demonstrated to play a role in the delamination occurrence. In the coated CNT forests, the thickness of the top Al coating was critical in delamination occurrence as thin coating did not provide the mechanical constraints that cause stresses to reach the strength of the interface. The results are important for design of new CNT forests for different needs by changing growth methods. Knowledge of delamination occurrence could also be used to design CNT based strain or impact sensors.

Micro-indentation of CNT forests coated from top to bottom with alumina by ALD revealed a significant increase that was explained by the effect of the added material in increasing compression and bending stiffness of CNTs. Visualization of deformation mechanism of conformally-coated CNT forests in flat punch mciro-indentaiton showed that fracture happens in CNTs with coatings as thick as 5 nm and that fracture started at the stress of ~ 40 MPa and eventually resulted in full fracture of the CNT/alumina hybrid nanotubes. We proposed that fracture in CNTs was caused by local tensile loading of CNTs after fracture of the coating. Higher recoverability was measured in mciro-indentation testing by a Berkovich tip. This was before significant fracturing of nanotubes and originated form lower vdW forces between alumina nanotubes than CNTs. The gained knowledge could be a framework for design of new hybrid nanostructures based on CNTs for using functionalities of both coating and CNTs.

Soaking CNT forests in three solvents (toluene, acetonitrile, and IPA) resulted in lower stiffness values measured by flat punch indentation. Calculations showed that Hamaker constant (that is proportional to vdW forces between CNTs) is lower in the case of solvents as medium. This demonstrated the effect of vdW forces in the effective stiffness of the CNT forests. The deformation mechanism of CNT forests changed from local buckling close to the substrate and an undeformed top region to global buckling of CNTs that involved the top region of the forest in the bending as well. This was, again, due to the lower vdW forces that made the gradient of morphology along height less significant. The results suggest an easy method of decreasing stiffness and change of deformation mechanism that causes higher contact area at the top surface.

The main unique findings of this work could be listed as following:

- The location of buckling along height of CNT forests could change (from bottom to middle to top) with changing growth parameters.
- Two major factors that determine the location of incipient buckling within CNT forests are the aerial density and tortuosity of CNTs.
- Delamination could happen in macroscale compression of uncoated and microscale indentation of coated CNT forests.
- Tensile stresses due to buckling could exceed the interfacial strength and cause delamination at the growth substrate. Therefore, they are the possible causes of the observed delamination.
- ALD coating of CNT forests does not change the deformation mechanism significantly when the coating is thin (2 nm) but fracture of alumina coating and CNTs happens in the case of thick (5 nm) coating.
- Both stiffness and recoverability increase in nanoindentation of conformally-coated CNT forests using a Berkovich tip.
- Solvent infiltration of CNT forests decreases their stiffness and solvents causing lower vdW forces between CNTs produce lower stiffness values. This shows the importance of vdW forces in the stiffness of CNT forests.

Finally, the main scientific contribution of this work is to show the significance of the effect of morphology of CNT forests in their deformation and failure mechanisms:

tortuosity, aerial density, and interaction between individual CNTs in buckling, uniformity of height and top coating in delamination, and conformal coating in fracture.

7.2 Recommendations

This study could be extended in experimental or theory/computational directions to further advance the fundamental knowledge of structure-property relations in uncoated and coated CNT forests. Systematic investigation of CNT growth parameters such as pressure, temperature, and pre- and post-treatments will be required to find direct relations between growth parameters and morphology along height of CNT forests. Then, relations between deformation and failure mechanism of CNT forests and the growth parameters could be found. In the theory/computational direction, a mesoscale model of CNT forests that captures the tortuosity and entanglement of CNTs and their variations along the height of CNT forests should be developed to quantify the effects of morphology parameters such as tortuosity and density on the buckling, bending, delamination, etc. Adding coatings to the CNTs and studying their effect on the mechanical behavior are expected to shed light on the exact mechanism leading to delamination and fracture in the case of coated CNTs. Furthermore, a medium could be added to quantify the relation between the properties of the medium and the stiffness or deformation mechanism of the CNT forest. This will also provide a better understanding of the effect of vdW forces on the effective stiffness and deformation within the CNT forests.

In a more practical point of view, future studies could be directed toward using the knowledge from this dissertation in tuning the CNT properties for different applications. As an example, as reviewed in chapter 1, the performance of CNT forests as thermal/electrical interface materials highly depends on the contact area between the top surface and opposing surfaces. We recommend using CNT forests that have bending/buckling at the top as interface materials as those are expected to have larger contact areas and better performance. For example, plasma-pretreatment was showed to change the mechanical behavior from buckling close to the substrate to bending of tips. This could result in a better performance as a thermal/electrical interface material. Solvents also distribute the deformation along the height and create larger contact areas and are suggested as a way of improving CNT forests as interface materials. Both of these are also expected to limit the occurrence of delamination at the CNT-substrate interface since buckling close to substrate was the source of delamination. Conformal-coating with high conductivity ALD materials (such as TiO_2 for the case of thermal conductivity) with high stiffness could also be useful for interface materials in applications involving high stresses. The coating prevents CNTs from severe permanent deformations at high stresses. The load limit for such structure will be the load at which nanotubes fracture.

References

1. Guz, A.N. and Y.Y. Rushchitskii, *Nanomaterials: On the mechanics of nanomaterials.* International Applied Mechanics, 2003. **39**(11): p. 1271-1293.

2. Nalwa, H.S., *Encyclopedia of Nanoscience and Nanotechnology*. 2004: American Scientific Publishers.

3. de Heer, W.A., A. Châtelain, and D. Ugarte, *A Carbon Nanotube Field-Emission Electron Source.* Science, 1995. **270**(5239): p. 1179-1180.

4. Xu, J. and T.S. Fisher, *Enhancement of thermal interface materials with carbon nanotube arrays.* International Journal of Heat and Mass Transfer, 2006. **49**(9-10): p. 1658-1666.

5. Amama, P.B., et al., *Dendrimer-assisted controlled growth of carbon nanotubes for enhanced thermal interface conductance.* Nanotechnology, 2007. **18**: p. 385303.

6. Park, M., et al., *Effects of a carbon nanotube layer on electrical contact resistance between copper substrates.* Nanotechnology, 2006. **17**: p. 2294.

7. Yang, Z.P., et al., *Experimental observation of an extremely dark material made by a low-density nanotube array.* Nano Letters, 2008. **8**(2): p. 446-451.

8. Wang, X., et al., *Highly specular carbon nanotube absorbers.* Applied Physics Letters, 2010. **97**(16): p. 163116.

9. Xu, T., et al., *Aligned carbon nanotubes for through-wafer interconnects.* Applied Physics Letters, 2007. **91**(4): p. 042108.

10. Kim, B., H. Chung, and W. Kim, *Supergrowth of Aligned Carbon Nanotubes Directly on Carbon Papers and Their Properties as Supercapacitors.* The Journal of Physical Chemistry C, 2010.

11. McCarter, C.M., et al., *Mechanical compliance of photolithographically defined vertically aligned carbon nanotube turf.* Journal of Materials Science, 2006. **41**(23): p. 7872-7878.

12. Qiu, A., et al., *Local and non-local behavior and coordinated buckling of CNT turfs.* Carbon, 2011. **49**(4): p. 1430-1438.

13. Malik, H., et al., *Quantitative characterization of carbon nanotube turf topology by SEM analysis.* Journal of Materials Science, 2011. **46**(9): p. 3119-3126.

14. Raney, J.R., A. Misra, and C. Daraio, *Tailoring the microstructure and mechanical properties of arrays of aligned multiwall carbon nanotubes by utilizing different hydrogen concentrations during synthesis.* Carbon, 2011. **49**: p. 3631-3638.

15. Mesarovic, S.D., et al., *Mechanical behavior of a carbon nanotube turf.* Scripta Materialia, 2007. **56**(2): p. 157-160.

16. Qi, H.J., et al., *Determination of mechanical properties of carbon nanotubes and vertically aligned carbon nanotube forests using nanoindentation.* Journal of the Mechanics and Physics of Solids, 2003. **51**(11-12): p. 2213-2237.

17. Cao, A.Y., et al., *Super-compressible foamlike carbon nanotube films.* Science, 2005. **310**(5752): p. 1307-1310.

18. Cao, C., et al., *Buckling initiation and displacement dependence in compression of vertically aligned carbon nanotube arrays.* Carbon, 2011. **49**: p. 3190-3199.

19. Hutchens, S.B., L.J. Hall, and J.R. Greer, *In situ Mechanical Testing Reveals Periodic Buckle Nucleation and Propagation in Carbon Nanotube Bundles.* Advanced Functional Materials, 2010. **20**(14): p. 2338-2346.

20. Maschmann, M.R., et al., *Visualizing Strain Evolution and Coordinated Buckling within CNT Arrays by In Situ Digital Image Correlation.* Advanced Functional Materials, 2012. **22**(22): p. 4625.

21. Maschmann, M.R., et al., *In situ SEM Observation of Column-like and Foam-like CNT Array Nanoindentation.* ACS Appl Mater Interfaces, 2011. **3**: p. 648-653.

22. Maschmann, M.R., et al., *Length dependent foam-like mechanical response of axially indented vertically oriented carbon nanotube arrays.* Carbon, 2011. **49**(2): p. 386-397.

23. Barber, A.H., et al., *On the tensile strength distribution of multiwalled carbon nanotubes.* Applied Physics Letters, 2005. **87**(20): p. 203106-203106-3.

24. Hamdan, A., et al., *Evaluation of a thermal interface material fabricated using thermocompression bonding of carbon nanotube turf.* Nanotechnology, 2010. **21**: p. 015702.

25. Pour Shahid Saeed Abadi, P., C.K. Leong, and D.D.L. Chung, *Factors That Govern the Performance of Thermal Interface Materials.* Journal of Electronic Materials, 2009. **38**(1): p. 175-192.

26. Pathak, S., et al., *Higher Recovery and Better Energy Dissipation at Faster Strain Rates in Carbon Nanotube Bundles: an in-situ Study.* ACS Nano, 2011: p. submitted.

27. Cola, B.A., J. Xu, and T.S. Fisher, *Contact mechanics and thermal conductance of carbon nanotube array interfaces.* International Journal of Heat and Mass Transfer, 2009. **52**(15-16): p. 3490-3503.

28. Xie, S., et al., *Mechanical and physical properties on carbon nanotube.* Journal of Physics and Chemistry of Solids, 2000. **61**(7): p. 1153-1158.

29. Gomathi, A., et al., *Chemically bonded ceramic oxide coatings on carbon nanotubes and inorganic nanowires.* Advanced Materials, 2005. **17**(22): p. 2757-2761.

30. Zbib, A.A., et al., *The coordinated buckling of carbon nanotube turfs under uniform compression.* Nanotechnology, 2008. **19**(17): p. 175704.

31. Waters, J.F., et al., *Buckling instabilities in multiwalled carbon nanotubes under uniaxial compression.* Applied Physics Letters, 2004. **85**(10): p. 1787-1789.

32. Waters, J.F., P.R. Guduru, and J.M. Xu, *Nanotube mechanics - Recent progress in shell buckling mechanics and quantum electromechanical coupling.* Composites Science and Technology, 2006. **66**(9): p. 1141-1150.

33. Tong, T., et al., *Height independent compressive modulus of vertically aligned carbon nanotube arrays.* Nano Letters, 2008. **8**(2): p. 511-515.

34. Misra, A., J.R. Greer, and C. Daraio, *Strain Rate Effects in the Mechanical Response of Polymer-Anchored Carbon Nanotube Foams.* Advanced Materials, 2009. **21**(3): p. 334-338.

35. Pathak, S., et al., *Viscoelasticity and high buckling stress of dense carbon nanotube brushes.* Carbon, 2009. **47**(8): p. 1969-1976.

36. Suhr, J., et al., *Fatigue resistance of aligned carbon nanotube arrays under cyclic compression.* Nature Nanotechnology, 2007. **2**(7): p. 417-421.

37. Ang, L., et al., *Decoration of activated carbon nanotubes with copper and nickel.* Carbon, 2000. **38**(3): p. 363-372.

38. Kong, F., et al., *Continuous Ni-layer on multiwall carbon nanotubes by an electroless plating method.* Surface and Coatings Technology, 2002. **155**(1): p. 33-36.

39. Lee, J., et al., *Al_2O_3 nanotubes and nanorods fabricated by coating and filling of carbon nanotubes with atomic-layer deposition.* Journal of crystal growth, 2003. **254**(3): p. 443-448.

40. Liu, Z.J., et al., *A simple method for coating carbon nanotubes with Co-B amorphous alloy.* Materials Letters, 2003. **57**(7): p. 1339-1344.

41. McBride, J., E. Yunus, and S. Spearing, *Improving the contact resistance at low force using gold coated carbon nanotube surfaces.* The European Physical Journal Applied Physics, 2010. **50**(01).

42. Morisada, Y. and Y. Miyamoto, *SiC-coated carbon nanotubes and their application as reinforcements for cemented carbides.* Materials Science and Engineering: A, 2004. **381**(1): p. 57-61.

43. Tripathi, S.M., T.S. Bholanath, and S. Shantkriti, *Synthesis and Study of Applications of Metal coated Carbon Nanotubes.*

44. Wei, X.W., et al., *Coating multi-walled carbon nanotubes with metal sulfides.* Materials chemistry and physics, 2005. **92**(1): p. 159-163.

45. Zhang, Y., et al., *Metal coating on suspended carbon nanotubes and its implication to metal-tube interaction.* Chemical Physics Letters, 2000. **331**(1): p. 35-41.

46. Zhang, Y., et al., *Coating of carbon nanotubes with tungsten by physical vapor deposition.* Solid state communications, 2000. **115**(1): p. 51-55.

47. Chandrashekar, A., et al., *Forming carbon nanotube composites by directly coating forests with inorganic materials using low pressure chemical vapor deposition.* Thin solid films, 2008. **517**(2): p. 525-530.

48. Min, Y.S., et al., *Ruthenium oxide nanotube arrays fabricated by atomic layer deposition using a carbon nanotube template.* Advanced Materials, 2003. **15**(12): p. 1019-1022.

49. Herrmann, C., et al., *Multilayer and functional coatings on carbon nanotubes using atomic layer deposition.* Applied Physics Letters, 2005. **87**: p. 123110.

50. Willinger, M.G., et al., *The controlled deposition of metal oxides onto carbon nanotubes by atomic layer deposition: examples and a case study on the application of V2O4 coated nanotubes in gas sensing.* Phys. Chem. Chem. Phys., 2009. **11**(19): p. 3615-3622.

51. Lyklema, J., *Fundamentals of interface and colloid science*. 2000, San Diego: Academic Press. v. <3 >.

52. John H. Taphouse, T.L.B., Virendra Singh, Parisa Pour Shahid Saeed Abadi, Samuel Graham, Baratunde A. Cola, *Carbon Nanotube Thermal Interfaces Enhanced with Sprayed on Nanoscale Polymer Coatings.* 2013.

53. Pour Shahid Saeed Abadi, P. and D.D.L. Chung, *Numerical Modeling of the Performance of Thermal Interface Materials in the Form of Paste-Coated Sheets.* Journal of Electronic Materials, 2011. **40**(7): p. 1490-1500.

54. Cola, B.A., et al., *Photoacoustic characterization of carbon nanotube array thermal interfaces.* Journal of Applied Physics, 2007. **101**: p. 054313.

55. Cola, B.A., X. Xu, and T.S. Fisher, *Increased real contact in thermal interfaces: A carbon nanotube/foil material.* Applied Physics Letters, 2007. **90**: p. 093513.

56. Cola, B.A., et al., *Carbon nanotube array thermal interfaces for high-temperature silicon carbide devices.* Nanoscale and Microscale Thermophysical Engineering, 2008. **12**(3): p. 228-237.

57. Lin, W., et al., *Parametric study of intrinsic thermal transport in vertically aligned multi-walled carbon nanotubes using a laser flash technique.* Carbon, 2012. **50**(4): p. 1591-1603.

58. Iijima, S., *Helical Microtubules of Graphitic Carbon.* Nature, 1991. **354**(6348): p. 56-58.

59. Magrez, A., et al., *Catalytic CVD Synthesis of Carbon Nanotubes: Towards High Yield and Low Temperature Growth.* Materials, 2010. **3**(11): p. 4871-4891.

60. Dai, H.J., *Carbon nanotubes: Synthesis, integration, and properties.* Accounts of Chemical Research, 2002. **35**(12): p. 1035-1044.

61. Sinnott, S.B., et al., *Model of carbon nanotube growth through chemical vapor deposition.* Chemical Physics Letters, 1999. **315**(1–2): p. 25-30.

62. Baker, R.T.K., et al., *Formation of filamentous carbon from iron, cobalt and chromium catalyzed decomposition of acetylene.* Journal of Catalysis, 1973. **30**(1): p. 86-95.

63. Meyyappan, M., et al., *Carbon nanotube growth by PECVD: a review.* Plasma Sources Science & Technology, 2003. **12**(2): p. 205-216.

64. Xu, J. and T.S. Fisher, *Enhanced thermal contact conductance using carbon nanotube array interfaces.* IEEE Transactions on Components and Packaging Technologies, 2006. **29**(2): p. 261-267.

65. Bedewy, M., et al., *Collective Mechanism for the Evolution and Self-Termination of Vertically Aligned Carbon Nanotube Growth.* Journal of Physical Chemistry C, 2009. **113**(48): p. 20576-20582.

66. De Volder, M.F.L., et al., *Self-similar organization of arrays of individual carbon nanotubes and carbon nanotube micropillars.* Microelectronic Engineering, 2010. **87**(5-8): p. 1233-1238.

67. Wu, J., et al., *Distortion of carbon nanotube array and its influence on carbon nanotube growth and termination.* Colloids and Surfaces A: Physicochemical and Engineering Aspects, 2008. **313**: p. 13-17.

68. Zhu, S., et al., *Growth orientation of carbon nanotubes by thermal chemical vapor deposition.* Journal of crystal growth, 2002. **234**(2-3): p. 584-588.

69. Su, H.C., et al., *Improving the adhesion of carbon nanotubes to a substrate using microwave treatment.* Carbon, 2010. **48**(3): p. 805-812.

70. Cao, A., et al., *Multifunctional brushes made from carbon nanotubes.* Nature materials, 2005. **4**(7): p. 540-545.

71. Talapatra, S., et al., *Direct growth of aligned carbon nanotubes on bulk metals.* Nature Nanotechnology, 2006. **1**(2): p. 112-116.

72. Cross, R., et al., *A metallization and bonding approach for high performance carbon nanotube thermal interface materials.* Nanotechnology, 2010. **21**: p. 445705.

73. *Deformation behavior and mechanical analysis of vertically aligned carbon nanotube (VACNT) bundles.*

74. Säynätjoki, A., *Atomic-layer-deposited thin films for silicon nanophotonics.*

75. Oliver, W.C. and G.M. Pharr, *An improved technique for determining hardness and elastic modulus using load and displacement sensing indentation experiments.* Journal of Materials Research, 1992. **7**(06): p. 1564-1583.

76. Pharr, G.M., W.C. Oliver, and F.R. Brotzen, *On the Generality of the Relationship among Contact Stiffness, Contact Area, and Elastic-Modulus during Indentation.* Journal of Materials Research, 1992. **7**(3): p. 613-617.

77. Yu, M.-F., et al., *Strength and Breaking Mechanism of Multiwalled Carbon Nanotubes Under Tensile Load.* Science, 2000. **287**(5453): p. 637-640.

78. Qi, H., et al., *Determination of mechanical properties of carbon nanotubes and vertically aligned carbon nanotube forests using nanoindentation.* Journal of the Mechanics and Physics of Solids, 2003. **51**(11-12): p. 2213-2237.

79. Zbib, A., et al., *The coordinated buckling of carbon nanotube turfs under uniform compression.* Nanotechnology, 2008. **19**: p. 175704.

80. Kim, J.Y., D. Jang, and J.R. Greer, *Insight into the deformation behavior of niobium single crystals under uniaxial compression and tension at the nanoscale.* Scripta Materialia, 2009. **61**(3): p. 300-303.

81. Hutchens, S.B., *Deformation behavior and mechanical analysis of vertically aligned carbon nanotube (VACNT) bundles*, 2011, California Institute of Technology.

82. Hutchens, S.B., A. Needleman, and J.R. Greer, *Analysis of uniaxial compression of vertically aligned carbon nanotubes.* Journal of the Mechanics and Physics of Solids, 2011. **59**: p. 2227-2237

83. Doerner, M. and W. Nix, *A method for interpreting the data from depth-sensing indentation instruments.* Journal of Materials Research, 1986. **1**(04): p. 601-609.

84. Qiu, A., et al., *Time-dependent contact behavior between diamond and a CNT turf.* Nanotechnology, 2011. **22**: p. 295702.

85. Slocum, A.H. and O. Yaglioglu, *Carbon nanotube based electromechanical probes*, 2007, Massachusetts Institute of Technology.

86. Lu, Y., et al., *Large-Displacement Indentation Testing of Vertically Aligned Carbon Nanotube Arrays.* Experimental Mechanics.

87. Pour Shahid Saeed Abadi, P., et al., *Effects of morphology on the micro-compression response of carbon nanotube forests.* Nanoscale, 2012. **4**(11): p. 3373-3380.

88. Hutchinson, J.W., M.D. Thouless, and E.G. Liniger, *Growth and configurational stability of circular, buckling-driven film delaminations.* Acta Metallurgica et Materialia, 1992. **40**(2): p. 295-308.

89. Thouless, M.D., J.W. Hutchinson, and E.G. Liniger, *Plane-strain, buckling-driven delamination of thin films: Model experiments and mode-II fracture.* Acta Metallurgica et Materialia, 1992. **40**(10): p. 2639-2649.

90. Wang, X.J., et al., *Visible and near-infrared radiative properties of vertically aligned multi-walled carbon nanotubes.* Nanotechnology, 2009. **20**(21).

91. Gao, Y., et al., *Impact of nanotube density and alignment on the elastic modulus near the top and base surfaces of aligned multi-walled carbon nanotube films.* Carbon, 2012. **50**(10): p. 3789-3798.

92. Hutchens, S.B., et al., *Nanoshearing.* Materials Today, 2012. **15**(3): p. 127.

93. Pathak, S., et al., *Compressive Response of Vertically Aligned Carbon Nanotube Films Gleaned from In-Situ Flat Punch Indentations.* Journal of Materials Research, 2012. **1**(1).

94. Cola, B.A., et al., *Carbon Nanotube Array Thermal Interfaces for High-Temperature Silicon Carbide Devices.* Nanoscale and Microscale Thermophysical Engineering, 2008. **12**(3): p. 228-237.

95. Lahiri, I., et al., *Ultrathin alumina-coated carbon nanotubes as an anode for high capacity Li-ion batteries.* Journal of Materials Chemistry, 2011. **21**(35): p. 13621-13626.

96. Cha, S.I., et al., *Strengthening and toughening of carbon nanotube reinforced alumina nanocomposite fabricated by molecular level mixing process.* Scripta Materialia, 2005. **53**(7): p. 793-797.

97. Andrews, R., et al., *Continuous production of aligned carbon nanotubes: a step closer to commercial realization.* Chemical Physics Letters, 1999. **303**(5–6): p. 467-474.

98. Wong, E.W., P.E. Sheehan, and C.M. Lieber, *Nanobeam mechanics: Elasticity, strength, and toughness of nanorods and nanotubes.* Science, 1997. **277**(5334): p. 1971-1975.

99. Demczyk, B.G., et al., *Direct mechanical measurement of the tensile strength and elastic modulus of multiwalled carbon nanotubes.* Materials Science and Engineering a-Structural Materials Properties Microstructure and Processing, 2002. **334**(1-2): p. 173-178.

100. Salvetat, J.P., et al., *Mechanical properties of carbon nanotubes.* Applied Physics a-Materials Science & Processing, 1999. **69**(3): p. 255-260.

101. Tripp, M.K., et al., *The mechanical properties of atomic layer deposited alumina for use in micro- and nano-electromechanical systems.* Sensors and Actuators a-Physical, 2006. **130**: p. 419-429.

102. Hiemenz, P.C. and R. Rajagopalan, *Principles of colloid and surface chemistry*. 3rd ed. 1997, New York: Marcel Dekker. xix, 650 p.

103. Lefèvre, G. and A. Jolivet. *Calculation of Hamaker constants applied to the deposition of metallic oxide particles at high temperature*. in *Proceedings of International Conference on Heat Exchanger Fouling and Cleaning*. 2009.

104. Garcia, E.J., et al., *Fabrication of composite microstructures by capillarity-driven wetting of aligned carbon nanotubes with polymers.* Nanotechnology, 2007. **18**(16).

105. Tawfick, S., M. De Volder, and A.J. Hart, *Structurally Programmed Capillary Folding of Carbon Nanotube Assemblies.* Langmuir, 2011. **27**(10): p. 6389-6394.

106. Zhao, Z.Z., et al., *Bending of nanoscale filament assemblies by elastocapillary densification.* Physical Review E, 2010. **82**(4).

107. Liu, Z., et al., *Densification of carbon nanotube bundles for interconnect application.* Proceedings of the IEEE 2007 International Interconnect Technology Conference, 2007: p. 201-203.

108. De Volder, M.F.L., et al., *Fabrication and electrical integration of robust carbon nanotube micropillars by self-directed elastocapillary densification.* Journal of Micromechanics and Microengineering, 2011. **21**(4): p. 045033.

109. Qiu, A. and D.F. Bahr, *The role of density in the mechanical response of CNT turfs.* Carbon, (0).

110. Pushparaj, V., et al., *Deformation and capillary self-repair of carbon nanotube brushes.* Carbon, 2012. **50**(15): p. 5618-5620.

111. Van Oss, C.J., M.K. Chaudhury, and R.J. Good, *Interfacial Lifshitz-van der Waals and polar interactions in macroscopic systems.* Chemical Reviews, 1988. **88**(6): p. 927-941.

112. Takenaga, M., et al., *Effective van der Waals surface energy of self-assembled monolayer films having systematically varying degrees of molecular fluorination.* Journal of Colloid and Interface Science, 2008. **320**(1): p. 264-267.

113. Kay, J.M. and R.M. Nedderman, *Fluid mechanics and transfer processes*. 1985, Cambridge Cambridgeshire ; New York, N.Y.: Cambridge UniversityPress. xviii, 602 p.

114. Chhabra, R.P. and J.F. Richardson, *Non-Newtonian flow in the process industries : fundamentals and engineering applications*. 1999, Oxford ; Boston, MA: Butterworth-Heinemann. xiii, 436 p.

115. Zhang, Q., et al., *Viscoelastic creep of vertically aligned carbon nanotubes.* Journal of Physics D: Applied Physics, 2010. **43**: p. 315401.

116. Whitten, P.G., G.M. Spinks, and G.G. Wallace, *Mechanical properties of carbon nanotube paper in ionic liquid and aqueous electrolytes.* Carbon, 2005. **43**(9): p. 1891-1896.

117. Coleman, J.N., et al., *Improving the mechanical properties of single-walled carbon nanotube sheets by intercalation of polymeric adhesives.* Applied Physics Letters, 2003. **82**(11): p. 1682-1684